UNIVERSITÀ
DEGLI STUDI
DI TRIESTE

UNIVERSITÀ DEGLI STUDI DI TRIESTE

XXXIV CICLO DEL DOTTORATO DI RICERCA IN FISICA

A theoretical investigation of ultrathin space charge layers in hematite photoelectrodes

Settore scientifico-disciplinare: **FIS/03 Fisica della Materia**

DOTTORANDO / A
Paola Andrea
Delcompare Rodríguez

COORDINATORE
PROF. Francesco Longo Francesco Longo

SUPERVISORE DI TESI
PROF. Nicola Seriani

ANNO ACCADEMICO 2020/2021

Abstract

Many efforts have been devoted to understand the hematite-electrolyte interface due to its potential application in the photoelectrocatalytic oxidation of water. This interface usually extends over lengths ranging from tens of nanometers to micrometers under water splitting conditions, therefore its realistic simulation via ab-initio calculations has been considered challenging. However, recent experiments measured space charge layers smaller than ∼10 Å in highly doped nanostructured hematite photoanodes, which also displayed high photocurrent densities in water splitting experiments.

We used a set of continuous equations based on the Poisson-Boltzmann distribution and the Stern model to investigate under which experimental conditions the space charge layer in hematite becomes ultrathin. In this regime, a considerable fraction of the potential drop across the interface is located in the Helmholtz layer, therefore we reported corrections to the Mott-Schottky equation that should be taken into account under these conditions. Using the continuous equations, we also examined the effect of the macroscopic properties provided by experiments on the microscopic state of the interface: we got access to the width of the space charge layer and the distribution of the electrostatic potential across the interface a function of the experimental conditions. We then used density functional theory (DFT) to get an atomistic insight of the space charge layer in the semiconductor, in systems ranging from the pristine stoichiometric surface, a surface with adsorbed hydroxyls, to Ti-doped slabs with doping densities of the order of $\sim 1.0 \times 10^{21} cm^{-3}$. We disregarded the presence of the electrolyte on the DFT calculations, since we focused on the development of the space charge layer in the semiconductor. In our simulations, the hematite slabs are in contact with vacuum.

According to our analysis, space charge layers around 10 Å must have been present also in other water splitting experiments with some of highest photocurrents registered. We observed that at high doping densities the inverse of the square of the capacitance should have a quadratic behavior close to flat-band conditions and a sub-linear behavior due to square-root-like corrections far from the flat-band potential. We used density functional theory to compute the band bending of the proposed atomistic models. The pristine

stoichiometric and the hydroxylated undoped surfaces displayed band bendings of ~ 0.14 eV and ~ 0.49 eV, respectively. In the doped case, we found band bendings of ~ 0.07 eV and ~ 0.01 eV for the pristine and OH-terminated slabs, respectively. The latter band bendings corresponded to space charge layers extending in the sub-nanometer regime, according to the continuous equations. In the presence of doping, we found a qualitative and quantitative correspondence between the results provided by density functional and the continuous model.

Contrary to the common picture of the electrochemical interface of a semiconductor and an electrolyte in water splitting experiments, where large space charge layers are present, the latter results give an insight of an unexpected regime of high photoelectrocatalytic efficiency in ultrathin space charge layers. Which in principle, are amenable to quantum mechanical ab-initio simulations. In this work we were able to describe the space charge layer of thin hematite slabs using DFT at an atomistic level.

Acknowledgements

I would like to thank my supervisor, Nicola Seriani, for his support, fruitful discussions and the knowledge he shared with me during these three years.

I want to express my deep gratitude to the International Centre for Theoretical Physics for the resources and space that were granted to me during my PhD. As well as for the opportunity that it was given to me at the ICTP Postgraduate Diploma Programme.

Finally, I would like to thank my family, specially to my mom Janette and my father Roberto for believing in me and their love. And to all my friends (which are spread across the world) for the good times we spent together and their support.

Table of Contents

List of Figures

List of Tables

Chapter 1

Introduction

Climate change and the increase of the global energy consumption require the search for greener sources of energy. Solar energy has attracted attention among renewable energy sources. This is because the sun represents the largest source of energy on the planet: the energy it produces is enough to cover the energetic needs of humanity. Photovoltaic cells are already used to harvest solar energy, however the energy they produce has to be stored in other devices.[1,2] Therefore more efficient ways to harvest and store solar energy are required. A direct way to store solar power is to save the electromagnetic energy into chemical bonds, leading to the production of fuels. This can be achieved through photoelectrochemical reactions in photoelectrochemical cells (PEC).[1–6] Figure 1.1 shows a scheme of a basic photoelectrochemical cell, which is constituted by a photoactive material acting as anode, a cathode, an electrolyte and an external circuit. In these devices the solar light is absorbed by the photoelectrode and the solar fuels are produced in both anode and cathode.

The photoelectrochemical splitting of water into molecular oxygen and molecular hydrogen is one of the reactions investigated to store solar energy into chemical bonds. This reaction is described as follows[3–6]

$$2\mathrm{H_2O} + 4h\nu \rightarrow 2\mathrm{H_2} + \mathrm{O_2}. \tag{1.1}$$

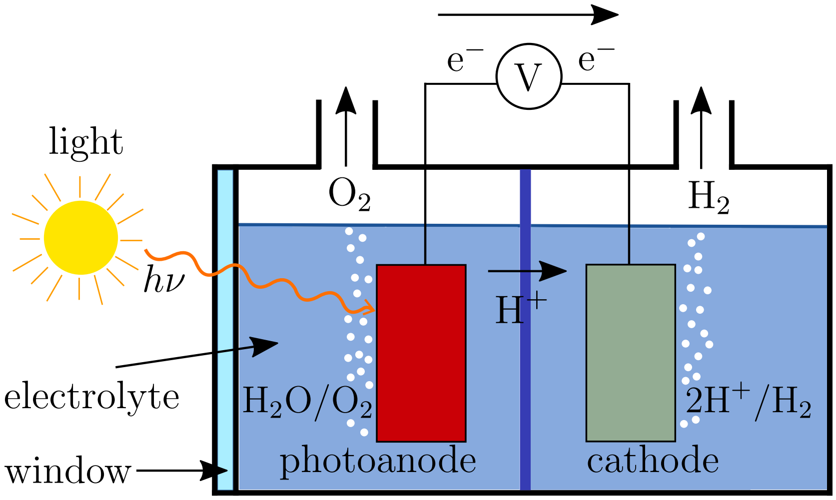

Figure 1.1: Scheme of a photoelectrochemical cell for the water splitting reaction. The photons coming from the sun are absorbed by the photoanode generating electrons and holes. The holes are used in the anode to oxidize H_2O to O_2. The photogenerated electrons are transported to the cathode aided by the external bias and used in the reduction of H^+ to H_2. Each gas can be stored then separately, as shown in the picture.

The two half redox reactions involved in this process are the oxygen evolution reaction (OER) or water oxidation and the hydrogen evolution reaction (HER).[3–6] The first takes place at the photoanode and the second occurs at the cathode, see figure 1.1. At alkaline pH conditions, the OH^- dominate over H^+. Under these conditions, the OER and HER are[4,6]

$$4\mathrm{OH}^-(aq) + 4h^+ \rightarrow 2\mathrm{H_2O} + \mathrm{O_2} \qquad (\mathrm{OER}), \tag{1.2}$$

$$2\mathrm{H_2O} + 2e^- \rightarrow \mathrm{H_2} + 2\mathrm{OH}^-(aq) \qquad (\mathrm{HER}). \tag{1.3}$$

On the other hand, under acidic conditions, due to the higher concentrations of protons H^+, the OER and HER are[4,6]

$$2H_2O + 4h^+ \rightarrow O_2 + 4H^+(aq) \qquad \text{(OER)}, \tag{1.4}$$

$$2H^+ + 2e^- \rightarrow H_2 \qquad \text{(HER)}. \tag{1.5}$$

Thermodynamically, reactants and products are in equilibrium at an applied bias of $V = 1.23$ V.[4,5,7,8] Semiconducting materials are needed as photoanodes in order to absorb the photons required to produce the charge carriers involved in the photoelectrochemical water splitting reaction, see figure 1.1. Once the photons are absorbed by the photoanode, in the case of an n-type semiconductor, the produced holes are transported to the surface and participate in the OER. On the other hand, the photo-excited electrons migrate to the cathode helped by the external circuit. Since the water splitting reaction and the water oxidation occur at the photoanode, much effort has been directed towards the search of the ideal semiconductor capable to perform this task.

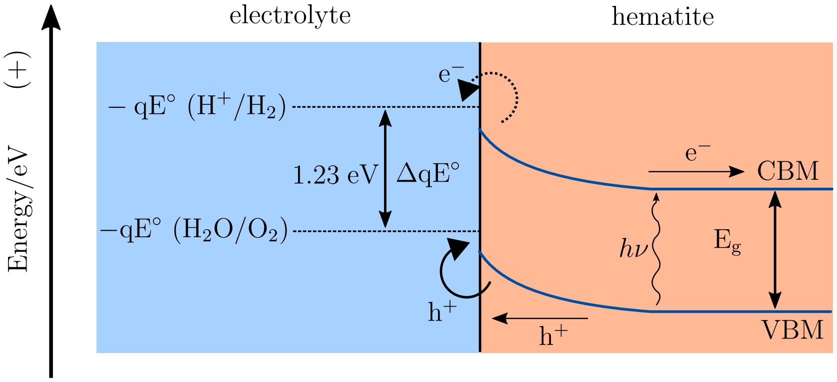

Figure 1.2: Relative position of hematite energy bands and the electrochemical potentials − q E° of the (H^+/H_2) and (O_2/H_2O) redox couples in the electrolyte, E° is the reduction potential. The energy bands in hematite bend in the vicinity of the surface. CBM is the conduction band minimum and VBM is the valence band maximum. The dashed arrow indicate that the electron transfer to the surface of hematite is not spontaneous. E° is the reduction potential for both (H^+/H_2) and (O_2/H_2O) redox couples.

Among semiconductors, oxides have been investigated due to their optical and properties and stability under oxidizing conditions.[4] The electronic structures of these kind of materials generally display valence bands (VB) consisting on O-2p orbitals, and conduction bands formed by valence orbitals of metals.[4] Some of these oxides are TiO_2, WO_3, $BiVO_4$ and Fe_2O_3. TiO_2, for example, has been extensively investigated after Fujishima and Honda performed water splitting by UV light-induced electrocatalysis.[9] However, the optical activity of TiO_2, WO_3 and $BiVO_4$ is limited by the large bandgap of $E_g \sim 3$ eV displayed by these materials.[4,5]

In this work we focus on hematite ($\alpha-Fe_2O_3$), which has been studied during the last decades due to its advantageous properties: large abundance, non-toxicity, electrochemical stability at pH greater than 3, bandgap of $\sim$ 2 eV and a favorable position of the valence band for the oxygen evolution reaction.[1,5,6] Indeed, a suitable photoanode for water oxidation should also have a valence band positioned favorably with respect to the redox potential of the oxygen evolution reaction. Figure 1.2 shows the relative positions of the electrochemical potentials $-qE^\circ$ for the (H^+/H_2) and (O_2/H_2O) redox couples, and the conduction and valence bands of hematite.[4,6,10] There it can be seen that hematite cannot perform the reduction of hydrogen by itself: the conduction band lies below the redox potential of (H^+/H_2). This means that the electrons cannot be spontaneously transferred to perform the hydrogen evolution reaction and therefore an external bias is required to perform the overall water splitting reaction,[6] see Figure 1.1. Hematite presents additional drawbacks: low conductivity in the bulk, high-electron hole recombination and slow kinetics of the oxygen evolution reaction.[1,5,6] Some authors suggest the two latter drawbacks occur due to the sluggish transfer of holes at the hematite/electrolyte interface.[11] Therefore a better understanding of the semiconductor-electrolyte interface would be important to rationalize these problems.

The semiconductor-electrolyte interface consists of a space charge layer in the semiconductor and a charge distribution with opposite sign in the electrolyte.[4,12,13] Figure 1.3 shows a representation of the hematite-electrolyte interface. The space charge layer is constituted by fixed ionized donor atoms. The charge distribution in the electrolyte consists of ions and solvent molecules, which are adsorbed at the semiconductor surface and also distributed in the solvent. This charge configuration at the interface is due to the charge redistribution that occurs when both materials are put into contact. In the case of

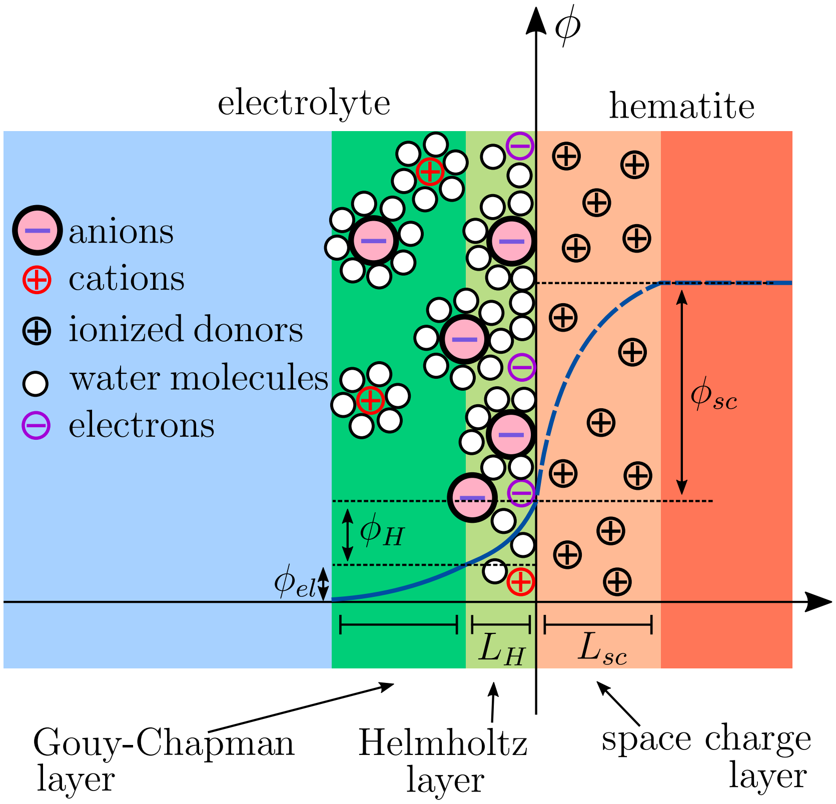

Figure 1.3: Hematite-electrolyte interface. This figure shows the charge distribution in both sides of the interface. According to the Stern model, the interface can be separated in three main regions: the space charge layer, the Helmholtz layer and the Gouy-Chapman layer. A potential distribution develops in the vicinity of the surface of the semiconductor, which is illustrated as a function of the spatial extension of the interface. The potential drops across the space charge layer, the Helmholtz layer and the Gouy-Chapman layer are denoted by ϕ_{sc}, ϕ_H and ϕ_{el}, respectively.

an n-type semiconductor like hematite, electrons migrate from the solid to the electrolyte until the Fermi level or electrochemical potential is equal in both sides.[4,12,13] The charge distributions in the solid and the liquid imply the existence of a potential drop across the interface, as depicted in the y-axis in figure 1.3. The potential drop in the space charge layer changes ϕ_{sc} the potential energy of the electrons in hematite leading to the upward bending of the energy bands bend in the vicinity of the surface, as depicted on the right side of Figure 1.2. This bending is measured as the potential drop in the space charge layer ϕ_{sc} and is commonly known as the band bending BB, see Figure 1.3. It is fundamental for the water splitting reaction, because it allows the transport of photogenerated holes in the bulk towards the surface. Once at the surface, these holes may participate in the water oxidation reaction,[6] see Figure 1.2. The band bending amplitude can be tuned using an external bias or by doping the semiconductor. The bands can even be flattened by applying a specific voltage, the so-called flatband potential V_{fb}.

Much effort has been devoted to understand the semiconductor-electrolyte interface: starting from analytical models,[14–17] its experimental characterization[11,18–28] to quantum mechanical ab-initio simulations.[6,29–33] Helmholtz,[14] Gouy[15] and Chapman[16] attempted to model the solid-liquid interface, however their models were too simple to provide a realistic description. Helmholtz considered two layers of opposite charge to model the solid and liquid part, which yielded a parallel plate capacitor.[14] Gouy and Chapman considered that the ions in the solution are distributed according to the Boltzmann distribution in the potential generated by the Poisson equation.[15,16] However, in this model, the sizes of the ions approaching the semiconductor surface were not taken into account. Therefore the ions could approach infinitely close to the interface. Stern combined both approaches to describe the interface in a more realistic way. In the Stern-picture, the semiconductor-electrolyte interface consists of a space charge layer in the semiconductor; a Helmholtz layer in the electrolyte which consists of ions and solvent molecules attached to the interface; the latter is followed by a diffuse Gouy-Chapman layer that extends into the solution, see Figure 1.3. Pleskov et al.[13] developed an analytical solution of the Poisson-Boltzmann equation for the Stern-picture of the interface. In this way, one can get information on the width of the space charge layer and the potential drop across the interface (ϕ_{sc}, ϕ_H and ϕ_{el}).

The experimental techniques employed to characterize the interface include electrochemical impedance (EIS),[18–25] transient absorption spectroscopy (TAS),[11] cyclic voltammetry[19,26] and photoelectrocatalytic measurements.[27,28] The experimental measurements provide information on flatband potentials, doping density, interface capacitance and charge dynamics at the interface. For example, EIS provides access to the electrostatics of the interface by interpreting their impedance measurements through equivalent-circuit models, however the results depend on the circuit used to analyze the data.[18–23] The interface capacitances can be extracted through these models and analyzed through the Mott-Schottky analysis. In this way one can get access to the flatband potentials, doping densities and space charge layer widths.

On the other hand ab-initio simulations based on density functional theory (DFT) provide an atomistic description of reaction overpotentials,[29–31] Helmholtz capacitance,[32] charge dynamics[31] and proton exchange dynamics between the hematite surface and the electrolyte.[33] Despite providing a description of these processes and properties, density functional theory is unable to provide information about the macroscopic electrostatics at the interface.[6,30] Besides this, realistic density functional theory simulations of the interface have been thought unattainable due to its extension. It is believed that the interface can extend over tens of nanometers to micrometers. However, in recent water splitting experiments, Zhang et al.[34] measured space charge layers smaller than 10 Å in highly doped nanostroctured hematite photoanodes, which in principle are accessible to quantum mechanical ab-initio simulations.

The fact that these small space charge layers were observed under water splitting conditions, goes against the common belief that broad space charge layers are essential in photoelectrochemistry. Indeed, space charge layers play a crucial role, since electron-hole separation occurs here. They also avoid recombination and promote charge carrier transfer to the semiconductor surface. Although it is well known that high doping concentrations lead to ultrathin space charge layers, this condition is rarely identified in experiments and its consequences have not been analyzed. Using the set of continuous equations developed by Pleskov et al. for the Stern-picture of the interface,[13] in this work we showed that similar space charge layers must have been present in other water splitting experiments. We also examined the consequences that high doping has on the interface. And in addition to that, using the same equations we explored the trends followed by water splitting experiments under different doping conditions. Given that the space charge layers can reach sizes of less than one nanometer, we used density functional theory to get an atomistic insight from the space charge layer in (0001) hematite surfaces. Considering that ultrathin space charge layers have proved to display high efficiencies, the atomistic characterization of the space charge layer in highly doped slabs might be crucial to understand the electronic phenomena in this limit. We explored the evolution of the space charge layer while we added elements of reality to the surface: first we started with the (0001) stoichiometric surface, then we added one OH group to each surface, then we added one additional charge per surface and finally we doped the slabs at concentrations of the order of 10^{21}cm^{-3}.

This thesis is organized as follows: chapter two is devoted to introduce the electrostatic model, based on the Poisson-Boltzmann equations and the Stern model, we employed to study the hematite-electrolyte interface. In this chapter we also give a brief description of density functional theory and the technical details of the calculations we used to analyze the space charge layer in hematite. In chapter three we report the trends observed in a series of experimental data, using the analytical solutions of the electrostatic model used in chapter one. In this chapter, we also examine the consequences of high doping for the interface and on the Mott-Schottky analysis. Chapter four and five are devoted to the analysis of the space charge layer via Density Functional Theory. In the first we report the results obtained in undoped slabs, in the latter we report the consequence of doping the slabs. Finally, we summarize the main conclusions of this work.

Chapter 2

Methods

This chapter is focused on the physical background and ab initio tools we used to study space charge layers in hematite photoanodes. We review the semiconductor-electrolyte interface, where the space charge layer is located in the solid part. This interface can be described by a set of equations based on the Stern model and the Poisson-Boltzmann distribution. In this chapter we will introduce the solution of these equations, we will determine some parameters necessary to implement them and we will connect them to the available water-splitting experimental data. Density functional theory was used to simulate space charge layers in hematite thin films. We will discuss the fundamentals of this theory as well as the approximations needed to implement it. We will also review the main idea of the "DFT+U" correction to the exchange and correlation energy functional which is needed due to the localized nature of the 3d orbitals in the iron atoms of hematite.

2.1 The semiconductor-electrolyte interface

The study of the semiconductor-electrolyte interface is crucial to understand the chemical and physical phenomena involved in the photoelectrochemical water splitting. Many models have been proposed to describe the potential distribution across this interface, the first one and the simplest was proposed by Helmholtz.[14] According to this model, the interface consists of two layers of opposite charge displaying a parallel plate capacitor. Gouy and Chapman[15,16] improved the picture by assuming that the space charge in the liquid is a diffuse structure that goes from the semiconductor's surface to the bulk solution and for which they solved analytically the Poisson-Boltzmann equation. However this model failed in accounting for the finite size of the ions approaching to the surface.

To fix this situation, Stern[17] combined the ideas of Helmholtz, Gouy and Chapman to model the liquid part of the interface finite compact layer followed by the diffuse or Gouy-Chapman layer. Despite the simplicity of the Stern model, it contains enough elements of reality to provide an analytical set of electrostatic equations that can connect microscopic properties of the electrolyte-semiconductor interface to water splitting experimental data.

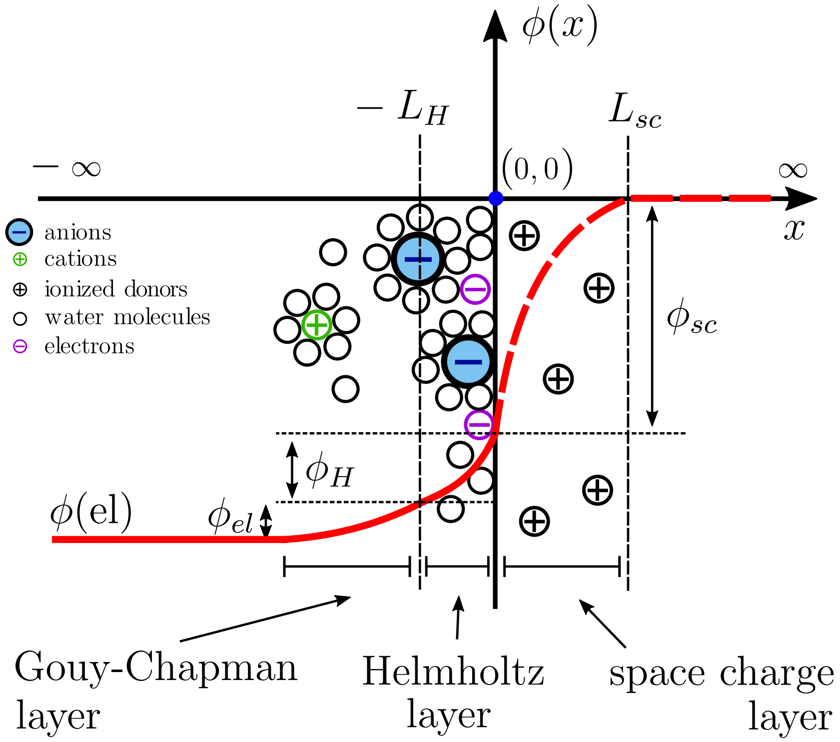

Figure 2.1: Diagram of the semiconductor-electrolyte interface. The Helmholtz layer plane is defined by $x = -L_H$; the surface of semiconductor by $x = 0$; and the width of the space charge layer by $x = L_{sc}$.

2.1.1 Poisson-Boltzmann equations

In the Stern picture, the interface is constituted by a space charge layer in the semiconductor, compact Helmholtz layer in the electrolyte, followed by diffuse Gouy-Chapman layer, see Figure 2.1. Here we will review the analytical solutions obtained by Pleskov and Gurevich[13] for the Poisson Boltzmann-distribution to the electrolyte-semiconductor interface in the Stern description. Figure 2.1 shows the spatial configuration of the interface used to describe the system. The Helmholtz layer plane is defined by the ordinate $-L_H$; the surface of semiconductor by the ordinate 0; and the width of the space charge layer by the ordinate L_{sc}. The potential in the bulk of the semiconductor takes a reference value of 0 and the potential in the bulk of the solution is set to an arbitrary constant $\phi(el)$.

Description of the space charge layer

In general, the space charge layer in the semiconductor consists of mobile carriers (electrons n and holes p) and fixed impurities (donors N_D or acceptors N_A depending on the type of doping). Assuming that the local concentrations of electrons and holes can be described by the Boltzmann distribution, and the donors and acceptors are fully ionized, the Poisson equation[12,13] in the space charge layer is commonly expressed as follows:

$$\frac{\mathrm{d}^2\phi}{\mathrm{d}\mathbf{x^2}} = -\frac{e}{\epsilon_{sc}\epsilon_0}\left(p_0 \exp^{\frac{-e\phi(x)}{k_BT}} - n_0 \exp^{\frac{e\phi(x)}{k_BT}} + N_D - N_A\right), \tag{2.1}$$

where p_0 and n_0 are the equilibrium concentration of holes in the valence band; N_D and N_A are the density of donor and acceptor dopants in the semiconductor; ϵ_{sc} denotes the dielectric constant of the semiconductor; e is the charge of the electron; ϕ_{sc} is the potential drop in the space charge layer of the semiconductor; k_B is the Boltzmann constant and T is the temperature. The Boltzmann distribution was used assuming that the system is at equilibrium and that the semiconductor is non-degenerate,[13] i.e. low carrier densities. At high charge carrier densities, the Fermi-Dirac distribution should be used to account for quantum effects.

The potential distribution in the space charge layer can be calculated using the depletion approximation. Where it is assumed that the charge carriers fully migrated to the solution. In this approximation, the space charge distribution is assumed to decay at a length L_{sc} from the surface, in the simplest case the distribution is assumed to be a step function.[12]

$$\rho(x) = \begin{cases} eN_D \ , & 0 < x < L_{sc}, \\ 0 \ , & x > L_{sc} \ . \end{cases}$$

In the case of n-type semiconductor, where electrons are donated by the impurities, in the depletion approximation equation 2.1 is reduced to:

$$\frac{\mathrm{d}^2\phi}{\mathrm{d}x^2} = -\frac{eN_D}{\epsilon_{sc}\epsilon_0}. \tag{2.2}$$

According to the depletion approximation, the ionized donors in the space charge layer are located in a region of width L_{sc}. Beyond $x = L_{sc}$, this region is neutral. As a consequence, the electric field vanishes far from the surface. In the depletion approximation it is considered that for $x > L_{sc}$ the electric field is small. Hence the boundary conditions for this equation are:

$$\phi(0) = -|\phi_{sc}|,$$

$$\phi(L_{sc}) = 0,$$

$$\frac{\mathrm{d}\phi}{\mathrm{d}x} = 0 \ , \ \text{when } x = L_{sc},$$

where ϕ_{sc} is the potential drop in the space charge layer. Here the potential in the bulk of the semiconductor is set to zero as a reference. In the depletion approximation, $\phi_{sc} < 0$ for an n-type semiconductor. Since the reference in the bulk is taken at a potential of 0 V, the value of $\phi(x)$ at the interface can be expressed as $-|\phi_{sc}|$. We can find an expression for $(\mathrm{d}\phi/\mathrm{d}x)$ in equation 2.2 as follows:

$$\frac{\mathrm{d}}{\mathrm{d}x}\left(\frac{\mathrm{d}\phi}{\mathrm{d}x}\right) = -\frac{eN_D}{\epsilon_{sc}\epsilon_0},$$

$$\int \mathrm{d}\left(\frac{\mathrm{d}\phi}{\mathrm{d}x}\right) = -\int \frac{qN_D}{\epsilon_{sc}\epsilon_0}\mathrm{d}x,$$

$$\frac{\mathrm{d}\phi}{\mathrm{d}x} = -\frac{qN_D}{\epsilon_{sc}\epsilon_0}x + c_1, \tag{2.3}$$

where we found the integration constant c_1. Evaluating $(\mathrm{d}\phi/\mathrm{d}x)$ at $x = L_{sc}$

$$\frac{\mathrm{d}\phi}{\mathrm{d}x}|_{x=L_{sc}} = -\frac{qN_D}{\epsilon_{sc}\epsilon_0}(L_{sc}) + c_1 = 0,$$

$$c_1 = \frac{qN_D L_{sc}}{\epsilon_{sc}\epsilon_0}. \tag{2.4}$$

We substituted c_1 (Eq.2.4) in equation 2.3 and solved it for $\phi(x)$ as follows

$$\frac{\mathrm{d}\phi}{\mathrm{d}x} = -\frac{qN_D}{\epsilon_{sc}\epsilon_0}x + \frac{qN_D L_{sc}}{\epsilon_{sc}\epsilon_0}, \tag{2.5}$$

$$\int \mathrm{d}\phi = \int \left(-\frac{qN_D}{\epsilon_{sc}\epsilon_0} x + \frac{qN_D L_{sc}}{\epsilon_{sc}\epsilon_0} \right) \mathrm{d}x,$$

$$\phi(x) = \left(-\frac{qN_D}{2\epsilon_{sc}\epsilon_0} x^2 + \frac{qN_D L_{sc}}{\epsilon_{sc}\epsilon_0} x + c_2 \right), \tag{2.6}$$

where we calculated c_2. Evaluating $\phi(0) = -|\phi_{sc}|$. From 2.6 it can be seen that $c_2 = -|\phi_{sc}|$. Rearranging equation 2.6 and substituting $c_2 = -|\phi_{sc}|$ we obtained

$$\phi(x) = -\frac{qN_D}{2\epsilon_{sc}\epsilon_0} \left(x^2 - 2L_{sc}x + \frac{2\epsilon_{sc}\epsilon_0 |\phi_{sc}|}{eN_D} \right). \tag{2.7}$$

The value of L_{sc} can be found evaluating equation 2.7 in $x = L_{sc}$ considering that $\phi(L_{sc}) = 0$

$$\phi(L_{sc}) = -\frac{qN_D}{2\epsilon_{sc}\epsilon_0} \left(L_{sc}^2 - 2L_{sc}^2 + \frac{2\epsilon_{sc}\epsilon_0 |\phi_{sc}|}{eN_D} \right),$$

$$0 = \left(-L_{sc}^2 + \frac{2\epsilon_{sc}\epsilon_0 |\phi_{sc}|}{eN_D} \right),$$

$$L_{sc} = \sqrt{\frac{2\epsilon_{sc}\epsilon_0 |\phi_{sc}|}{eN_D}}. \tag{2.8}$$

Substituting the expression of L_{sc} into equation 2.7, the potential distribution in the space charge layer of the semiconductor is given by:

$$\phi(x) = -\frac{eN_D}{2\epsilon_{sc}\epsilon_0} \left(x - L_{sc} \right)^2 \ , \quad 0 \le x \le L_{sc}. \tag{2.9}$$

The potential profile in the space charge layer displays a parabolic behavior that decays from the surface to the bulk of the semiconductor, as indicated by the negative sign of the potential in Equation 2.9.[12,13] A thermal correction for the width space charge layer can be found if equation 2.1 is integrated from $x = 0$ to ∞ to find $(\mathrm{d}\phi/\mathrm{d}x)$. From here, expressions for the charge per unit surface area σ_{sc} and the capacitance in the space charge layer C_{sc} can be found. The square of the inverse of the latter is known as the Mott-Schottky equation and it is given by

$$\frac{1}{C_{sc}^2} = \frac{2}{e\epsilon_{sc}\epsilon_0 N_D}\left[\mid \phi_{sc} \mid - \frac{k_B T}{e}\right]. \tag{2.10}$$

The thickness of the space charge layer, L_{sc} can be determined in the general case from the condition $C_{sc} = \epsilon_{sc}\epsilon_0/L_{sc}$

$$L_{sc} = \left(\frac{2\epsilon_{sc}\epsilon_0}{eN_D}\right)^{1/2}\left(\mid \phi_{sc} \mid - \frac{k_B T}{e}\right)^{1/2}. \tag{2.11}$$

Description of the electrolyte

In the Stern picture, the liquid part of the semiconductor-electrolyte interface can be modeled as a compact layer with a finite size followed by a diffuse layer that decays into the bulk solution. The Helmholtz layer consists of adsorbed ions, adsorbed solvent molecules from the electrolyte and solvated ions close to the semiconductor surface. In the case of a 1 : 1 electrolyte solution, the diffuse layer consists of monovalent co-ions solvated by water molecules. As mentioned before, Stern considered the finite size of ions and water molecules, therefore he assumed the Helmholtz layer extends over a finite region of atomic dimensions, which is defined from $x = 0$ to $x = -L_H$ in Figure 2.1. The ions in the Gouy-Chapman layer are distributed according to the Poisson-Boltzmann equation, which accounts for the competition between the thermal processes and the Coulomb interaction at regions away from the surface. Taking into account the boundary conditions in every region and the continuity of the electric displacement field, Pleskov and Gurevich found that the potential drops for the Helmholtz ϕ_H and the diffuse layers ϕ_{el}.

$$\phi_H = \frac{L_H\sqrt{2}}{\epsilon_H\epsilon_0}\sqrt{e\epsilon_{sc}\epsilon_0 N_D \mid \phi_{sc} \mid}\ , \tag{2.12}$$

$$\phi_{el} = \frac{2k_BT}{e}\text{arcsinh}\left[\left(\frac{e\epsilon_{sc}N_D \mid \phi_{sc} \mid}{4c_0\epsilon_{el}k_BT}\right)^{1/2}\right], \tag{2.13}$$

where L_H represents the width of the Helmholtz layer and ϵ_H is its effective dielectric constant; c_0 is the concentration of the electrolyte and ϵ_{el} its dielectric constant. We will show the derivation of these equations starting from the Poisson-Boltzmann equation for the diffuse layer. In the case of a 1:1 electrolytes the Poisson equation can be expressed as follows

$$\frac{\mathrm{d}^2\phi}{\mathrm{d}\mathbf{x^2}} = -\frac{e}{\epsilon_{el}\epsilon_0}\left(c_0 \exp^{\frac{-e[\phi(x)-\phi(el)]}{k_BT}} - c_0 \exp^{\frac{+e[\phi(x)-\phi(el)]}{k_BT}}\right), \tag{2.14}$$

where $\phi(el)$ is the value of the electric potential in the bulk of the solution, see Figure 2.1. Taking into account that $\sinh x = (e^x - e^{-x})/2$, equation 2.14 can be rewritten as

$$\frac{\mathrm{d}^2\phi}{\mathrm{d}\mathbf{x^2}} = \frac{2ec_0}{\epsilon_{el}\epsilon_0}\sinh\left[\frac{e(\phi(x)-\phi(el))}{k_BT}\right]. \tag{2.15}$$

We can solve equation 2.15 for $(\mathrm{d}\phi/\mathrm{d}x)$, noting first that

$$\frac{\mathrm{d}^2\phi}{\mathrm{d}x^2}\frac{\mathrm{d}\phi}{\mathrm{d}x} = \frac{\mathrm{d}}{\mathrm{d}x}\left[\frac{1}{2}\left(\frac{\mathrm{d}\phi}{\mathrm{d}x}\right)^2\right]. \tag{2.16}$$

Multiplying Equation 2.15 by $(\mathrm{d}\phi/\mathrm{d}x)$ and substituting the left hand side by the expression in equation 2.16, we obtained

$$\frac{\mathrm{d}}{\mathrm{d}x}\left[\frac{1}{2}\left(\frac{\mathrm{d}\phi}{\mathrm{d}x}\right)^2\right] = \frac{2ec_0}{\epsilon_{el}\epsilon_0}\sinh\left[\frac{e(\phi(x)-\phi(el))}{k_BT}\right]\frac{\mathrm{d}\phi}{\mathrm{d}x}. \tag{2.17}$$

Rearranging the differentials, and integrating in both sides we found an integral expression for $(\mathrm{d}\phi/\mathrm{d}x)$

$$\int \mathrm{d}\left[\frac{1}{2}\left(\frac{\mathrm{d}\phi}{\mathrm{d}x}\right)^2\right] = \int \frac{2ec_0}{\epsilon_{el}\epsilon_0}\sinh\left[\frac{e(\phi(x)-\phi(el))}{k_BT}\right]\frac{\mathrm{d}\phi}{\mathrm{d}x}\mathrm{d}x,$$

$$\frac{1}{2}\left(\frac{\mathrm{d}\phi}{\mathrm{d}x}\right)^2 = \int \frac{2ec_0}{\epsilon_{el}\epsilon_0}\sinh\left[\frac{e(\phi(x)-\phi(el))}{k_BT}\right]\frac{\mathrm{d}\phi}{\mathrm{d}x}\mathrm{d}x. \tag{2.18}$$

We solved the integral in equation 2.18 by substituting

$$\psi = \frac{e(\phi(x)-\phi(el))}{k_BT},$$

and noting that the differential of ψ takes the following form:

$$\mathrm{d}\psi = \frac{e}{k_BT}\frac{\mathrm{d}\phi}{\mathrm{d}x}\mathrm{d}x.$$

Therefore we rewrote the integral in equation 2.18 as

$$\frac{1}{2}\left(\frac{\mathrm{d}\phi}{\mathrm{d}x}\right)^2 = \int \frac{2ec_0}{\epsilon_{el}\epsilon_0}\frac{k_BT}{e}\sinh\psi\ \mathrm{d}\psi, \tag{2.19}$$

which yields

$$\left(\frac{\mathrm{d}\phi}{\mathrm{d}x}\right)^2 = \frac{4ec_0}{\epsilon_{el}\epsilon_0}\frac{k_BT}{e}\cosh\psi + 2\beta,$$

$$= \frac{4c_0k_BT}{\epsilon_{el}\epsilon_0}\cosh\left[\frac{e(\phi(x)-\phi(el))}{k_BT}\right] + 2\beta, \tag{2.20}$$

where β is an integration constant. The boundary conditions in this problem are given by

$$\frac{\mathrm{d}\phi}{\mathrm{d}x} = 0 \ , \ \text{when } x \to -\infty \tag{2.21}$$

$$\phi(x)|_{x=Lsc} - \phi(el) = \phi_{el}, \tag{2.22}$$

where $\phi(el)$ is the potential at the bulk of the solution ($x \to -\infty$) and ϕ_{el} is the potential drop in the Gouy-Chapman layer, see Figure 2.1. The first boundary condition means that in average the electric potential is constant in the bulk of the solution and can be used to find the integration constant β in equation 2.20. Evaluating 2.20 in the limit of ($x \to -\infty$)

$$\lim_{x\to\infty} \left(\frac{\mathrm{d}\phi}{\mathrm{d}x}\right)^2 = \lim_{x\to\infty} \frac{4c_0 k_B T}{\epsilon_{el}\epsilon_0} \cosh\left[\frac{e(\phi(x) - \phi(el))}{k_B T}\right] + 2\beta,$$

$$0 = \frac{4c_0 k_B T}{\epsilon_{el}\epsilon_0} \cosh\left[\frac{e(\phi(x_{x\to\infty}) - \phi(el))}{k_B T}\right] + 2\beta,$$

$$0 = \frac{4c_0 k_B T}{\epsilon_{el}\epsilon_0} \cosh\left[\frac{e(\phi(el) - \phi(el))}{k_B T}\right] + 2\beta,$$

$$\beta = -\frac{2c_o k_B T}{\epsilon_{el}\epsilon_0}, \tag{2.23}$$

where we took into account the fact that $\cosh 0 = 1$. Inserting β in equation 2.20, we get an expression for $(\mathrm{d}\phi/\mathrm{d}x)$

$$\left(\frac{\mathrm{d}\phi}{\mathrm{d}x}\right)^2 = \frac{8ec_0 kT}{\epsilon_{el}\epsilon_0} \left(\cosh\left[\frac{e(\phi(x) - \phi(el))}{k_B T}\right] - 1\right), \tag{2.24}$$

where latter expression can be rewritten considering $\cosh t - 1 = 2\sinh^2(t/2)$

$$\left(\frac{\mathrm{d}\phi}{\mathrm{d}x}\right) = -\sqrt{\frac{8ec_0k_BT}{\epsilon_{el}\epsilon_0}}\sinh\left[\frac{e(\phi(x)-\phi(el))}{2k_BT}\right]. \tag{2.25}$$

Therefore we have an expression for the first derivative of the potential distribution from the bulk solution to the Helmholtz layer plane $x = -L_H$. The expression for the potential drop in the Helmholtz layer ϕ_H and the potential drop in the Gouy-Chapman layer ϕ_{el} can be found considering the conditions for electric induction continuity across the different boundaries and the difference in the directions of the potential axes of the different contributions

$$-\epsilon_{el}\left(\frac{\mathrm{d}\phi}{\mathrm{d}x}\right)_{x=-L_H} = \epsilon_H\xi_H = \epsilon_{sc}\left(\frac{\mathrm{d}\phi}{\mathrm{d}x}\right)_{x=0}, \tag{2.26}$$

where ξ_H denotes the electric field in the Helmholtz layer and ϵ_H is its dielectric constant. The expression for the potential drop in the Helmholtz layer can be found considering the condition

$$\epsilon_H\xi_H = \epsilon_{sc}\left(\frac{\mathrm{d}\phi}{\mathrm{d}x}\right)_{x=0}. \tag{2.27}$$

The first derivative of the potential at $x = 0$ can be evaluated using the expression for the potential in the semiconductor, which is given by equation 2.9

$$\frac{\mathrm{d}\phi}{\mathrm{d}x} = \frac{\mathrm{d}}{\mathrm{d}x}\left(-\frac{eN_D}{2\epsilon_{sc}\epsilon_0}(x-L_{sc})^2\right) = -\frac{eN_D}{\epsilon_{sc}\epsilon_0}(x-L_{sc}). \tag{2.28}$$

Evaluating equation 2.28 in $x = 0$ and inserting it in 2.27, we obtained

$$\epsilon_H\xi_H = -\epsilon_{sc}\frac{eN_D}{\epsilon_{sc}\epsilon_0}(0-L_{sc}). \tag{2.29}$$

Substituting the expression for the width of the space charge layer L_{sc} as expressed in equation 2.8 in the latter equation, we obtained

$$\epsilon_H \xi_H = \epsilon_{sc} \frac{eN_D}{\epsilon_{sc}\epsilon_0} \sqrt{\frac{2\epsilon_{sc}\epsilon_0 |\phi_{sc}|}{eN_D}},$$

$$= \sqrt{\frac{2e\epsilon_{sc} N_D |\phi_{sc}|}{\epsilon_0}}. \tag{2.30}$$

Since the charge density at any point from the semiconductor surface to Helmholtz layer plane $-L_H$ is zero, the field ξ_H is constant and can be estimated as $\xi_H = \phi_H / L_H$. Therefore equation 2.30 can be rearranged to find ϕ_H

$$\begin{aligned} \phi_H &= \frac{L_H}{\epsilon_H} \sqrt{\frac{2e\epsilon_{sc} N_D |\phi_{sc}|}{\epsilon_0}}, \\ &= \frac{L_H}{\epsilon_H} \sqrt{\frac{2e\epsilon_{sc} N_D |\phi_{sc}|}{\epsilon_0}} * \frac{\sqrt{\epsilon_0}}{\sqrt{\epsilon_0}}, \\ &= \frac{L_H \sqrt{2}}{\epsilon_H \epsilon_0} \sqrt{e\epsilon_{sc}\epsilon_0 N_D |\phi_{sc}|}. \end{aligned} \tag{2.31}$$

We can find ϕ_{el}, if we consider the continuity of the electric induction in the Gouy-Chapman layer and the Helmholtz layer as expressed in equation 2.22 and substituting the expression for $(\mathrm{d}\phi/\mathrm{d}x)$ in equation 2.25, we have

$$\epsilon_H \xi_H = -\epsilon_{el} \left(\frac{\mathrm{d}\phi}{\mathrm{d}x} \right)_{x=-L_H},$$

$$= \sqrt{\frac{8ec_0 kT}{\epsilon_{el}\epsilon_0}} \sinh \left[\frac{e(\phi(-L_H) - \phi(el))}{2k_B T} \right]. \tag{2.32}$$

Considering the boundary condition $\phi(-L_H) - \phi(el) = \phi_{el}$. We can express equation 2.32

as follows

$$\epsilon_H \xi_H = \sqrt{\frac{8ec_0k_BT}{\epsilon_{el}\epsilon_0}} \sinh\left[\frac{e\phi_{el}}{2k_BT}\right]. \tag{2.33}$$

Substituting the expression for $\epsilon_H \xi_H$ found in equation 2.30 in the the left hand side of equation 2.33

$$\sqrt{\frac{2e\epsilon_{sc}N_D|\phi_{sc}|}{\epsilon_0}} = \sqrt{\frac{8ec_0k_BT}{\epsilon_{el}\epsilon_0}} \sinh\left[\frac{e\phi_{el}}{2k_BT}\right]. \tag{2.34}$$

Finally, inverting the $\sinh x$ function and solving for ϕ_{el}, we obtain

$$\phi_{el} = \frac{2k_BT}{e} \text{arcsinh}\left[\left(\frac{e\epsilon_{sc}N_D \mid \phi_{sc} \mid}{4c_0\epsilon_{el}k_BT}\right)^{1/2}\right].$$

The Galvani potential or the total potential drop at the interface is given by

$$\phi_{total} = |\phi_{sc}| + \phi_H + \phi_{el}. \tag{2.35}$$

It is important to mention that L_H and ϵ_H were introduced in the definition of the system and the boundary conditions. And at the same time they cannot be measured directly in electrochemical experiments. Therefore they have to be estimated by other means. Other observation is that the expressions for L_{sc}, ϕ_H and ϕ_{el} depend on the value of ϕ_{sc}, thus the latter should be related to an experimental quantity. We also find important to point out that the depletion approximation is a necessary condition for the Mott-Schottky equation to hold. Specially at moderately high doping densities because under these conditions the majority of the potential drop in the interface is located in the space charge layer.

2.1.2 Determination of the parameters from the Helmholtz layer

We determined the values of the width of the Helmholtz layer L_H and its dielectric constant ϵ_H from ab-initio molecular-dynamics simulations (AIMD) of the hematite-electrolyte interface found in Ref.[32] We used the results on capacitances and water density profiles they provided for the stoichiometric FeO_3Fe and the hydroxylated terminations to determine the Helmholtz layer parameters.

We extracted L_H from the analysis of the water densities profiles for both terminations reported in Ref.[32] First we determined the distance between the surface of hematite and the Outer Helmholtz Plane (OHP) to estimate the extension of the Helmholtz layer. The OHP corresponds to the plane that passes through the centers of the ions that are not specifically adsorbed to hematite. We assumed that the first hydration layer in the water density profiles accounts for the adsorbed solvent molecules on the surface and the water molecules solvating the ions in the OHP. Therefore we set the OHP at the peaks of the ion distributions that are immediately after the first hydration layer, which is determined by the first peak in the water density profile reported by Ulman et al. The surface was defined as the Fe plane in the case of the FeO_3Fe-termination and the OH plane in the case of the OH-termination, see Ref.[32] We set the OH plane as the plane that passes through the Oxygen atom. The simulations were done for different monovalent ions for every termination, therefore we averaged the resulting L_H in all the cases. This yielded values of $L_H = 4.4$ Å and $L_H = 6.4$ Å respectively. We then estimated the value of the dielectric constants by assuming the Helmholtz layer behaves like a parallel-plate capacitor which obeys

$$C_H = \frac{\epsilon_H \epsilon_0}{L_H}, \tag{2.36}$$

from which we obtained a value of $\epsilon_H = 25.3$ for the stoichiometric termination and a value of $\epsilon_H \sim 29.1$ for the OH termination. It is important to point out that the values estimated for L_H and ϵ_H behave qualitatively as expected. It is always assumed that the Helmholtz layer extends over distances of the order of radii of solvated ions. Magnussen and Gross observed the flattening of the average electrostatic potential after the first water layer on Pt(111) via AIMD.[35] They claim this bulk-like behaviour implies that the width of the compact part of the electric double layer should be lower than 10 Å.

It is well known from experiments that the local dielectric constant in electrolytic solutions decreases as it moves from the solution bulk to a charged surface.[36] The latter behavior was used to explain recent experimental measurements of the kinetics of charge transfer which mapped the behavior of the local dielectric constant from the diffuse layer to the Helmholtz layer.[36] Though, the values of the dielectric constants at the Helmholtz layer were not reported in this study. We reported values of ϵ_H much lower than the dielectric constant of bulk water $\epsilon_{water} \sim 78$ and bulk electrolytic solutions.[37–40] Values with similar magnitudes were estimated in literature for other systems. For example, Conway et al. estimated ϵ_H for a silver electrode in aqueous acid solution to be around ~ 15.[41]

We also estimated the Helmholtz layer parameters in an alternative way from experimental data to check whether we were able to get compatible values with the ones we extracted via ab-initio simulations. There is no way to determine the values of L_H and ϵ_H directly from the available electrochemical data. However we fixed one of these two quantities, and checked which values of L_H and ϵ_H are compatible with the measured values of Helmholtz layer capacitances C_H reported in literature.[21–23,42] We selected the values of capacitances reported for samples with $(1\bar{2}02)$ surface orientation because it is structurally closer to the stoichiometric termination FeO_3Fe termination, which is the one we used to model the surface. We also filtered the available data, by considering experiments held in solutions with pH>3 because hematite is unstable at strong acidic conditions. We calculated the width of the Helmholtz layer L_H using the planar capacitor equation 2.36, using three different orders of magnitude of the dielectric constant ϵ_H =1, 10 and 100 and for three intermediate values of ϵ_H =5, 25, 30, 40 and 50. The resultant values of L_H can be seen in Table 2.1.

To estimate the value of the dielectric constant, we kept the columns for which the calculated values of L_H fell in a physically reasonable range, i.e. between the Bohr radius and $\sim$10 Å,[35] and discarded the rest. Then we kept the values of ϵ_H smaller than the bulk dielectric constant of the NaOH solutions used in these experiments. Among the ϵ_H

$C_H(\mu F/cm^2)$ | ϵ_H(Å) :	1	5	10	25	30	40	50	100
35[21]	0.25	1.26	2.53	6.32	7.59	10.12	12.65	25.30
53[22]	0.17	0.84	1.67	4.18	5.01	6.68	8.35	16.71
75.1[22]	0.12	0.59	1.18	2.95	3.54	4.72	5.90	11.81
88[42]	0.1	0.5	1.01	2.52	3.02	4.02	5.03	10.06
180[22]	0.05	0.25	0.49	1.23	1.48	1.97	2.46	4.92
227.5[23]	0.04	0.19	0.39	0.97	1.17	1.56	1.95	3.89
237.7[23]	0.04	0.19	0.37	0.93	1.12	1.49	1.86	3.72
331[23]	0.03	0.13	0.27	0.67	0.80	1.07	1.34	2.67

Table 2.1: Values of L_H (Å) calculated from experimental capacitances, assuming the Helmholtz layer behaves like a planar capacitor. The value of ϵ_H vary in the direction of the columns and the value of the capacitance in the Helmholtz layer C_H changes across the rows.

values considered, $\epsilon_H = 25$ showed to be the best estimation of the dielectric constant given that it yielded the highest amount of acceptable L_H within a broad range of experimental capacitances. The values of 30 and 40 for the dielectric constant also yielded acceptable values of L_H. However, it can be observed in table 2.1 that the dependence of L_H on the dielectric constant is weak. Therefore, the results should change quantitatively, but not qualitatively.

To estimate the value of L_H, we decided to set L_H to values of 1.25 Å, 2.5 Å, 5 Å and 10 Å and to test the behavior of the total potential drop using the continuous equations at the experimental conditions. We noticed that in general the potential drops through the different layers behaved as expected at doping densities of $N_D \sim 10^{18}\text{cm}^{-3}$, i.e. the drop in the space charge layer of the semiconductor dominates over the other two. We decided to choose an intermediate value of 5 Å given that no drastic differences were found while varying the value of L_H. This value also falls in the range of the L_{sc} estimated for $\epsilon_H = 25$ using the capacitances measured in experiments, see Tab. 2.1. Therefore we can see that Helmholtz layer parameters obtained through the analysis of the experimental data is compatible with the values found via ab-initio results.

2.1.3 Connection of equations with experiment

As we mentioned previously, the potential drop in the space charge layer ϕ_{sc} is the parameter needed to define the drops in the other two layers. Therefore we should identify a connection between this quantity and the experimentally applied potential.

We found this connection through the flat band potential V_{fb}, whose measurements are reported in the considered experiments. At an applied potential equal to the flat band potential $\phi_{sc} = 0$, as a consequence ϕ_{el}, ϕ_H and ϕ_{tot} are also zero, as clearly shown by Eq. 2.12 and 2.13. These conditions can be used to connect the macroscopic quantities provided by experiments and the microscopic quantities described in the equations describing the semiconductor-electrolyte interface. The next crucial assumption is that the main changes in voltage occur at the hematite-electrolyte interface when the applied bias is moved away from flat-band conditions. The applied voltage V_{app} reported in experiments can thus be associated to the total potential drop across the interface:

$$V_{app} - V_{fb} = \phi_{total} = |\phi_{sc}| + \phi_H + \phi_{el}. \tag{2.37}$$

With this equation and the ones for the potential drops in ϕ_{el} and ϕ_H, we can fully describe the potential drop across the interface as a function of the experimental conditions. In every case, the value of ϕ_{sc} has to be found by solving numerically a system of these equations. To ensure uniformity in the selected data, we chose the experiments held at 1 Sun of illumination and using 1M NaOH solutions as the electrolyte, except Ref.[24] and Ref.[25] which used 0.1M NaOH. We set the values of ϵ_{el} to the dielectric constants reported by Buchner et al. for NaOH solutions.[38]

We used a dielectric constant of $\epsilon_{sc} = 57$ for hematite. This value was measured by Ref. 43, where they used pure-undoped hematite and reported dielectric constants ranging from 32 to 57. We also found values between 12-120 for ϵ_{sc} in literature,[43–46] including some with strong temperature dependence.[46] Though the problem of choosing an appropriate dielectric constant for hematite remains open, we chose the constant from Ref. 43 because they measured it with the c-axis of the hexagonal structure perpendicular to the substrate.

We disregarded any dependence of ϵ_{sc} on doping, given that any variation of the dielectric constant produces a change of the order of a square root in the equation for L_{sc} (Eq. 2.11). We report calculations with ϵ_{sc} in the Appendix A to show the robustness of our calculations. The calculations in Appendix A are consistent with calculations performed using $\epsilon_{sc} = 57$.

We would like to remark that in literature the width of the space charge layer is often calculated using $\mathrm{V}_{app}-\mathrm{V}_{fb}$ instead of ϕ_{sc}.[47,48] As we will show, this is justified at low doping, where the contribution of the space charge layer dominates in the total potential drop. But this is not true at high doping concentrations, where the drop in the Helmholtz layer is not negligible compare to the one in the space charge layer of the semiconductor.

2.2 Density functional Theory

Density functional theory (DFT) allow us to have access to the ground state properties of real materials via the ground state electronic density. Using the electronic density is practical because this quantity depends on the positions of the atoms instead of complicated wavefunctions that depend on 3N degrees of freedom. Since matter is composed of electrons and nuclei, it constitutes an interacting many-body system. Based on the Born-Oppenheimer approximation, DFT is able to treat an interacting-electron system in a simpler one body formalism. Though this is an exact theory, some approximations in the modeling of the many body effects should be done in order to use it in practice. In the following chapter we will introduce the concepts in which Density functional theory is based on as well as the approximations required to implement it.

2.2.1 Born-Oppenheimer approximation

Density functional theory relies on the Born-Oppenheimer approximation, which allows to treat the electronic and nuclear problem separately. Due to the big difference in the masses of the electrons and nuclei, the electrons move faster than the nuclei degrees of freedom and therefore the electrons see the nuclei as if they were fixed. Therefore an ansatz for the wavefunction can be proposed, where it can be expressed as the product of a nuclear wavefunction and an electronic wave function, where the nuclear coordinates act as a parameter in the latter.

$$\Psi(\mathbf{r},\mathbf{R}) = \Phi_R(\mathbf{r}) \cdot \chi(\mathbf{R}), \tag{2.38}$$

where $\mathbf{R}$ represents the coordinates of the nuclei, $\mathbf{r}$ the electronic coordinates, $\chi(\mathbf{R})$ is the nuclear wavefunction and $\Phi_R(\mathbf{r})$ correspond to the electronic wavefunction. The Hamiltonian for a set of N_n nuclei and N_e is given by

$$H = -\sum_{i=1}^{N_e} \frac{\hbar^2}{2m_e} \nabla_i^2 - \sum_{I=1}^{N_n} \frac{\hbar^2}{2M_I} \nabla_I^2 + \frac{1}{2} \sum_{I,J} \frac{Z_I Z_J e^2}{|\mathbf{R}_I - \mathbf{R}_J|} + \frac{1}{2} \sum_{ij} \frac{e^2}{\mathbf{r}_i - \mathbf{r}_j} - \sum_{Ii} \frac{Z_I e^2}{|\mathbf{R}_I - \mathbf{R}_J|}, \tag{2.39}$$

where the first term corresponds to the kinetic energy of the electrons; the second term to the kinetic energy of nuclei; the third term accounts for the interactions between the nuclei; the fourth term describes the electron-electron Coulomb interaction; and the fifth term represents the interaction between nuclei and electrons, this term is fundamental because is attractive contribution to the Hamiltonian that holds all the particles together.

We can apply the nuclear kinetic energy operator to the total wavefunction proposed in the ansatz given by eq. 2.38 and using the fact that $m_e \ll M_I$, we can neglect the so-called non adiabatic terms.

$$T_I\Psi(\mathbf{r},\mathbf{R}) = -\sum_{I=1}^{N_n} \frac{\hbar^2}{2M_I}\nabla_I^2\Psi(\mathbf{r},\mathbf{R}) = -\sum_{I=1}^{N_n} \frac{\hbar^2}{2M_I}\nabla_I^2\left[\Phi_R(\mathbf{r})\cdot\chi(\mathbf{R})\right], \tag{2.40}$$

$$T_I\Psi(\mathbf{r},\mathbf{R}) = -\sum_{I=1}^{N_n} \frac{\hbar^2}{2M_I}\left[\chi(\mathbf{R})\nabla_I^2\Phi_R(\mathbf{r}) + \Phi_R(\mathbf{r})\nabla_I^2\chi(\mathbf{R}) + 2\nabla_I^2\Phi_R(\mathbf{r})\cdot\nabla_I^2\chi(\mathbf{R}\right], \tag{2.41}$$

$$T_I\Psi(\mathbf{r},\mathbf{R}) = -\sum_{I=1}^{N_n} \frac{\hbar^2}{2M_I}\left[\Phi_R(\mathbf{r})\nabla_I^2\chi(\mathbf{R})\right]. \tag{2.42}$$

Applying the approximation obtained for the nuclear kinetic energy in the eq. 2.42 to the Hamiltonian in eq. 2.39 and integrating out the electronic degrees of freedom. The nuclear and electronic problem can be separated. The nuclear problem is reduced to solve this Schrödinger equation:

$$-\sum_{I=1}^{N_n} \frac{\hbar^2}{2M_I}\nabla_I^2\chi(\mathbf{R}) + U(R)\chi(\mathbf{R}) = E\chi(\mathbf{R}). \tag{2.43}$$

The nuclear degrees of freedom are treated quantum mechanically. Due to the localized nature of solutions, they display a classical behavior. Where $U(R)$ is the Born-Oppenheimer potential energy surface, it represents the ground state potential energy of the electronic problem when the nuclei are determined by the vector R. $U(R)$ can be found by solving the Schrödinger problems for the electronic degrees of freedom.

$$\left(-\sum_{i=1}^{N_e} \frac{\hbar^2}{2m_e}\nabla_i^2 + \frac{1}{2}\sum_{ij}\frac{e^2}{\mathbf{r}_i - \mathbf{r}_j} - \sum_{Ii}\frac{Z_I e^2}{|\mathbf{R}_I - \mathbf{R}_J|} + \frac{1}{2}\sum_{IJ}\frac{Z_I Z_J e^2}{|\mathbf{R}_I - \mathbf{R}_J|}\right)\Phi_R^{\alpha}(\mathbf{r}) = U_{\alpha}(\mathbf{R})\Phi_R^{\alpha}(\mathbf{r}). \tag{2.44}$$

The electronic problem is thus an interacting electron system since it cannot be decoupled in a one-body problem. Fortunately DFT provides the framework to tackle this problem.

2.2.2 Hohenberg-Kohn Theorem

Density functional is based the Hohenberg-Kohn theorem which states that the total energy of an interacting electron system is a functional of the electronic density. They showed that there is a one to one relation between the electronic density and the external potential. Which means that a determined ground state electronic density is caused by one and only one external potential. Therefore, given an external potential, we can write the ground state total energy as functional of the electronic density.

Hohenberg and Kohn did not give a hint on how to build this functional. But a functional based on the interacting electrons problem can be proposed

$$E[\rho] \quad = T[\rho] + E^{ext}[\rho] + E^{Hartree}[\rho] + E^{XC}[\rho], \tag{2.45}$$

where $T[\rho]$ corresponds to the kinetic energy term; $E^{ext}[\rho]$ to the contribution from the external potential which is produced by nuclei; $E^{Hartree}[\rho]$ is the Hartree term representing the electron-electron pairwise Coulomb interaction; and the $E^{XC}[\rho]$ is the exchange and correlation energy functional, which encloses the many-body effects and includes the corrections to the kinetic energy and the Coulomb interactions. The real ground state electronic density is the one that minimizes the total energy functional. Therefore a variational method has to be applied to the total energy functional with respect to the electronic density conserving the number of electrons. It is important to mention that certain electronic densities cannot be represented by any external potential, which is a signature that they do not correspond to ground state electronic densities.

2.2.3 Kohn-Sham equations

Kohn and Sham proposed an ansatz in which they assumed that the ground state density of the original interacting system is equal to that a non-interacting system. Which translates in a mapping of an interacting electron problem to one-body formalism. This allow us to introduce a set of auxiliary Kohn-Sham orbitals $\phi_i(r)$. We can express the electronic density in terms of these orbitals

$$\rho(r) = \sum_i^{N_e} f_i \left|\phi_i(r)\right|^2, \tag{2.46}$$

where f_i is occupation of the orbital state ϕ_i. Since there is no direct expression of the kinetic energy in terms of the electronic density, this change of variables allow us to have an approximate expression of the kinetic energy

$$T_0[\rho(r)] = -\sum_i f_i \int \phi_i^*(r) \frac{\hbar^2\nabla^2}{2m} \phi_i(r) dr, \tag{2.47}$$

and therefore we can re-express the total energy functional as follows:

$$E^0[\rho] = T_0[\rho(r)] + \int \mathrm{d}^3 r \rho(r) V^{ext} + \frac{1}{2} \int \int \frac{\rho(r)\rho(r')}{|r - r'|} + E_{xc}[\rho].$$

In this case the exchange and $E_{xc}[\rho]$ correlation functional will include the corrections generated by expressing the kinetic energy in terms of the Kohn-Sham auxiliary orbitals. We can find the shape of the effective potential V_{KS} acting on the fictitious non-interacting system by minimizing the ground energy functionals of both interacting and non-interacting systems with respect to the same electronic density. The constraint given by the conservation of the total number particles should be preserved during the variational procedure.

$$V_{KS} = V_{ext} + e^2 \int \frac{\rho(\mathbf{r}')}{|\mathbf{r} - \mathbf{r}'|} d\mathbf{r}' + v_{xc},$$

where v_{xc} is given by

$$v_{xc} = \frac{\partial E_{xc}[\rho]}{\partial \rho(r)}.$$

The so-called Kohn-Sham equations can be obtained by minimizing the total energy functional $E^0[\rho]$ with respect to the Kohn-Sham orbitals Φ_i and keeping fixed the total number of electrons:

$$H_{KS}\Phi_i(\mathbf{r}) = \left[-\frac{\hbar^2\nabla^2}{2m} + V_{KS}\right]\Phi_i(\mathbf{r}) = \epsilon_i\Phi_i(\mathbf{r}).$$

Therefore, the many body problem is reduced to the solution of a non-linear set of Schrödinger-like equations, in which the electronic density should be obtained but also is required to build the Kohn-Sham potential. Therefore these equations should be solved self-consistently with an initial guess for the electronic density and therefore V_{KS} until the convergence of both is reached.

Solving the Kohn-Sham equations translates to find the ground state electronic function of the interacting electron system and therefore the ground state energy. The electronic density provides the framework to work in a mean field approach, here the real electronic system was treated as a non-interacting system of electrons feeling a potential V_{KS} which accounts for the many-body effects.

2.2.4 Exchange and correlation energy functional

We can say that the goal of the Kohn-Sham equations is to determine the ground state electronic density and therefore the ground state energy given the exchange and correlation functional $E_{xc}[\rho]$. However no definite shape has been given to this functional. Indeed, no expression for $E_{xc}[\rho]$ is known for systems having more than one electron. In order to model the many-body effects and to put in practice DFT, the $E_{xc}[\rho]$ functional should be approximated. One of these approximations is the Local (Spin) Density approximation L(S)DA. In this approach, the real system is assumed to have locally the same density of an homogeneous electron gas. In this case the $E_{xc}[\rho]$ functional can be expressed as

$$E_{xc}^{LDA}[\rho] = \int \varepsilon^{hom}(\rho(\mathbf{r}))\rho(\mathbf{r}))d\mathbf{r},$$

where $\varepsilon^{hom}(\rho(\mathbf{r}))$ is the local energy density of an homogeneous electron gas. To treat magnetic systems one can express the $E_{xc}[\rho]$ functional in terms of both populations of spins and solving the Kohn-Sham populations for each spin population independently. Here the spins interact via the Hartree interaction and the exchange and correlation potential. The unbalance in the populations of spin is caused by the effect of the $E_{xc}[\rho]$ functional, therefore generating a finite magnetization.

The LDA approximation can describe the electronic, structural and magnetic properties of the ground state for materials like nearly-free-electron metals, ionic solids and intrinsic semiconductors. Though this approximation is made for systems with smooth electronic densities, it also works for systems with which are not perfectly homogeneous like covalent compounds. However it fails in reproducing binding energies and equilibrium bond lengths.

The Generalized Gradient Approximation (GGA) was created as an effort to account for the possible density inhomogeneities found in real systems. In this case, the exchange and correlation functional is also a functional from the local density variations:

$$E_{xc}^{GGA}[n] = \int \epsilon_{xc}^{GGA}(n(\mathbf{r}), |\nabla n(\mathbf{r}))n(\mathbf{r})d\mathbf{r}. \tag{2.48}$$

Though improvements in binding energies and structural properties could be achieved with this approximation, still DFT as implemented in the LDA and GGA approximation is a mean field approach. In order to add the correlations caused by localized charge distributions, corrections should be done to the $E_{xc}[\rho]$ energy functional. In this work we used the Perdew-Burke-Ernzerhof (PBE) exchange and correlation functional, which is in the GGA approximation, to approximate the functional $E_{xc}[n]$.

2.2.5 DFT + U

DFT is unable to describe correctly strongly-correlated materials. This drawback has its origin in the original assumption that the real system behaves like an electron gas. This framework makes either GGA and LDA unable to make correct calculations for materials with localized charge distributions and therefore strong correlations, as evidenced in the incorrect description of transition-metal oxides as metals or small-gap semiconductors.

Correlations are present in systems with highly localized charge distributions, like atoms with partially filled d or f orbitals. For example in the case of hematite, it is well known that the 3d orbitals from the iron atoms are localized in space. It is well known that there is a competition between the kinetic energy (which can be obtained from the bandwidth) and the potential energy that an electron should pay when approaching a region with localized charge. When the kinetic energy dominates, electrons can overcome the Coulomb potential energy originated by charge distributions and delocalize, as it happens in metallic systems. On the other extreme case, when there is a extremely localized state, the price in potential energy an electron has to pay to approach to it is higher than the kinetic energy. Making it difficult for electrons to hop to different sites, which is visible in the narrow bands in the electronic structure, which translates to an insulating behavior.

The natural framework to model correlations can be found in many-body Hamiltonians like the Hubbard Model which in in its simplest form is expressed as:

$$H = -t \sum_{<ij>\sigma} c^{\dagger}_{i\sigma} c_{j\sigma} + U \sum_{i} n_{i\uparrow} n_{j\downarrow}, \tag{2.49}$$

where $c^{\dagger}_{i\sigma} c_{j\sigma}$ is the spin density operator $n_{i\sigma}$ for spin σ on the i-th site and U is the magnitude of the Coulomb repulsion between two electrons with opposite spins located in the same site. In the Hamiltonian the hopping term (which is related to the bandwidth) and the U Coulomb potential energy are the interaction parameters and can be modulated. Therefore corrections to the exchange and correlation functional can be done based on a Hubbard-like mean-field approximation, however the results strongly depend on the values given to the interaction parameters. The main drawback is that there is not a fixed procedure to determine the U parameter, in many cases it is chosen to provide calculations that reproduce experimentally observed band gaps. And another drawback is that Hamiltonians are too simple, that no details in the nature of the electronic structure of the material can be modeled.

2.3 DFT calculation details

We investigated the bending of the energy bands of the hematite (0001) surface using density functional theory (DFT). We performed the calculations in the spin-polarized planewave-pseudopotential formalism using the PBE exchange-correlation functional,[49] as implemented in QUANTUM ESPRESSO.[50] We also considered the DFT+U correction in our calculations to take into account the effects of the localized nature of the $3d$ iron orbitals in hematite.[51,52] We chose the U parameter to be 4.2 eV, which yields a band gap of ~ 2 eV, in agreement with Ref. 53.

We performed the bulk calculations using a 30-atom hexagonal unit cell composed by six formula units of Fe_2O_3. We determined the values of the energy cutoffs and k-point grid we used in our calculations by testing the convergence of the energy differences in spin-paired and spin-polarized bulk hematite. We chose the input values for the calculation until the latter difference in energy converged with a variation of around 10 meV. We selected energy cutoffs of 40 Ry and 480 Ry for the wavefunctions and the charge density, respectively. And we considered a k-point grid of $6 \times 6 \times 2$ for the special-point integration in the Brillouin-zone. We performed a variable-cell relaxation to optimize the lattice constants of the crystals structure, obtaining values of a=5.11 Å and c=13.94 Å . These parameters differ in less than 2% with the experimental values (a = 5.0356 Å and c = 13.7489 Å).[53,54] This structure yielded a band gap of ~ 2 eV and a magnetic moment per iron atom of 4.29 μ_B (experimental value.:[53,55] 4.6 μ_B).

We performed calculations for the stoichiometric FeO_3Fe termination of the (0001) surface of hematite, which has shown to be the most stable in a wide range of oxygen chemical potentials according to ab-initio thermodynamics.[53,56–58] We modeled the surface using slabs with an odd-number of bilayers of hematite (one bilayer corresponds to one formula unit of Fe_2O_3) because it allowed to preserve the mirror symmetry of the antiferromagnetic (AFM) ordering. We used a vacuum of 20 Å between the slabs in the cell to decouple the surfaces and we chose a $6 \times 6 \times 1$ to sample the Brillouin zone, following the grid convergence for the bulk calculations. We computed the surface energy for the 5-bilayered Fe_3O_2 surface to check the consistency of our calculations compared to similar DFT calculations performed in literature. We obtained a value of 62 meV/Å^2 for the surface energy, which agrees with the result reported by Nguyen et al.[53]

Chapter 3

Continuous equations

In this chapter we use the continuous model based on the Stern model and the Poisson-Boltzmann introduced in the previous chapter to show the trends followed by the width of the space charge layer L_{sc} and the potential drop across the interface in dependence of the experimental conditions found in literature. We also show the existence of more experiments displaying ultrathin space charge layers and explore the effects of high doping on the interface. Before discussing this, in the first part of the chapter, we discuss the validity the continuous model under alkaline conditions.

3.1 Validity of continuous equations in alkaline environments

The water splitting experiments reported in literature usually take place at alkaline pH. Therefore it is important to know, whether or not the equations proposed in the last chapter are valid under these conditions. For this purpose, we connected the continuous equations to experimental measurements in Ref. 59. Boily et al.[59] claimed they measured the interfacial potential ψ_0 for the (001) hematite surface as a function of pH and ionic strength (the concentration of each ionic species in the solutions) in $NaNO_3$ solutions.

They measured the spontaneous electromotive force E of a single hematite crystal with respect to a standard reference electrode using a high impedance potentiometer. According to them, the changes of the electromotive force E — as a function of pH, ionic strength, adsorbate concentration, and electrolyte composition — arise from the semiconductor-electrolyte interface. They considered the latter was true if the reference electrode used in the measurements showed a constant potential that does not depend on the composition of the solution. They used the Basic Stern Model (BSM) to describe the electric double layer, which is constituted by the Helmholtz layer or Stern layer and the Gouy-Chapman layer, see Figure 3.1. The plane 0 corresponds to the inner Helmholtz plane and the plane

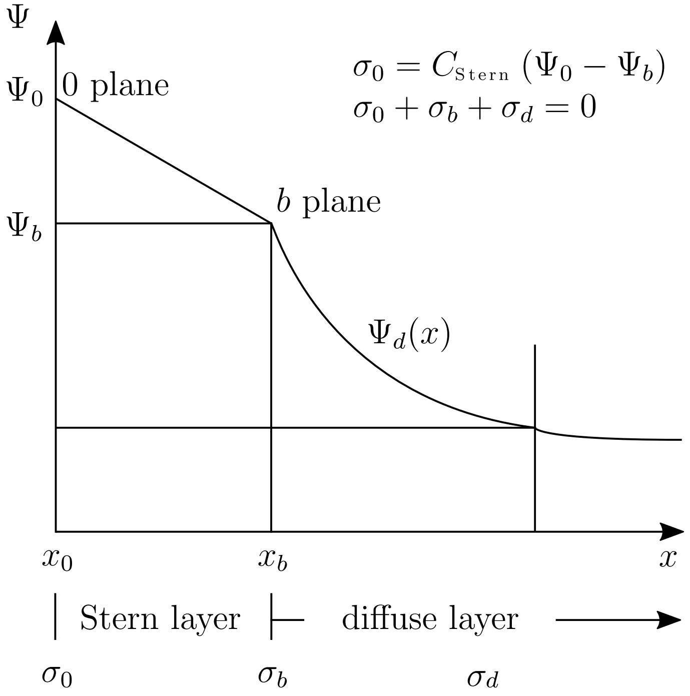

Figure 3.1: Diagram of the Basic Stern Model. The plane x_0 corresponds to the inner Helmholtz plane and the plane x_b marks the end of the Helmholtz layer and the beginning of the diffuse layer. Ψ_0 is the interfacial potential, Ψ_b is the value that the potential takes at the outer Helmholtz plane and Ψ_d is the potential in the diffuse layer. σ_0, σ_b and σ_d are the charges at the inner Helmholtz plane, the outer Helmholtz plane and the diffuse layer. The capacitance in the Stern layer is given by C_{Stern}.

b marks the end of the Helmholtz layer and the beginning of the diffuse layer. Boily et al., related their measured E to the potential Ψ_0 developed in the inner-Helmholtz plane of the hematite-electrolyte interface. At the same time, they also proposed a connection between Ψ_0 and the capacitance of the Stern layer C_{stern} or Helmholtz layer, the surface charge σ_0 and the potential measured at the plane b with respect to the bulk solution, Ψ_b.

$$E = \Psi_0 = \sigma_0/C_{Stern} + \Psi_b. \tag{3.1}$$

From figure 3.1, we can see that the potential drop in the Stern (Helmholtz) ϕ_H layer corresponds to:

$$\phi_H = \Psi_0 - \Psi_b. \tag{3.2}$$

Thus, Ψ_0 can be estimated from the parameters ϕ_H and Ψ_b. Given that Ψ_b is measured with respect to the bulk solution, it corresponds to ϕ_{el} (Equation 2.13). Hence,

$$\Psi_0 = \phi_H + \phi_{el}, \tag{3.3}$$

where ϕ_H is the potential drop in the Helmholtz layer and ϕ_{el} is the potential drop in the diffuse layer, defined respectively in equations 2.12 and 2.13.

We considered the measurements performed in two solutions of $NaNO_3$ with concentrations of 10mM and 500mM. The measured surface potentials E as a function of the pH for the two different solutions are represented by the curves represented by small circles and triangles in Figs. 3.2 and 3.3. The pH in the experiments was modified with the addition of HNO_3 and NaOH, to get more acidic or alkaline conditions respectively. The different geometric figures in the plots represent different titrations or volumetric analysis performed in the same hematite sample to achieve the acidic or alkaline pH conditions. In both cases the solutions had concentrations of 10mM and 500mM at pH 7. The addition of the acid and the base also modified the ionic strength of the solutions, in this case the

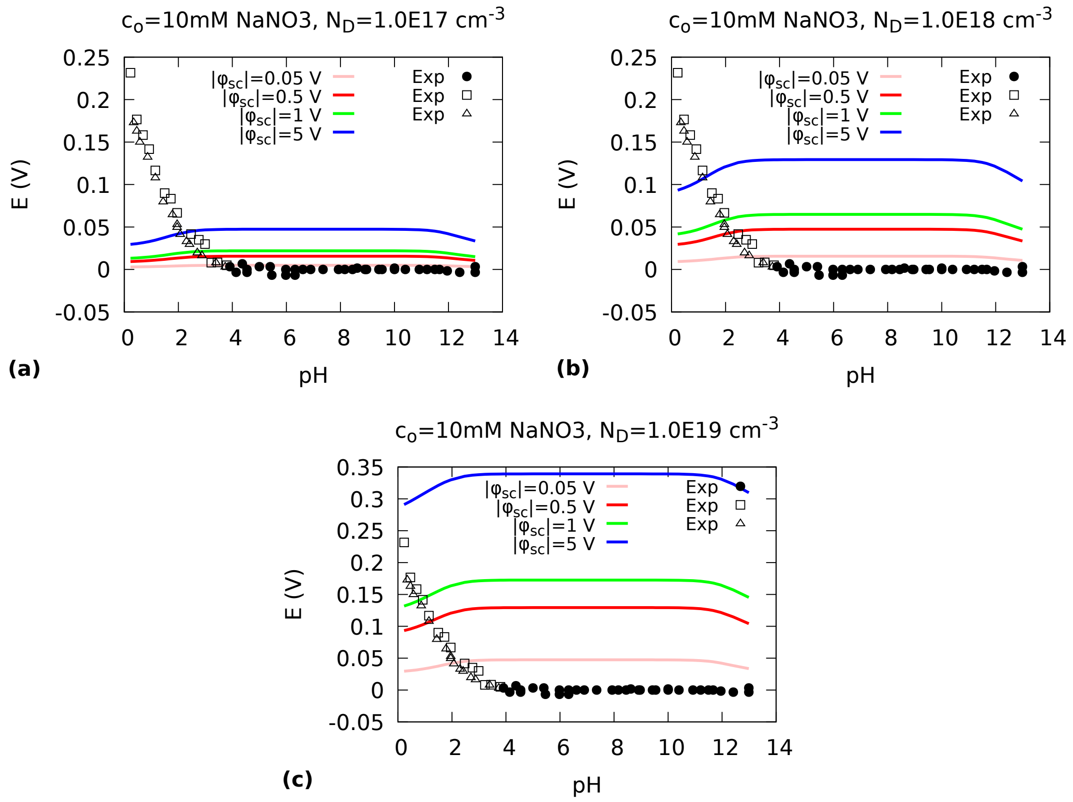

Figure 3.2: Surface potential Ψ_0 as a function of the pH for a solution with initial concentration of 10mM $NaNO_3$ at a pH 7 (neutral conditions). The geometric shapes represent different titrations performed using the same hematite sample. The colored lines show the output of the continuous model proposed in Eq. 3.3 at different potential drops in the space charge layer.

particular concentration of the cations in the solution. In the experiment they used natural hematite crystals exhibiting large smooth faces of (001) orientation.

To recreate the experimental conditions performed by Boily et al.,[59] we set the parameters in the equations describing the potential drop at hematite-electrolyte interface as follows:

- **Donor density**. We set the donor density to be of the order of 10^{18}cm^{-3}, which

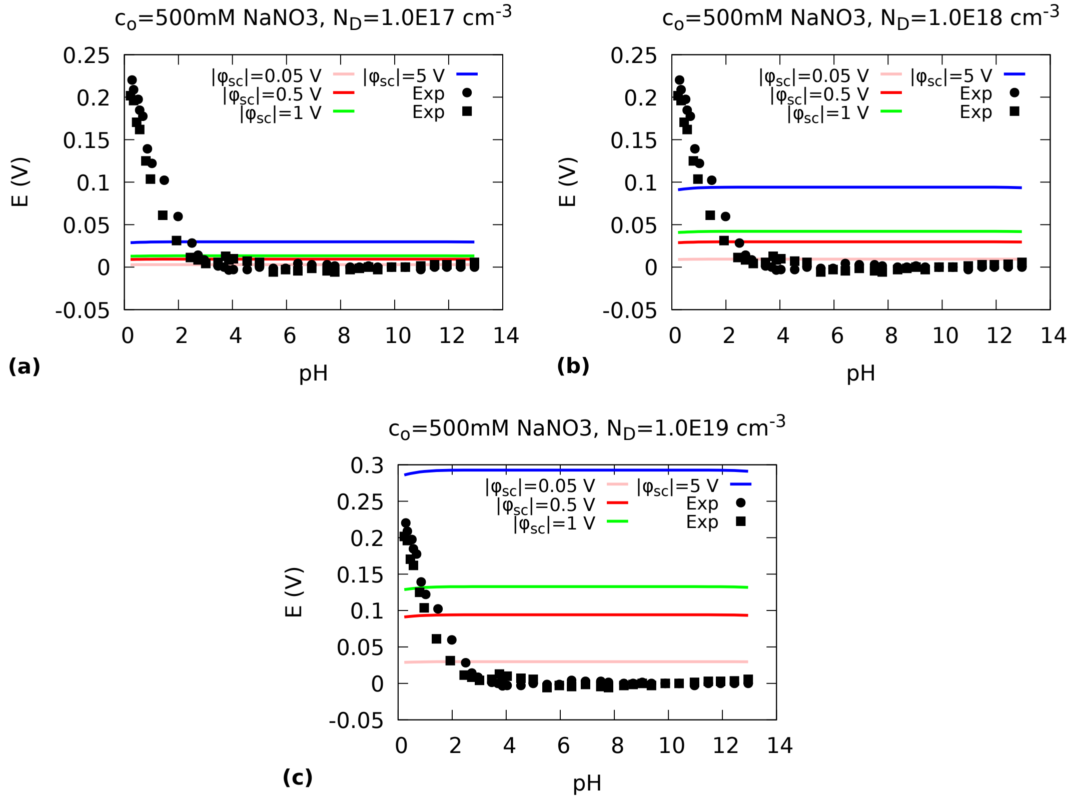

Figure 3.3: Surface potential Ψ_0 as a function of the pH for a solution with initial concentration of 500mM $NaNO_3$ at a pH 7 (neutral conditions). The geometric shapes represent different titrations performed using the same hematite sample. The colored lines show the output of the continuous model proposed in Eq. 3.3 at different potential drops in the space charge layer.

is a value that has been observed experimentally in pure hematite[60].[45] However we also studied the behavior of the equations when the donor density is of the order of $10^{17}cm^{-3}$ and $10^{19}cm^{-3}$.

- **Ionic strength (concentrations).** We used the pH to estimate the ionic strength of the NO_3^{-1} anion in the acidic region, which goes from 0.01/0.5M at pH 7 to 1.01/1.50M at pH 0 (for 10mM $NaNO_3$ and 500mM $NaNO_3$ respectively). We used the same reasoning to calculate the concentration of the ion Na^+ in the alkaline region. Given that $NaNO_3$ is a strong electrolyte, HNO_3 is a strong acid and NaOH is a strong base i.e. they are completely dissociated at any pH; the ionic strengths of the ions were calculated as the sum of the concentrations of the original 0.01M/0.5M solutions plus the concentration of H^+/OH^- donated by the strong acid and strong base.

- **Dielectric constants from the solutions.** Around the neutral-pH region, the concentrations of the electrolyte solutions are dominated by $NaNO_3$ (pH 2-12). We chose the values we used for ϵ_{el} from experimental dielectric constants corresponding to $NaNO_3$ solutions[61].[62] Away from the neutral region, the concentration is dominated either by the HNO_3 or NaOH, in the acidic and alkaline regions respectively. Therefore we considered the experimental values of the dielectric constants of NaOH solutions[38] for the alkaline region. We used the data available for $NaNO_3$ solutions[61] for the acidic region, given that we do not have data for the dielectric constants of HNO_3 solutions. When the concentration of the electrolyte is comparable to the added base or acid, we calculated the dielectric constant of the solution as a weighted average of the components. In most of the cases the dielectric constants at specific concentrations are not found in literature, therefore we estimated them by fitting the existing data to linear equations.

- **Helmholtz layer parameters.** Given that the OH termination is shown to be the dominant termination of hematite in contact with water[63],[10] we used $\epsilon_H = 29.1$ and $L_H = 6.4$ Å that we calculated from the theoretical result for the OH termination obtained by K. Ulman (see section 2.1.2)

The results we obtained for the surface potential Ψ_0 (see equation 3.3) for the 10mM $NaNO_3$ and 500mM $NaNO_3$ solutions, can be seen in Figures 3.2 and 3.3, respectively. The lines in colors represent the results obtained using the equations. The geometric figures represent the experimental data we wanted to reproduce. Since ϕ_H and ϕ_{el} depend both in N_D and $|\phi_{sc}|$, we checked the behavior of the system under different conditions dictated by these parameters.

We recovered the plateau in the experimental curves in Figs. 3.2 and 3.3 at intermediate and alkaline pH values. The ideal (001) hematite surface is expected to remain charge-neutral around the $2-10$ pH range and therefore the flat region should be located at an average zero potential.[59] Using the equations we have for ϕ_{el} and ϕ_H, the plateau is not always close to $\Psi_0 \sim 0$ V. However it is important to point out that the experimental results were shifted by a constant value in order to yield a neutral Ψ_0 in the flat region.[59] According to Figures 3.2 and 3.3, the neutral plateau is reached at low values of ϕ_{sc} at doping densities around $[10^{17}\text{cm}^{-3}, 10^{18}\text{cm}^{-3}]$, which correspond to pure hematite according to experimental literature.[?, 45, 60] The latter might imply that the model is reasonable at alkaline conditions.

To check the validity of the latter results, it is important to analyze whether the parameters introduced in Equation 3.3 are reasonable. Some of these parameters are fixed since they are part of the set up from the experiment and the nature of the sample, like the doping density N_D and the concentration of the solutions c. The remaining parameter to analyze is the potential drop in the space charge layer ϕ_{sc}. Since here we dealt with pure hematite, we should analyze the data at doping densities around $[10^{17}\text{cm}^{-3}, 10^{18}\text{cm}^{-3}]$. We can see in Figures 3.2 and 3.3 that the best fits to the experimental data are obtained at low values of ϕ_{sc}. Since the measurements in this experiment were performed without the presence of any external field, there is no way to increase the potential drop in the semiconductor. Therefore, small values of ϕ_{sc} are physically reasonable. It is important to mention that $|\phi_{sc}|$ is constrained to take values greater than k_BT/e, therefore the lowest value we tested is 0.05V.

At acidic pH conditions we expect to have positively charged (001) surfaces due to the protonation of the predominant $\mu-$OH terminations, according to the experiment. Therefore Ψ_0 should take higher values than the ones found in the plateau. In the experiment the surface potential Ψ_0 is steepest for 500mM $NaNO_3$ than for 10mM $NaNO_3$. Experimentalists attribute this change to the emergence of additional proton-active sites caused by the HNO_3-promoted dissolution of the (001) hematite surface,[59] i.e. the surface becomes more positive. The continuous equations are not able to describe the acidic region given that lack from the description of the adsorption of the protons on the surface. The model is also unable to capture the effect of the dissolution of the (001) on the creation of new proton-active sites. In this analysis we just took into consideration those experimental results in which the surface was not dissolved by addition of the titrant, i.e. fast titrations. According to Boily et al.,[59] the (001) surface showed to be stable during fast titrations due to the slow rate of acidic dissolution of hematite (001). The latter fact was reflected in the reversibility of the protonation of the surface by successive alkalimetric and acidimetric titrations.

Although we were not able to reproduce the data from Boily et al. at acidic conditions, people have been able to reproduce this experimental results using surface complexation models. These models help to take into account the adsorption of potential determining ions by applying a thermodynamic approach to describe the formation of surface complexes. For example, Boily et al.[59] developed a thermodynamic surface complexation model based on the basic stern model to describe their experimental results. In general surface complexation models are used together with models for the electric double layer (Helmholtz and Gouy-Chapman layer).[64] However their implementation generally imply the fitting of equilibrium K constants, capacitances and the surface site density to the experimental data. And in addition, the parameter sets obtained for each fitting have shown to be non-unique. In recent years, people have been working to find a way to develop approaches to estimate the parameters in an internally consistent manner.[64] In order to improve the description we have of the interface, we have to take into account the adsorption of ions (including al the phenomena involved like coordination, bonding, solvation). As well as the atomic structure of the surface given that different surface orientations have different charging behavior.

Summarizing, the model we chose to describe the hematite-electrolyte interface seems to work reasonably well at alkaline conditions. These are the pH conditions we are interested in, given that water splitting experiments are held under these conditions due to the instability of hematite at pH < 3.

3.2 Space charge layer width

The width of the space charge layer is decisive for the efficiency of the photocalalyst in the electrochemical splitting of water: it promotes electron-hole separation and helps to avoid recombination.[60,65] This is possible due the existence of an electric field caused by the depletion of conduction electrons from this region. Figure 3.4 depicts the width of the space charge layer L_{sc} as a function of the doping density for different experiments. The white and the black dots illustrate the values of L_{sc} at which the Oxygen evolution reaction (OER) occurs under illuminated and dark conditions, respectively. The straight lines represent the values that L_{sc} takes in the whole range of applied bias in every experiment. And the inset in Figure 3.4 zooms the data at high doping densities, which is around $\sim 10^{21}$ donors/cm^3.

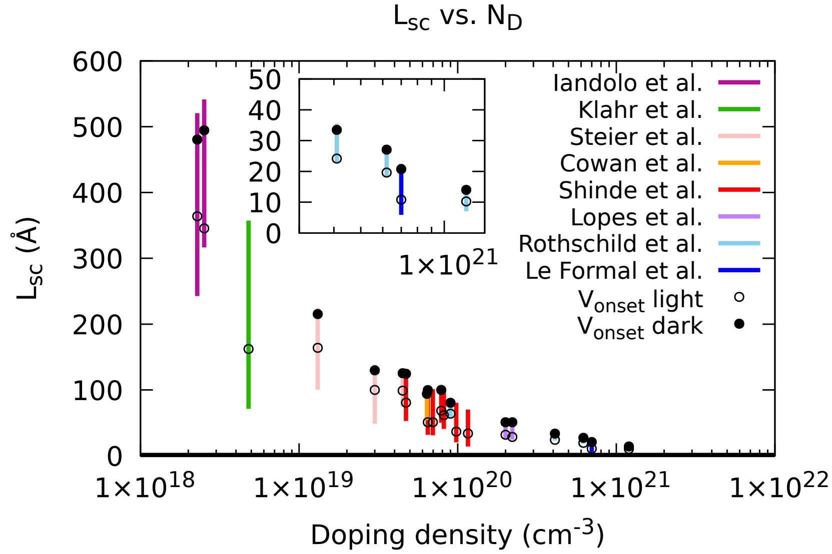

Figure 3.4: Calculated drop of the space charge layer L_{sc} versus the doping density. The inset shows a zoom in on the data at high doping densities $\sim 10^{21}\mathrm{cm}^{-3}$. The white and black dots represent the data of the onset of the OER under illuminated (1 sun) and dark conditions.

We observed that the width of the space charge layer can be as small as 1 nanometer in some experiments, see Figure 3.4. As we mentioned before, Tachikawa et al. recently measured such small space charge layers in highly doped and nanostructured hematite films.[28] We did not report the experiment in Ref. 28 in our work because of the lack of reported parameters needed as an input in the model we are using. We noticed that the hematite samples from the two experiments with the smallest L_{sc} have different microstructures. Le Formal et al.[27] used silicon-doped hematite thin-films with cauliflower-like nanostructures of around 5 nm and Rothschild et al.[66] used Ti-doped thin-films hematite photoanodes with a thickness of 50 nm. In the experiment by Le Formal et al.[27] the space charge layer represents a substantial volume-fraction of the photoanode, which is not true for the other. This difference is evidenced in the remarkably high photocurrent densities and lower onset potential reported in Ref. 27 in contrast to Ref. 66. Though the onset potential in the latter is shifted anodically (is higher) by just 300 mV compared to the onset reported by Le Formal et. al (see Figure 3.11), it still falls in the trends followed by experiments with much larger space charge layers. Rothschild et al.[66] attributed the low photocurrents they observed to bulk effects, based on the effect of H_2O_2 as hole scavenger[67] in the photocurrent densities; and due to surface effects based on the low values obtained for the charge-transfer efficiency coefficient in this sample.

The calculations in this work suggest that the small width of the space charge layer might also play a role in the photocurrent efficiencies. Figure 3.8 shows mean electric fields at the space charge layer as a function of the doping density. The highly-doped samples displayed electric fields in the space charge region, that might be partially compensating the small width of the space charge layer, see Figure 3.8. The volume-fraction occupied by the space charge layer in the photoanode, seems to play a role in the efficiency, as shown by the experiment by Le Formal et al.[27]

The trends observed in the width of the space charge layer L_{sc} under both illuminated and dark conditions occur despite the samples displayed differences in doping densities, doping agents nature, thickness and morphology,[24,25,27,60,66,68–70] see Figure 3.4 and Table 3.1. For example, the films prepared by Shinde et al.[70] were annealed at high and low temperatures and doped with Sn at the surface or by diffusion from the substrate. Clearer

Reference	Dopant type	N_D (cm^{-3})	Film Thickness (Å)	L_{sc} (Å)
Iandolo et al.[24]	Oxygen vacancies	2.28×10^{18}	250 ± 20	242-520
		2.52×10^{18}		316-541
Klahr et al.[25]	Unknown (Possibly Oxygen vacancies)	4.80×10^{18}	600	71-357
Steier et al.[68]	Oxygen vacancies	1.31×10^{19}	190-300	100-224
		3.00×10^{19}		48-138
		4.50×10^{19}		74-129
Cowan et al.[69]	Oxygen vacancies	6.40×10^{19}	Not reported	54-103
Shinde et al.[70]	Sn	4.72×10^{19}	2000 ± 200	53-130
		6.48×10^{19}		32-105
		6.97×10^{19}		31-101
		7.87×10^{19}		50-104
		8.18×10^{19}		40-98
		9.79×10^{19}		20-80
		1.16×10^{20}		14-70
Lopes et al.[60]	Impurities induced by pre-treatment	2.00×10^{20}	247	27-55
		2.21×10^{20}	286	25-52
Rothschild et al.[66]	Ti	9.00×10^{19}	500	59-86
		4.10×10^{20}		23-35
		6.20×10^{20}		18-28
		1.20×10^{21}		7-15
Le Formal et al.[27]	Si	7.00×10^{20}	Not reported	6-22

Table 3.1: Film thicknesses of the samples used in the experiments (reported in the literature) and their corresponding calculated width of the space charge layer L_{sc}. We calculated L_{sc} for the range of applied voltages reported in literature. Every row in L_{sc} correspond to the samples reported by the authors of the experiments. Note that in most of the cases the widths of the space charge layer are smaller than the film thicknesses.

trends were observed in the data obtained from measurements in the dark, where just the electrochemical processes at the interface play a role, see Figure 3.6 (c) and Figure 3.7 (c). The irregularities we observed in the data from measurements under illumination might be linked to bulk phenomena such as exciton formation and photoabsorption.

Thin films with thicknesses of the order of the size of the depletion layer might help to reduce electron-hole recombination according to some authors.[60,71] Lopes et al.[60] observed increased photocurrents at given applied potentials by increasing the film thickness until a critical value, which might be comparable to the size of the space charge layer in the hematite films at the reported doping density. They attributed the lower photocurrents measured in ultra-thin films with moderated doping levels to spatial limitations imposed to the development of the depletion region. They also observed negligible photocurrents in thicker films, presumably because the increase of the electrical resistance in the semiconductor bulk.[60] The calculated widths of the space charge layer are smaller than the reported film thicknesses in most of the cases we examined, except by the films used by Iandolo et al.,[24] see the fourth and and fifth columns in Table 3.1. We would like to point out that frequently the photoelectrodes have non-planar structures, which should lead to a more complicated analysis. In these cases, the local electric field should depend on the curvature of the surface.[72]

We want to point out that the model we used in this thesis for L_{sc}, corresponds to the one extensively used in literature. Experimentalists use it to extract the space charge layer thicknesses in their studies. The validation of the model regarding the prediction of the thicknesses in the nanometric regime is still an open question. However, as part of the motivation of this research, we give the first steps towards understanding this limit. It is not clear how or when this description breaks down. However, the validation could be performed either by experimental or theoretical techniques. Higher resolution experiments are required for the investigation of this interface. On the other and, more robust simulations are required to understand this limit at atomic scales.

3.3 Potential drop at the interface

Figures 3.5, 3.6 and 3.7 show the potential drops across the three regions of the hematite-electrolyte interface and the ratios between them as a function of the doping density. The potential drop in the Helmholtz layer ϕ_H and the potential drop in the semiconductor ϕ_{sc} take comparable values at high doping densities $\sim 10^{21}$ cm^{-3}, see Figure 3.5 (e). This particular condition occurs at the same high-doping regime where the width of the space charge layer reaches ultra-thin dimensions: it is a signature of unexpected working conditions of the photoanode in water splitting experiments. The potential drop in the space charge layer contributes the most to the total potential drop under depletion conditions ($\phi_H/\phi_{sc} \ll 1$),[73] which favor charge separation and hole transport to the surface.[47,48] Many authors claim that this is the regime where charges are separated more efficiently and therefore where the overall efficiency is the highest. The high concentration of experiments with ratios $\phi_H/\phi_{sc} < 1$ reflect this situation, see Figure 3.5 (a).

We plotted ϕ_{sc}, ϕ_H and ϕ_{el} as a function of the applied voltage for samples at different doping regimes to get an insight of the potential distribution across the interface, see Figure 3.5 (c), (d) and (e). The samples with moderated doping levels show potential distributions commonly associated to depletion conditions, Figure 3.5 (c) and (d). In contrast, the highly doped sample in Figure 3.5 (e) displayed comparable magnitudes of ϕ_{sc} and ϕ_H in the entire range of applied potentials. This regime of high doping concentration has not been explored much in experiments. Figure 3.5 (e) shows that changes in the applied potential might cause substantial ionic and molecular rearrangements in the Helmholtz layer. Comparable values of ϕ_{sc} and ϕ_H imply capacitances C_{sc} and C_H with the same order of magnitude.[73] Le Formal et. al[27] reported capacitances with this behavior in the experiment in Figure 3.5 (e). The potential drop in the diffuse layer contributes the least in the entire range of doping conditions, see Figure 3.5 (b), (c), (d) and (e). It vanishes at high solution concentrations $c_0 >\sim 0.1$ M, as it can be seen analyzing Eq. 2.13 in the limit of large c_0.[12,13] Most of the experiments we selected use 1M NaOH electrolytes, except by Iandolo et al.[24] and Klahr et al.[25] who used 0.1M NaOH solutions.

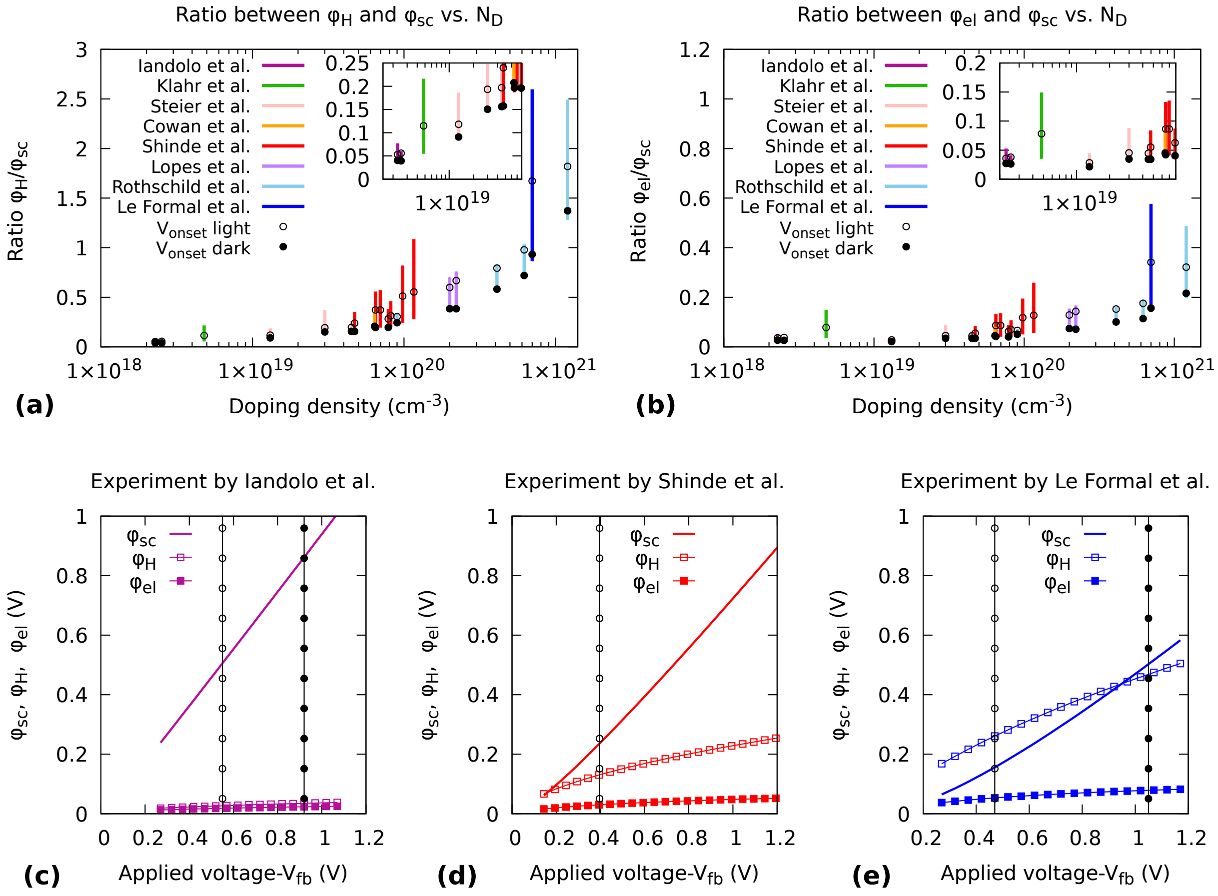

Figure 3.5: Behaviour of the potential drops across the interface of hematite. Figures (a) and (b) show plots of the ratios ϕ_H/ϕ_{sc} and ϕ_{el}/ϕ_{sc} versus the doping density. Figures (c), (d) and (e) show ϕ_{sc}, ϕ_H and ϕ_{el} versus the applied voltage with respect to the flatband potential for three different samples located in different regions of (a). The doping densities of the samples in these experiments were $2.28 \times 10^{18}\text{cm}^{-3}$, $1.1594 \times 10^{20}\text{cm}^{-3}$ and $7 \times 10^{20}\text{cm}^{-3}$ respectively. The vertical lines in (c), (d) and (e) represent the potential values for the onset of the oxygen evolution reaction on both dark and illuminated conditions. The zero of the applied voltage is referenced to the flat band potential V_{fb}. Voltages higher than zero mean applied voltages more positive than V_{fb}.

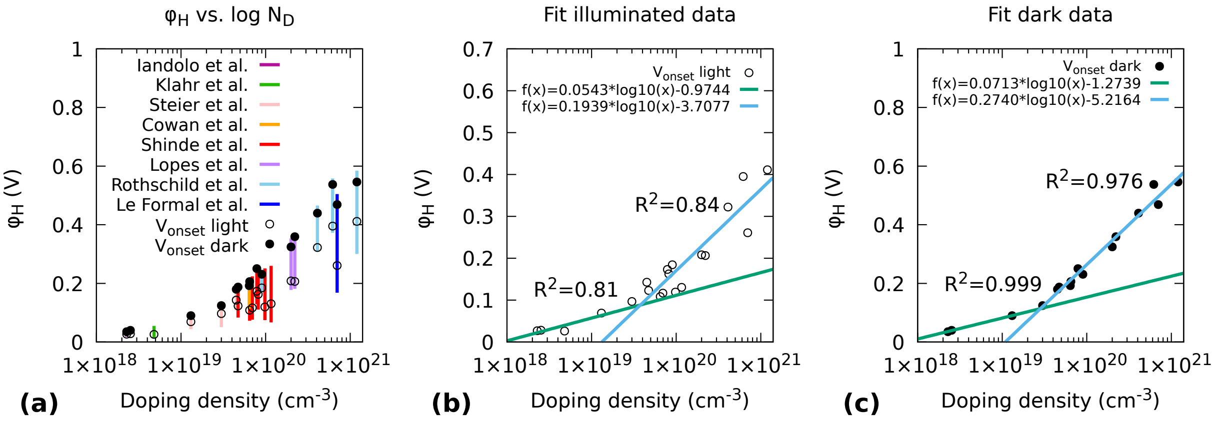

Figure 3.6: Potential drop in the Helmholtz layer versus the doping density, (a). Figures (b) and (c) show linear fits performed for the data of onset potential under illuminated and dark conditions respectively. Here, $\epsilon = 57$ has been used for bulk hematite, together with the Helmholtz parameters extracted from the simulations of the stoichiometric termination.

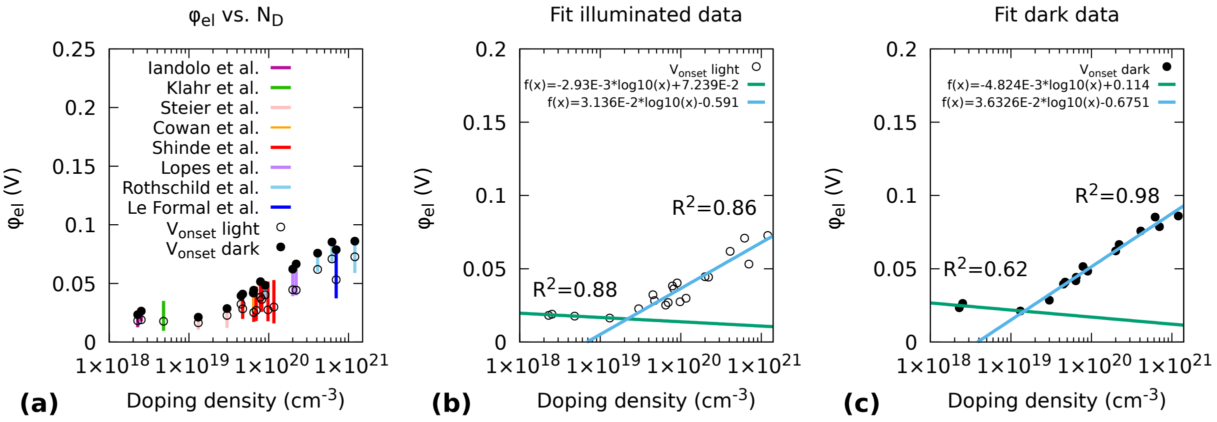

Figure 3.7: Potential drop in the Gouy-Chapman layer versus the doping density, (a). Figures (b) and (c) show linear fits performed for the data of onset potential under illuminated and dark conditions respectively. Here, $\epsilon = 57$ has been used for bulk hematite, together with the L$_H$ extracted from the simulations of the stoichiometric termination.

Figures 3.6 and 3.7 show plots of the potential drop in the Helmholtz layer ϕ_H and the Gouy-Chapman layer ϕ_{el}, both as a function of the doping densities, for all the experiments.

Both potential drops show more dispersed behavior for experiments under illuminated conditions in comparison to the experiments under dark conditions. To get a quantitative insight into these trends, we performed linear fits of the trends followed by the potential drops under illuminated and dark conditions, see (b) and (c) from both Figs. 3.6 and 3.7. The fits were performed in two different regimes: Low (green line) and high (light blue line) doping conditions. We found high correlation coefficients for the both drops (ϕ_H and ϕ_{el}) in the high doping regime, see 3.6 (b)(c) and 3.7 (b)(c). Under these conditions ϕ_H takes values between 0.1 V and 0.6 V. The latter might be a quantitative signature of the regime in which the contribution of ϕ_H becomes important.

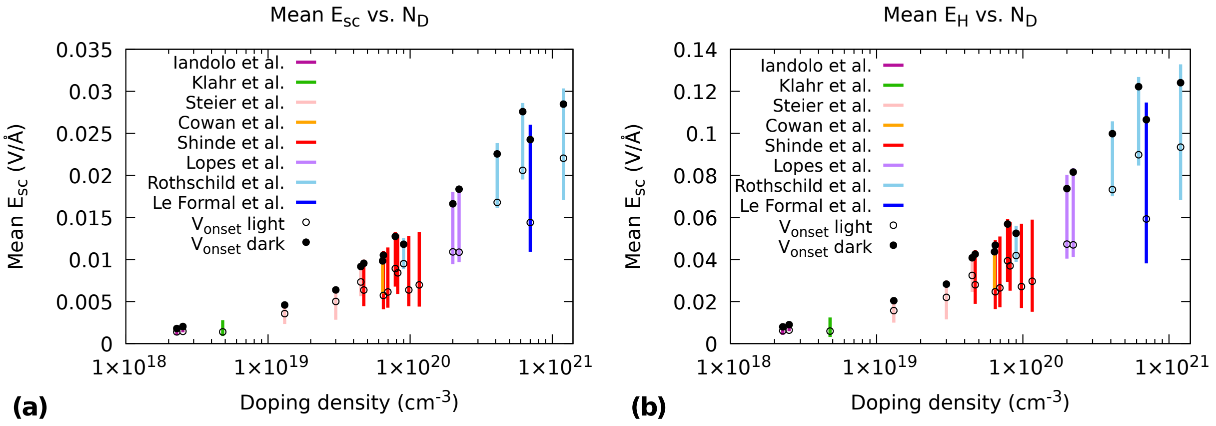

Figure 3.8: Average electric field versus the doping density across the the space charge layer and the Helmholtz layer, figures (a) and (b) respectively. Both average fields increase while increasing the doping density due to the decrease of the spatial extension of both layers.

Figure 3.8 shows the mean electric field in the (a) space charge layer and the Helmholtz layer (b). We computed the first using the calculated L_{sc} (Figure 3.4, Eq. 2.11) and ϕ_{sc} (Figure 3.9), which we obtained by the numerical solution of the system of equations Eq. 2.35, Eq. 2.12 and 2.13. We computed the latter using the ϕ_H (Figure 3.6) and L_H we chose. We can see that in both cases the intensities of the fields in these layers are remarkably high at high doping densities. Which as we mentioned before, might be the compensating factor that enhances charge transfer in ultra-thin space charge layers.

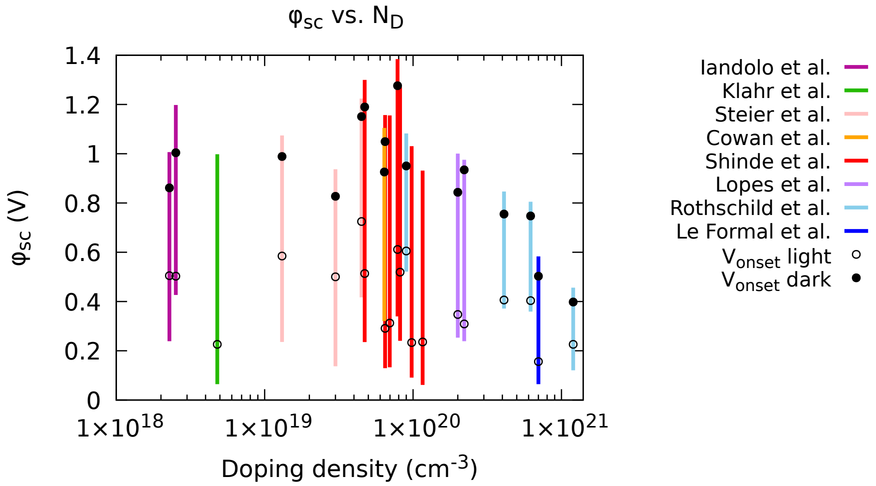

Figure 3.9: Potential drop in the space charge layer versus doping density. Here, $\epsilon = 57$ has been used for bulk hematite, together with the Helmholtz parameters extracted from the simulations of the stoichiometric termination.

3.4 High-doping correction to the Mott-Schottky equation

The Mott-Schottky analysis allows to study the space charge layer and to characterize it using data provided by experiments. The fundamental equation used in this analysis, describes a linear relation between the potential drop in the space charge layer ϕ_{sc} and the square of the inverse capacitance:

$$\frac{1}{C_{sc}^2} = \frac{2}{e\epsilon_{sc}\epsilon_0 N_D}\left[\phi_{sc} - \frac{k_B T}{e}\right]. \tag{3.4}$$

For moderately high-doped semiconductors, most of the total potential drop is accommodated by the space charge layer. This leads to:[34,47,48,74]

$$\frac{1}{C_{sc}^2} = \frac{2}{e\epsilon_{sc}\epsilon_0 N_D}\left[(V_{app} - V_{fb}) - \frac{k_B T}{e}\right], \tag{3.5}$$

where V$_{app}$−V$_{fb}$ = ϕ_{sc}. However this may be inadequate in the case of extreme high-doping densities, which are under study here. As we discussed before, in this regime the contribution of the potential drop of the Helmholtz layer to the total drop across the interface is substantial.

In this section we provide a derivation of the modified version of the Mott-Schottky equation in the case where the potential drop in the Helmholtz layer cannot be neglected. Considering the relation between V_{app} and the contributions to the potential drop ϕ_{sc}, $V_{app} - V_{fb} = \phi_{total} = |\phi_{sc}| + \phi_H + \phi_{el}$; the expression for ϕ_H in equation 2.12 and neglecting ϕ_{el}; we obtained:

$$V_{app} - V_{fb} = \phi_{sc} + A\sqrt{\phi_{sc}}, \tag{3.6}$$

where

$$A = \frac{L_H\sqrt{2}}{\epsilon_H\epsilon_0}\sqrt{e\epsilon_{sc}\epsilon_0 N_D}. \tag{3.7}$$

The latter equation is quadratic in $\sqrt{\phi_{sc}}$, and its solutions are:

$$\sqrt{\phi_{sc}} = -\frac{A}{2} \pm \frac{\sqrt{A^2 + 4(V_{app} - V_{fb})}}{2}. \tag{3.8}$$

Imposing the flatband condition ($\phi_{sc} = 0$ at $V_{app} = V_{fb}$), the only possible solution is the positive '+'. Squaring both sides in Eq. 3.8, we obtained

$$\phi_{sc} = \frac{A^2}{2} + (V_{app} - V_{fb}) - \frac{A^2}{2}\sqrt{1 + \frac{4(V_{app} - V_{fb})}{A^2}}, \tag{3.9}$$

which inserted in Eq. 3.4 leads to:

$$\frac{1}{C_{sc}^2} = \frac{2}{e\epsilon_{sc}\epsilon_0 N_D}\left[\frac{A^2}{2} + (V_{app} - V_{fb}) - \frac{A}{2}\sqrt{A^2 + 4(V_{app} - V_{fb})} - \frac{k_B T}{e}\right]. \tag{3.10}$$

This equation generalizes the Mott-Schottky relation and it is applicable when ϕ_H

cannot be neglected i.e. high doping conditions. Under these conditions the behaviour **changes** close to the flatband potential. In the vicinity of the flatband potential V_{fb}, (V_{app}−V_{fb}) $\ll$ A^2. Thus one can develop a Taylor expansion of the square root in Eq. 3.9

$$\sqrt{(1+x)} = 1 + \frac{1}{2}x - \frac{1}{8}x^2 + ... \tag{3.11}$$

The Taylor expansion to second order leads to the cancellation of the low-order terms and gives:

$$\phi_{sc} = \frac{(V_{app} - V_{fb})^2}{A^2}. \tag{3.12}$$

Inserting this equation in the Mott-Schottky relation in Eq. 3.4, we obtained:

$$\frac{1}{C_{sc}^2} = \frac{2}{e\epsilon_{sc}\epsilon_0 N_D}\left[\frac{(V_{app} - V_{fb})^2}{A^2} - \frac{k_B T}{e}\right]. \tag{3.13}$$

The leading term has changed, therefore close to the flatband potential the Mott-Schottky relation should become quadratic in V_{app}, see Figure 3.10 (a).

On the other hand, if A is small enough under conditions far from the flatband potential, the following relation may apply $A^2 \ll V_{app}-V_{fb}$. We expanded the general expression for the modified Mott-Schottky relation (Eq. 3.10) to first order in A:

$$\frac{1}{C_{sc}^2} = \frac{2}{e\epsilon_{sc}\epsilon_0 N_D}\left[(V_{app} - V_{fb}) - A\sqrt{V_{app} - V_{fb}} - \frac{k_B T}{e}\right]. \tag{3.14}$$

Thus Eq. 3.14 shows that a square root term should correct the linear dependence of the inverse square capacitance on V_{app}−V_{fb}, see Figure 3.10 (b). In principle, this behavior could be detected in highly doped samples, which would indicate a deviation from the classical semiconducting electrode. It is important to mention that the quadratic behavior in the vicinity of the flatband potential and the sub-linear behavior far from it are observed

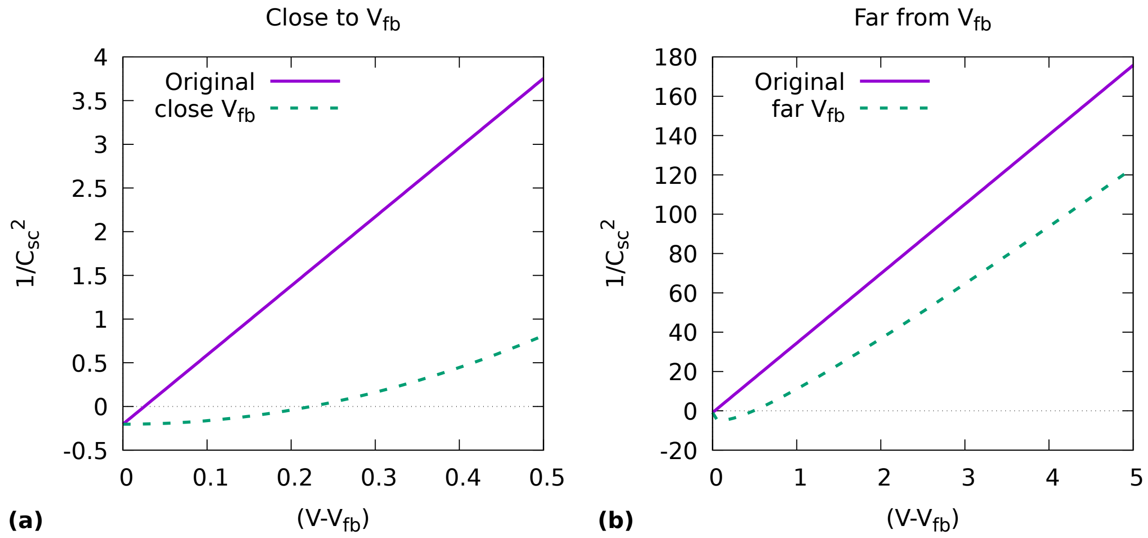

Figure 3.10: Behavior of the general Mott-Schottky $1/C_{sc}^2$ at high doping conditions in two limits: (a) close to the flatband potential where (V$_{app}-$V$_{fb}$) $\ll$ A^2 holds and (b) far from the flatband potential where A^2 $\ll$ V$_{app}-$V$_{fb}$ applies. The green dashed lines represent the curves generated in the two limiting cases, using Eq. 3.13 and Eq. 3.14 for (a) and (b), respectively. The purple lines represent the behavior of the usual linear Mott-Schottky analysis generated with the same parameters used in the high-doping correction.

frequently in the experimental data.[34,47,48,75] However other effects may be playing a role in the experiments. The present equations can be tested in precise experiments to check whether they describe the high-doping regime. We derived expressions for the width of the space charge layer L_{sc} in the high-doping regime, based on the capacitances obtained before. This can be done as equation 2.11 is obtained in the literature.[13] In the general expression for the high-doping regime, L_{sc} can be expressed as:

$$\begin{aligned} L_{sc2} = \quad & \sqrt{\frac{2\epsilon_{sc}\epsilon_0}{eN_D}}[\frac{A^2}{2} + (V_{app} - V_{fb}) \qquad (3.15) \\ & -\frac{A}{2}\sqrt{A^2 + 4(V_{app} - V_{fb})} - \frac{k_B T}{e}]^{\frac{1}{2}}. \qquad (3.16) \end{aligned}$$

And near the flatband potential, it is given by

$$L_{sc3} = \sqrt{\frac{2\epsilon_{sc}\epsilon_0}{eN_D}} \left[\frac{(V_{app} - V_{fb})^2}{A^2} - \frac{k_B T}{e} \right]^{\frac{1}{2}} . \tag{3.17}$$

3.5 Behavior at dark and illuminated conditions

The onset potentials in the dark and under illumination as a function of the doping density are depicted in Figure 3.11. The onset potential in the dark is quite constant despite the differences in doping density, the nature of the dopant and the width of the space charge layer. On the other hand, the onset potential under illumination varies over a broader range of applied voltages. It is remarkable that the values V_{onset} in the dark are weakly affected, given the variety of space charge layer widths and applied potentials we considered in our calculations. From this behavior, we infer that in the dark the overpotential-determining phenomena are independent from the width of the space charge layer L_{sc} and the band bending ϕ_{sc}. This indicates that the surface reactions at the immediate surface of hematite limit largely the OER. Not even large changes in oxygen vacancy concentration performed in experiments affected the J-V curves much.[68]

The onset potential under illumination showed to be more sensitive to many parameters: pH, light intensity and morphology of the samples. Some authors suggest that doping improves slightly the V_{onset}, as it is shown by the scattered data in Figure 3.11. The lowest V_{onset}, we found in literature, correspond to Sn-doped films annealed at 800°C.[70] Similar values for V_{onset} were reported for hematite films annealed at the same temperature, but with different morphologies and microstructures.[7,26,76] The deposition of overlayers on hematite and the use of catalysts also allowed to shift V_{onset} cathodically[27,68,69,77] (by shifting cathodically we mean to shift V_{onset} in a negative direction). A strong correlation between V_{onset} and surface states has been extensively reported in literature.[25,27,68,70]

Some authors suggest that surface states act as electron-hole recombination centers at the hematite surface,[25] which has driven much effort to passivate them.[26,78] However they might play as well a second role as mediators of the hole transfer at the OER under illuminated conditions, instead of the valence band.[25] In fact, some authors claim they

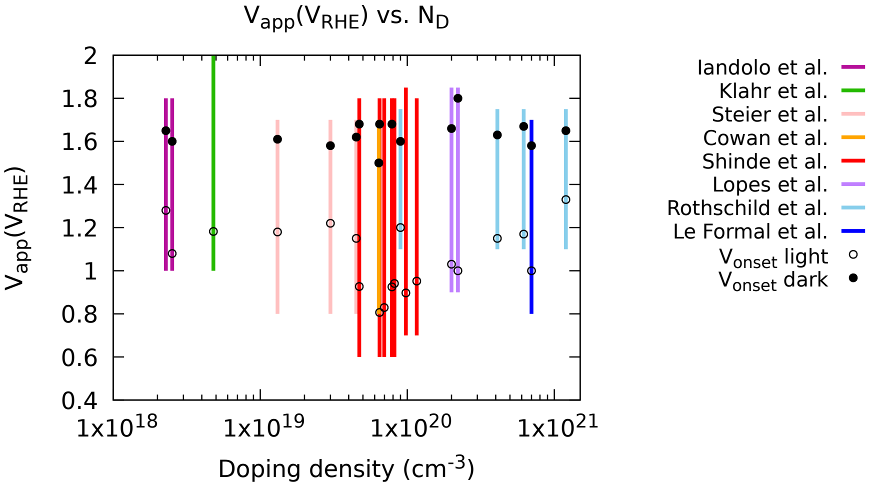

Figure 3.11: Applied potential reported in experiments vs V_{RHE} as a function of the doping density. The black and white dots correspond to the onset potential of the oxygen evolution reaction.

were able to identify these two varieties of surface states in thin hematite films annealed at 500°C and 800°C,[26] by means of cyclic voltametry measurements. They passivated the problematic surface states by annealing the hematite films at 800°C, and they claim that the remaining ones correspond to mediators of the OER.[26] The deleterious surface states are supposed to affect the electron-hole separation because they restrict the band bending.[26] The latter happens because they possess energies below the flatband potential and pin the Fermi level.[26] The remaining "good" surface states at high temperatures can explain the high surface state capacitances measured by Shinde et al.[70] who used samples annealed at 800° C.

Chapter 4

DFT calculations in undoped hematite slabs

We showed in the previous chapter that the space charge layer in hematite can reach widths smaller than 1 nanometer at high but realistic doping concentrations. Recently, these thin space charge layers have been detected in highly doped and nanostructured hematite samples.[28] This regime also seems to be connected to high photocurrents in photoelectrochemical water splitting experiments.[27,28] Space charge layers of such a small size are accessible to direct simulation by ab-initio methods.

In this chapter we show a series of calculations for hematite slabs, based on density functional theory. We analyzed how the band bending develops as we add, one by one, elements of the interface to the models. The atomistic models we used to study the space charge layer in undoped systems are depicted in Figure 4.1. First we started with the stoichiometric termination of the (0001) α-hematite surface (Fig. 4.1 (a)), which is the most stable termination of this material in a wide range of oxygen potentials according to ab-initio thermodynamics;[53,56] then we added one hydroxyl group on each side of the slabs(Fig. 4.1 (b)), while keeping the neutrality of the surface; we also added two additional electrons to the latter (Fig. 4.1 (c)) in order to charge the OH groups. We will show in the next chapter the results obtained by doping the slabs with Ti by substitution of Fe atoms.

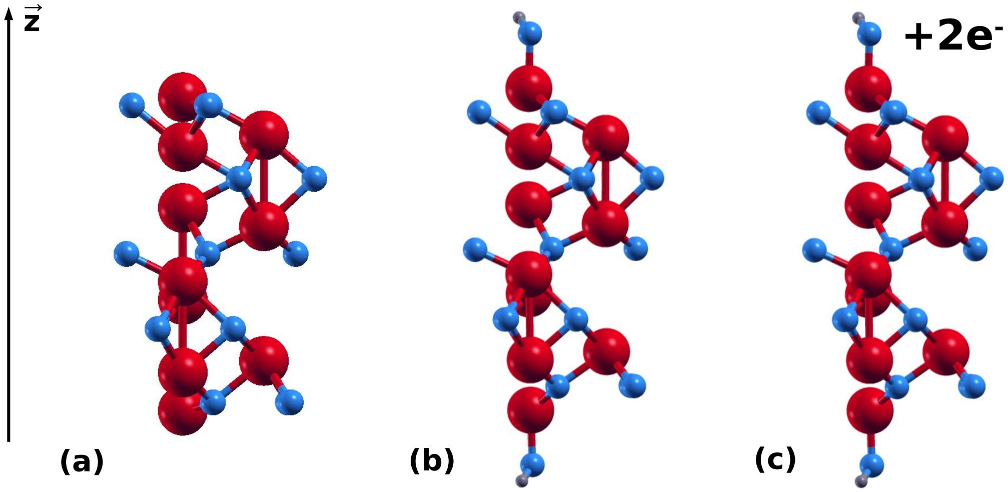

Figure 4.1: Atomistic models used to study the space charge layer in undoped systems. The slab in (a) corresponds to the stoichiometric termination of the (0001) α-hematite surface, (b) corresponds to the latter slab with one additional hydroxyl group on each side (keeping the neutrality of the surface) and (c) illustrates the addition of two extra electrons to the slab in (b). In this case, the slabs consist of 5-bilayers of Fe_2O_3

Here, we focused on the development of the band bending in the semiconductor. We disregarded completely any description of the liquid part of the electrochemical interface in the simulations. The description of the electrolyte implies the addition of ions and water molecules: i.e. the formation of a double layer of charges on both sides of the interface. As a consequence, extra electrostatic terms might arise from the liquid region. In the case of the simulations with adsorbed OH groups, the electrostatic potentials generated by these species (which decay as 1/r) might screen the potential arising from the liquid. It is important to keep in mind that the description of the full interface is out of reach for anyone at the moment. For example, Ulman et al.[32] used a minimalistic model for the solid region to get a more detailed description of the electrolyte (water molecules and ions) using ab initio molecular dynamics (AIMD) calculations. Moreover, it is also impossible to simulate the system under the conditions used in experiments. In this case, electric fields arising from external applied biases should be taken into account. Other important aspect to consider is the liquid nature of the electrolyte. Since this is not an static system, different configurations of the liquid should be sampled. This is already done using AIMD calculations, however it requires orders of magnitude of simulation time.

4.1 Band bending

We reported the local top of the valence band for each oxygen atom layer in the hematite slabs in Figures 4.2, 4.3 and 4.4. We chose the top of the valence band as the energy at which the PDOS of the O-2p states was dropped to 0.001 a.u.; we also reported the energies obtained with thresholds of 0.005, 0.001 and 0.01. We computed the band bending on each

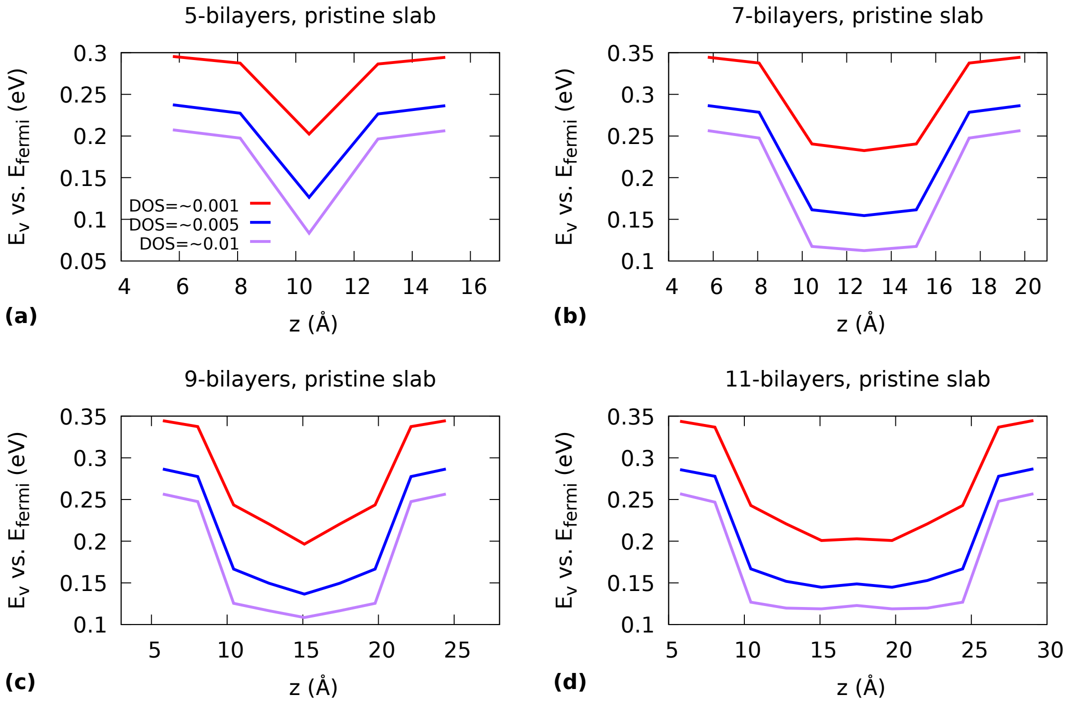

Figure 4.2: Top of the valence band with respect to the Fermi level vs. the positions of the oxygen atoms for the pristine FeO_3Fe slabs with (a) 5-bilayers, (b) 7-bilayers, (c) 9-bilayers and (d) 11-bilayers. The band bending saturation starts to become visible in the 7-bilayered system.

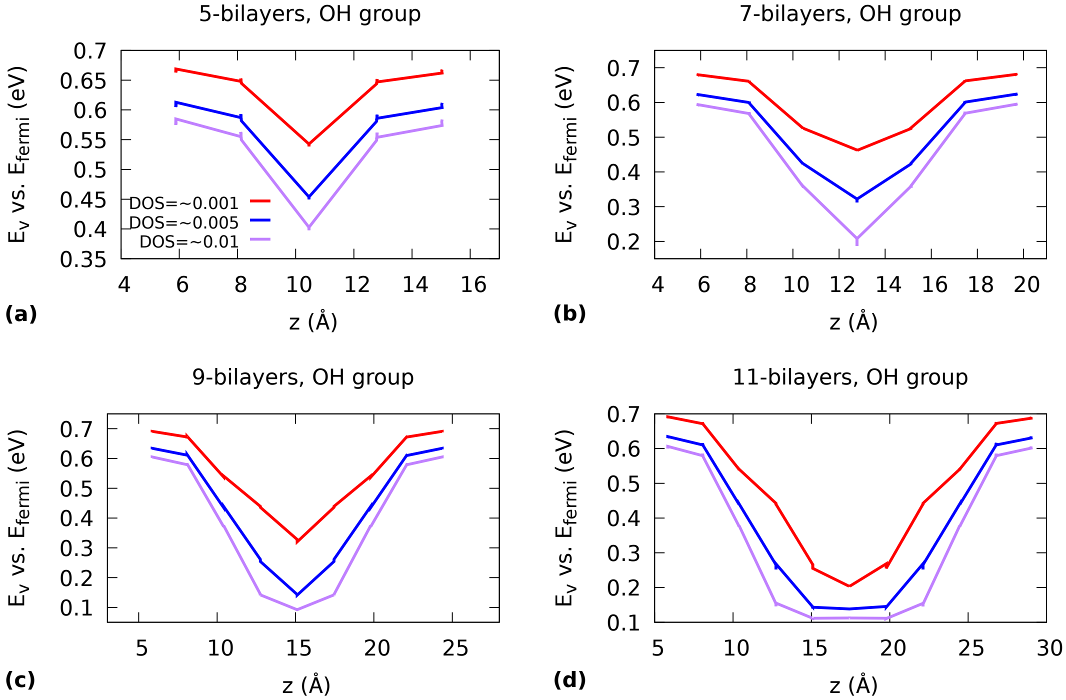

Figure 4.3: Top of the valence band with respect to the Fermi level vs. the positions of the oxygen atoms for adsorbed-OH slabs with a) 5-bilayers, b) 7-bilayers, c) 9-bilayers and d) 11-bilayers. The band bending saturation is visible in the bigger slab.

case, as the difference between the maximum and minimum of each curve in Figures 4.2, 4.3 and 4.4. The band bending is usually introduced as a monotonous function, however its actual description is an open question. In this case it is the difference between the local top of the valence band energy in the center of the slab and at the surface. We want to emphasize that this is not always the case, as we will see in chapter 5.

Figure 4.5 shows the band bending (BB) for the (a) pristine surface, for the surface with (b) adsorbed OH groups and for the surface with (c) adsorbed OH groups and two additional electrons. It is around ~ 0.14 eV for the pristine surface and ~ 0.49 eV for the surface with OH groups. The band bending reached saturation for the pristine and neutral slabs with the adsorbed OH, as suggested in Figure 4.5. In the charged slabs with the OH groups, the band bending reaches a value of ~ 1 eV for the 11-bilayered surface, but

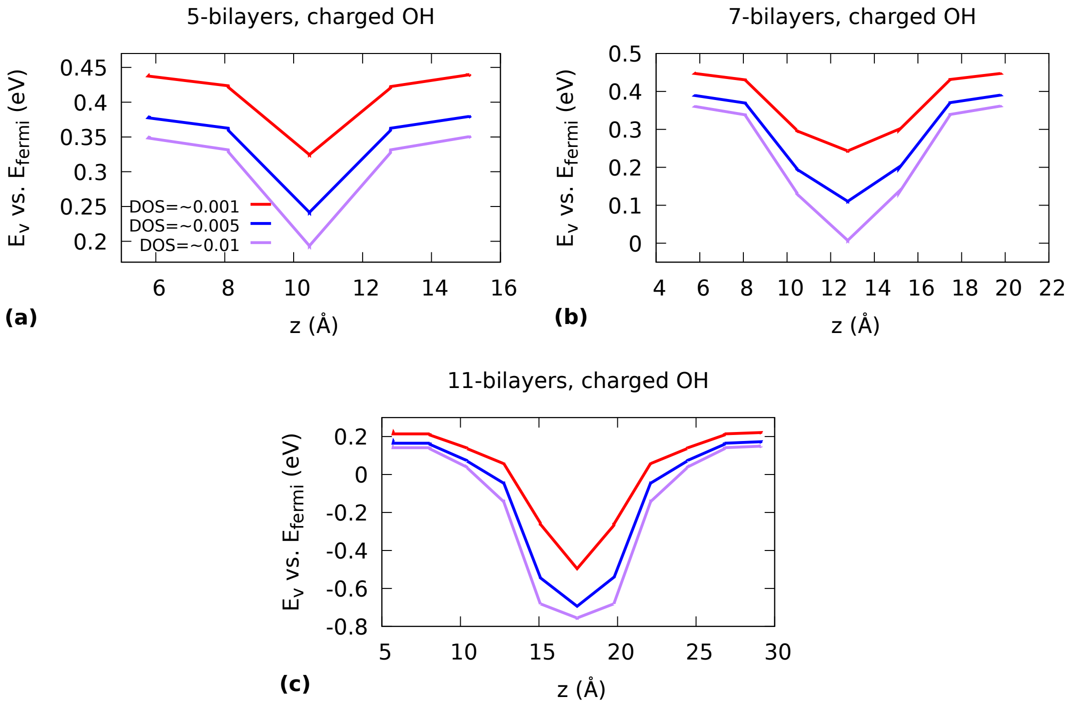

Figure 4.4: Top of the valence band with respect to the Fermi level vs. the positions of the oxygen atoms for OH slabs with two additional electrons made of a) 5-bilayers, b) 7-bilayers and d) 9-bilayers. The band bending saturation saturation has not been achieved even in larger slab.

we did not observed any trace of saturation up to this slab thickness. In general, the band bending strongly depends on the threshold, see Figure 4.5 (a) and (b) for the slabs with small number of bilayers and for all the slab sizes in (c). Despite the choice of threshold is arbitrary, the arbitrariness in the procedure is overcome when the band bending converges with slab thickness. We observed that the band bending is independent of the choice of threshold whenever saturation has been achieved. The bands are basically flat in the center of the slabs, when they are thick enough to show convergence of the band bending with the slab thickness, see Figures 4.2, 4.3 and 4.4. We considered the model is large enough to describe the depletion region when this happens. We observed this behavior in the 7-bilayered slab for the pristine surface and in the 11-bilayered slab with the adsorbed OH groups, see Figures 4.2 (b) and 4.3 (d). The slabs with charged OH groups have not

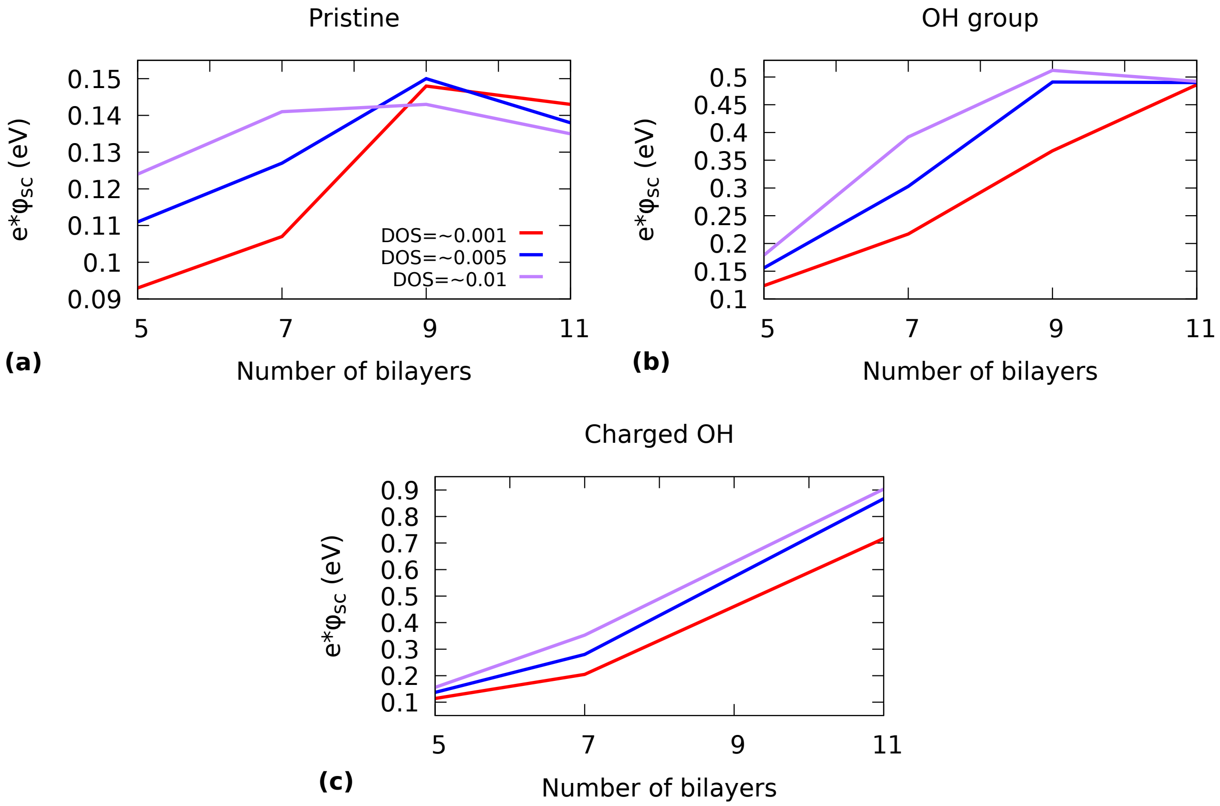

Figure 4.5: The bending of the top of the valence band as a function of the slab size for the (a) pristine surface, for the surface with (b) adsorbed OH groups and for the surface with (c) adsorbed OH groups and two additional electrons. At some points in the graph, small jumps are visible. They are due to atoms with the same z coordinate having slightly different values of the displayed quantities.

developed any flat structure up to the 11-bilayered slab. This might be a signature that more bilayers are needed to reach convergence of of the band bending with the slab size. Clearly, the charged systems are not converged with respect to the slab size and the fact that a compensating charge is needed in the vacuum to keep the charge-neutrality in the system also complicates the calculations. However, the DFT calculations themselves are converged. We added the two extra electrons aiming to charge the OH group on each side of the slabs, as we will see below. Therefore we will use the results of the charged slabs in this chapter, to check the effect of the extra charge on the system.

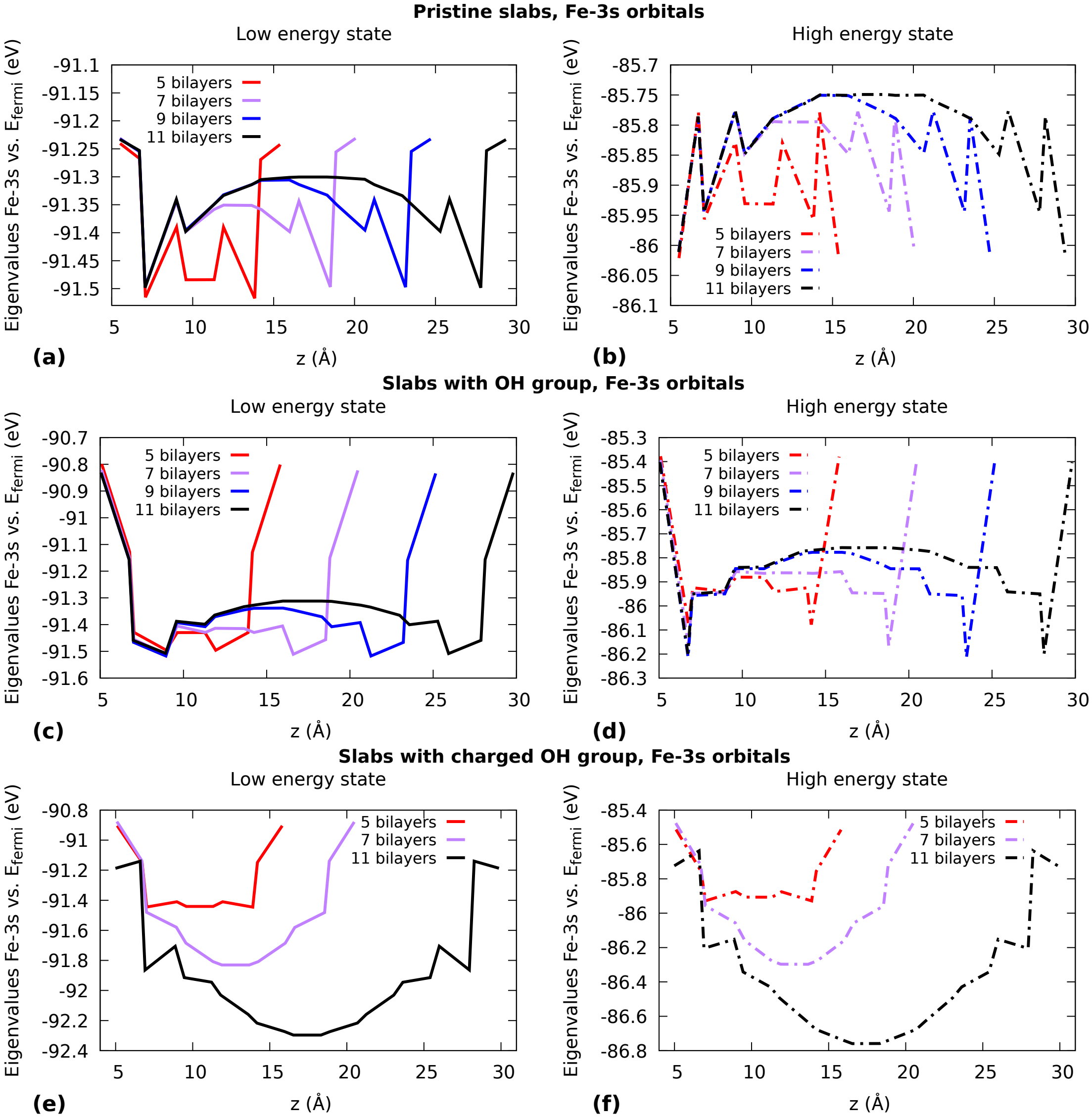

Figure 4.6: Energy of the localized Fe-3s orbitals along the doped slabs with different sizes. Two states with different energy levels were found on each Fe atom for the (a) pristine-doped slab and (b) the slabs with one OH group attached to each side. The low energy state (solid lines) and high energy state (dashed lines) corresponded to two different eigenvalues. The flatness developed on the center of the slabs as the size of the slabs increase, might be a signal of saturation in the case of the uncharged slabs.

We analyzed the behavior of deeper states, namely the Fe-3s states, to confirm the electrostatic nature of the shifts of the bands in proximity of the surface. We extracted the energy from these states using the projections of the wavefunctions into molecular orbitals. We filtered the wavefunctions displaying Fe-3s states with coefficients greater than 0.9, in order to find localized states. We found two different states with different energies for each Fe atom, which due to their localized nature, correspond to different eigenvalues in the band structure. We plotted the two states we found as a function of the position of the Fe atoms in Fig. 4.6 for the (a) (b) pristine slab, (c) (d) the slab with adsorbed OH-groups and (e) (f) the slab with adsorbed OH-groups and two additional charges. The solid lines in figure 4.6 represent the states with lower energy and the dashed lines represent the states with higher energy. In the uncharged slabs, we observed that the energies of the Fe-3s states converge in the center of the slabs as the number of bilayers increases. The latter gives rise to a flat region in the inner part of the slabs, that might indicate convergence of the band bending.

Due to the irregularity of the shapes displayed in Figure 4.6, we calculated the band bending (BB) as the difference between the maximum point and minimum on each plot. The trends followed by the band bending of the Fe-3s states as a function of the slab size can be found in figure 4.7, for the (a) pristine, (b) OH-adsorbed and (c) charged-OH slabs. Figure 4.7 (a) and (b) suggests that the bending of the energy bands from the Fe-3s states has reached saturation in the uncharged cases. Which confirms the convergence of the calculations, as observed using the O-2p orbitals . We also observed in 4.6 (e)(f) and 4.7 (c) that there is no signature of saturation in the case of the charged slabs with adsorbed OH groups, as already seen using the O-2p orbitals. From the latter results, we got a qualitative insight of the electrostatics using the energy of the Fe-3s orbitals. However, we would like to point out that we cannot make a quantitative connection between the results in this section and classical expression for the width of the space charge layer (Eq. 2.11). Neither with the results obtained from the analysis done with the O-2p nor from the one done with the Fe-3s orbitals. The reason for this is that the slabs we analyzed here are undoped, and we did not consider other sources of doping like oxygen vacancies. The band bending developed in these cases is intrinsic to hematite, therefore its origin is

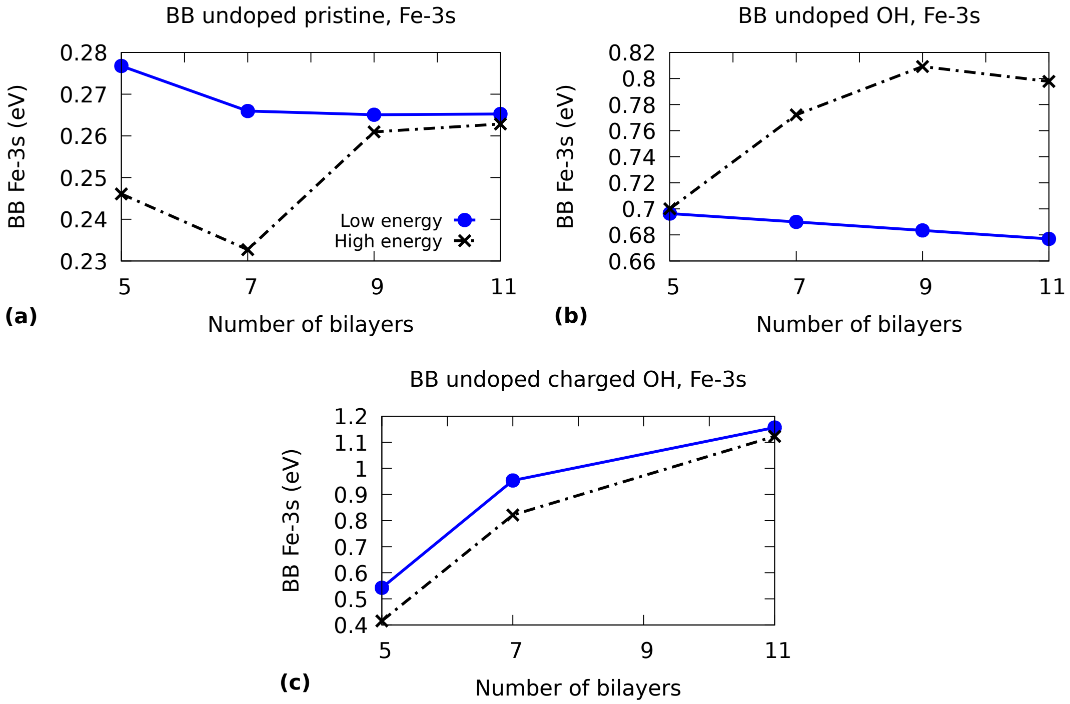

Figure 4.7: Trends in the band bending of the Fe-3s orbitals energy bands as a function of the size. The band bending on each case was computed as the difference between the highest and lowest points in the plots in Fig. 4.6. The band bending of Fe-3s orbitals shows convergence in the case of the uncharged slabs.

purely quantum mechanical. As we will show in the next chapter, we found a connection between the DFT data obtained from the doped systems to the analytical expression in Eq. 2.11.

4.2 Atomic and electronic structure of the space charge layer

As we showed in the previous section, the band bending increased as we added the OH group to the stoichiometric slab and then with the additional charge. The former agrees with chemical intuition because the OH-groups tend to attract negative charge towards

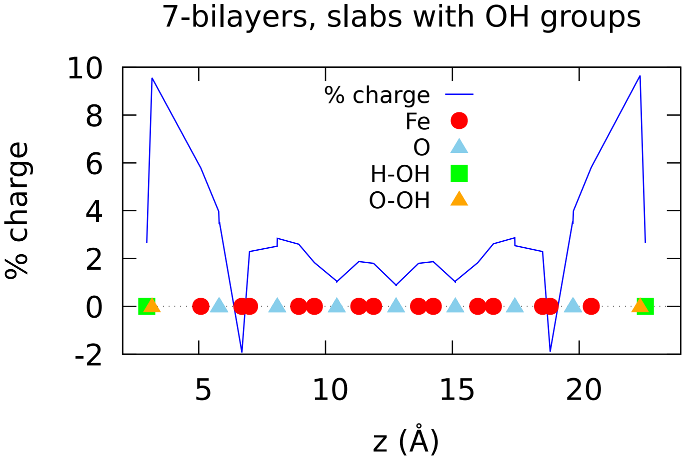

Figure 4.8: Percentage of Löwdin charges transferred to every atom in the slab with OH groups by the addition of two extra electrons. This calculation corresponds to the 7-bilayered slabs with OH termination. The position of the atoms in the slabs are represented by geometrical figures. The red circles correspond to the Fe atoms, the blue triangles to the oxygen atoms in hematite, the green squares to the H atoms from the OH groups and the yellow triangles to the O atoms from the OH groups. It can be seen that the greatest percentage of charge is received by the O atom from the OH group.

the surface. In our model, the surface density of one adsorbed OH group corresponds to 4.4 OH/nm^2. When charges are added to the slab, the accumulated charge at the surface leads to an increase in the band bending. The Löwdin pseudo-atomic charges confirm the trend. The charge of the additional electrons goes mainly to the OH groups, although also atoms inside the slab receive a tiny part of it (Figure 4.8). The additional electrons correspond to a surface charge of 0.7 C/m^2.

The additional charge on the hydroxyl group is also reflected in a clear change of geometric and electronic configuration of the hydroxyl group: in the neutral system, the angle $\angle$Fe-O-H is $\sim$ 120°, which is representative of sp^2 hybridization; in the charged system, this angle changes to 104.7°-107.8°, very similar to the 109.5° of tetrahedral sp^3-hybridized systems, and to 104.5° in water. The geometry of the surface does not change significantly with slab thickness in the neutral system (Tab. 4.1). This fact is useful for

	Relaxed slabs		
	5 bilayers	7 bilayers	11 bilayers
Uncharged-OH slabs			
Fe-O (Å)	1.83	1.83	1.83
O-H (Å)	0.98	0.98	0.98
$\angle$Fe-O-H	119.3°	119.5°	119.9°
Charged-OH slabs			
Fe-O (Å)	1.94	1.93	1.91
O-H (Å)	0.98	0.98	0.98
$\angle$Fe-O-H	104.8°	106.2°	107.2°

Table 4.1: Length of the O-H and Fe-O bonds and the angle $\angle$Fe-O-H for the uncharged-OH slabs and charged-OH slabs.

future calculations, since one can relax a small slab and use the same molecule orientation before relaxing larger systems. On the contrary, in the charged system, Löwdin charges and geometry of the surface continue to change with slab thickness, as a further confirmation that the charged system is not yet converged at the considered thicknesses. In that case, clearly the space charge layer extends beyond the sizes considered here.

The PDOS of the 7-bilayered slabs can be seen in Figure 4.9. The projected density of states (PDOS) of the pristine slabs and the neutral slabs with adsorbed OH groups do not show considerable changes as the number of bilayers in the slab increases. However, this is not the case for the charged slabs, where the gap decreases as the slab thickness increases, see Figure 4.10 (a) and (b). The band gap decreases in the three systems in comparison to the one of bulk hematite. This could be explained because of the emergence of empty states at the top of the valence band, see Figure 4.9 (a), (b) and (c). In the case of the charged slabs (Fig. 4.10 (a) and (b)), the gap also decreases due to the shift of the conduction band towards the gap. The empty states in the valence band from the pristine slab correspond to surfaces states; Ulman et al. identified them in previous DFT calculations and passivated them with Ga_2O_3 overlayers.[78] We also observed the same states in our calculations and we identified analogous surface states in the slabs with adsorbed OH groups (both neutral and charged). In addition to that, we detected surface states in the bottom of the conduction band in the three systems. Some peaks appear in the bandgap upon charge addition in

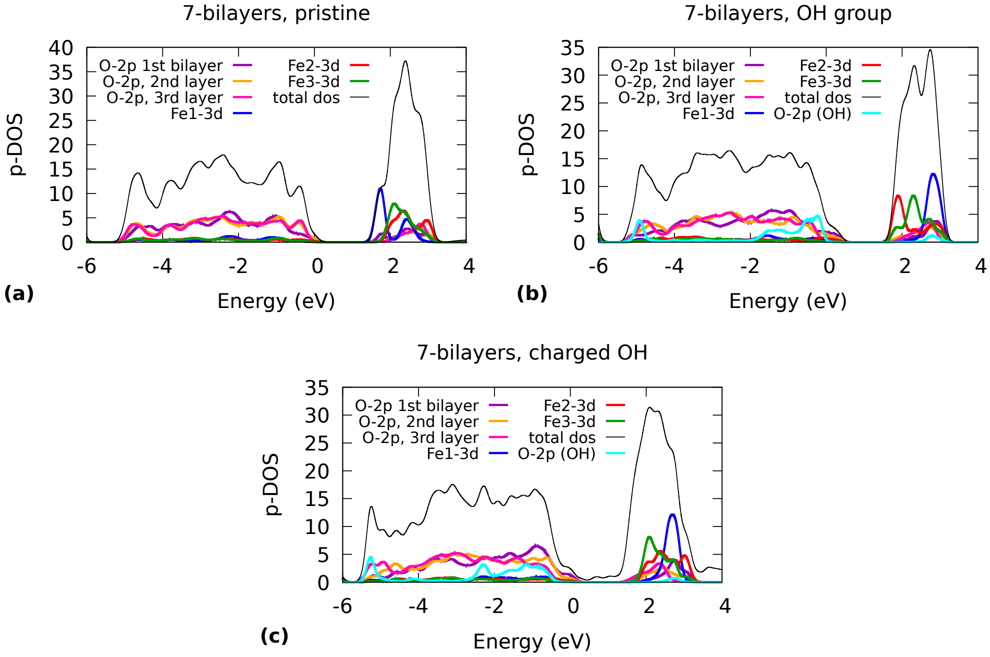

Figure 4.9: Projected density of states of a) pristine, b) uncharged OH and c) charged OH hematite slabs with 7 bilayers. The PDOS plotted for the different orbitals were multiplied by a factor of 1.4 to make them more visible. The density of states is adjusted to correspond to half of the atoms from the same side of the slab.

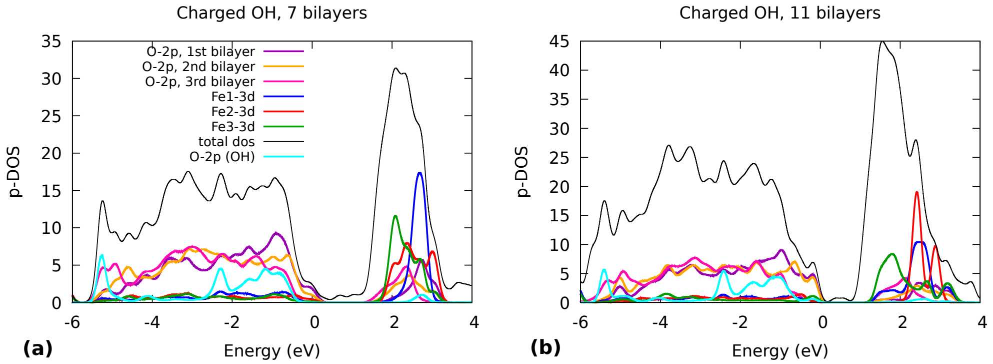

Figure 4.10: Density of states of charged OH hematite slabs. a) 7-bilayered slab and b) 11-bilayered slab. Here we multiplied the pdos for the different orbitals by 2. The total density of states is adjusted to correspond to half of the atoms from the same side of the slab.

the systems with attached OH molecules, see Figure 4.9 (b). These small peaks are mainly due to the s orbitals from the H atoms from the OH group and the 4p states from the top iron atoms. In the charged-OH slabs, the band gap gets reduced as the number of bilayers increases (Figure 4.10).

We plotted the band structure for the three systems in the $\bar{\Gamma}-\bar{M}-\bar{K}-\bar{\Gamma}$ direction, see figure 4.11. The pristine surface has some empty states at the top of the valence band, as shown by the PDOS; and it also presents a dispersive state around the K point, see Figure 4.11 (a). We checked the projections of these states into molecular orbitals and confirmed that these empty states consist on surface states which are delocalized on the surface. These states consist mostly of p-orbitals from the oxygen atoms located in the first two bilayers of the slab and of a small contribution from d-orbitals from the iron atoms from the upper bilayer. When we added the OH groups to the pristine slab, the band that was

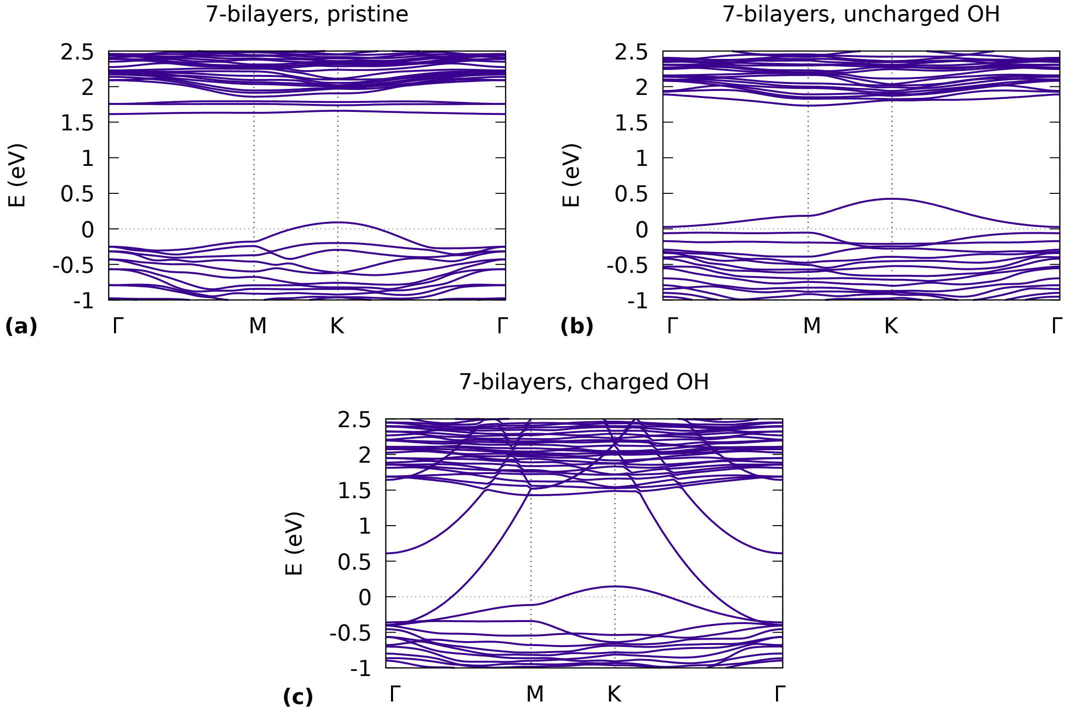

Figure 4.11: Band structure of the 7-bilayered a) pristine, b) uncharged OH and c) charged OH hematite slab.

previously the valence band shifts and becomes completely empty, see Figure 4.11(b). The latter happens because the slab donated electrons to the OH groups. The contribution from Fe-3d orbitals increases in the surface states, though the one from O-2p orbitals is still dominant. Upon addition of electrons, the single band mentioned before goes back to the original situation of having an empty pocket around the point K with surface states composed by superficial O-2p orbitals, see Figure 4.11(c). In addition to this, there is a massive change in the electronic structure in the slab with additional electrons: some bands appear across the band gap and some of these states are even occupied. We found out that these states are delocalized in the vacuum. However this effect cannot be attributed to a realistic physical phenomenon because it is caused by the background of positive charges used by Quantum Espresso to perform the calculations for the charged slab.

Figure 4.12 shows the probability density of some representative states from the valence band and conduction band at the $\bar{K}$ point ($\vec{k} = (1/3, 1/3, 0)$) for the (a) pristine slab, (b) the slab with adsorbed OH groups (c) and the slab with the OH groups and two additional electrons, all in the slabs with 7-bilayers. We depicted the surface states around the top of the valence band with blue lines and the bulk states in the conduction band with golden lines, see Figure 4.12. In order to identify the surface states, we integrated the probability density of the states from 5 Ångstroms of vacuum above the surface to the position of the second Fe atom in the slab and then we normalized it with the complete integral along the slab (including the 5 Ångstrom of vacuum on each side). Then we filtered the states by setting a threshold of 0.5 for the minimum weight the states can have close to the surface, i.e. the states with weights greater than 0.5 were considered surface states. As a further control, we checked the shape of the states to reject surface resonances.

We observed that in the three cases, the nature of the states and their position in the valence and conduction band, reflected the band bending picture. We confirmed that the empty states in top of the valence band indeed correspond to surface states, see V_B SS in figure 4.12. We also noticed that states with bulk character start to appear as one moves away from the valence band, see HOMO and below HOMO in Figure 4.12. We detected bulk states and surface resonances close to the bottom of the conduction band (C_B BS and C_B SR) and we identified surface states at higher energies deep into the band (C_B

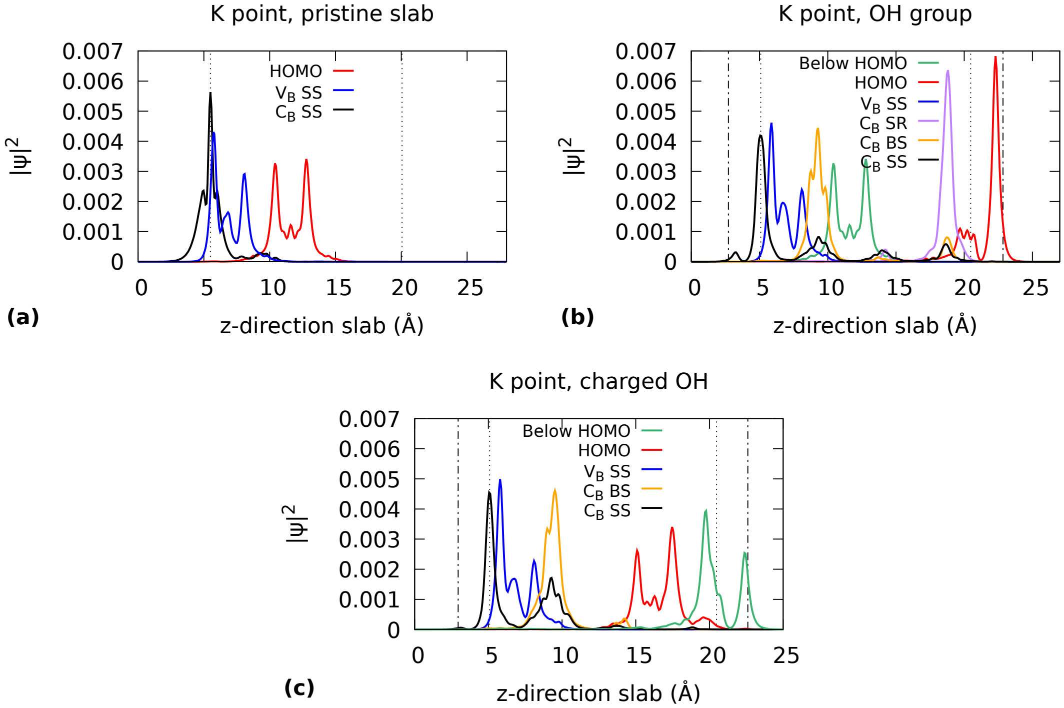

Figure 4.12: Probability density of representative states from the valence and conduction band at the $\bar{K}$ point in the 7-bilayered (a) pristine slab, (b) the slab with adsorbed-OH and (c) adsorbed-OH with two additional electrons at the $\bar{K}$ point. These states are degenerate and therefore have a symmetric counterpart on the other side of the slab. In this case we plotted the spin up states. HOMO represents the highest occupied state in the valence band, we also plotted some states deeper in the valence band and denoted them as Below HOMO. We identified surface states in the top of the valence band V_B SS and a few eV deep into the conduction band C_B SS. The surface resonances and bulk states at/close to the bottom of the conduction band are denoted by C_B SR and C_B BS. The dashed and dotted vertical lines represent the position of the hydrogen atoms and the top iron atoms in the slabs. The weight of the surface states close to the top of the valence band depicted in (a), (b) and (c) are 0.51, 0.54 and 0.57 respectively. The weight of the surface state found in the conduction band C_B SS in the (a) pristine surface is 0.89 and was found at 0.3 eV deep in the conduction band; in (b) the slab with attached OH groups the weight of the C_B SS is 0.6 and it was found at 1.2 eV deep in the conduction band; (c) In the charged-OH slab the weight of the state is 0.94 and it was found at 1.4 eV deep in the conduction band.

SS). Our observations suggest that the deepness of the energies of the surface states in the conduction band might be correlated to the relative band bending shown by the different slabs. In the $\bar{K}$, the surface states in the conduction band C_B SS were found at energies of ~ 0.3 eV, ~ 1.2 eV and ~ 1.4 eV deep in the conduction band in the pristine slab, the neutral slabs with attached OH and the charged slab with the OH group respectively, see Figure 4.12 (a), (b) and (c). We used the orbital projections from the states to track more surface states in the 7-bilayered slabs. We filtered the wavefunctions with atomic states close to the surface that were multiplied by high Fourier coefficients (∼0.7). In table 4.2, we report the depth at which we found these states in the conduction band and the weight of their probability density close to the surface, whenever the data was available.

	7 bilayers		11 bilayers	
	CB depth (eV)	weight	CB depth (eV)	weight
Pristine	0.25	0.92	0.29	0.89
	0.40	−−	0.40	0.93
			0.44	0.94
OH	0.35	0.50	0.39	0.51
Charged OH	0.87	−−	1.50	−−
	1.2	0.60	1.65	−−

Table 4.2: Surface states from the conduction band C_B SS in the three systems we modeled. We report the deepness at which the surface states were found in the conduction band and the weight of the probability density in the vicinity of the surface (up to the position of the second Fe atom). In this table we report the analysis in slabs with 7 bilayers and 11 bilayers. Every row in the table correspond to a surface state e.g., we found three surface states in the pristine slab with 11 bilayers. In this analysis we used the projections from the wavefunction into atomic orbitals to identify the states, therefore we did not have data to compute the weight in all cases: two dashes appear when the latter occurs.

We performed the same analysis in the 11-bilayered slabs to check the robustness of the latter analysis (using slabs not convered with slab thickness), see Table 4.2. In general, we found surface states with the same nature in all cases. The surface states found in the pristine and the adsorbed OH slabs are located practically at the same deepness in the conduction band for both slab sizes, while this is not the case for the charged slabs. The latter might be a consequence of the lack of convergence in this system. However, we find remarkable that in the charged slabs the depth of the states in the conduction band seems to be correlated with the band bending displayed at different slab sizes (the band bending is larger in the 11-bilayered slab than in the 7-bilayered). In the 11-bilayered slabs, we were also able to identify the band bending picture we observed in the smaller 7-bilayered system: we found surface states at the top of the valence band and we found bulk states at the bottom of the conduction band. Therefore, the band bending picture represented by the states plotted in figure 4.12 agree qualitatively with the three different systems in the 11-bilayered case. These calculations provide information on the electronic structure, independently of the lack of convergence of the band bending with slab size. As we observed in the analysis using the system with 11-bilayers, we obtained the same qualitative picture and similar quantitative results as in the smaller slabs, see Table 4.2. This is supported by the fact that the localized states in the surface are clearly constant independently of the slab size. As it was mentioned before, the DFT calculations are converged in all the cases.

4.3 Potential across the slabs and work function

Figure 4.13 shows the planar and macroscopic averages of the potential across the slabs for the 11-bilayered slabs. The addition of the OH group and the subsequent addition of the charges are evidenced in the change of the potential around the surface compared to the potential of the pristine surface, see Figure 4.13 (a), (b) and (c). Apart from changes of the potential close to the surface, the addition of the two electrons also changes significantly the behavior of the potential in the vacuum, which is constant in the neutral slabs but shows variations in the charged case.

We computed the work function W for the three slabs in all the sizes, see Table 4.3. We noticed that the work function converges when the band bending reaches saturation, as it can be seen for the values of the uncharged OH and pristine slabs (Tab. 4.3). The

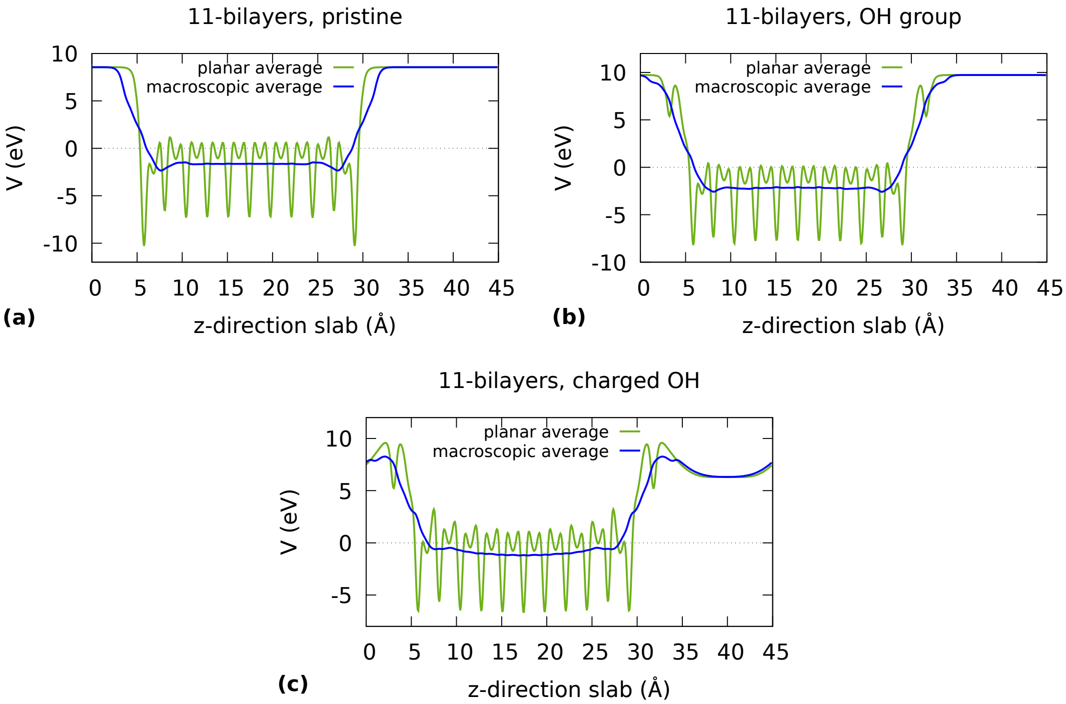

Figure 4.13: Planar and macroscopic averages of the potential across the 11-bilayered hematite slabs. The resulting potential across the pristine slab, the slab with an adsorbed OH molecule (OH Group), and the slab with the OH molecule plus two additional charges (charged OH), can be seen in figure (a), (b) and (c) respectively.

trends in the values of W agree with the physical intuition as the OH groups and the electrons are added to the slabs. When the OH group is added, it attracts electrons to the surface and lowers their energy in the solid. All this makes more difficult to extract electrons from the surface and therefore the work function increases. When the system is charged by adding electrons, their energy in the solid increases and it is easier to extract them: the work function decreases. Kraushofer et. al measured the work function of the stoichiometric surface using X-ray photoelectron spectroscopy (XPS).[79] They reported a value of 5.7 ± 0.2 eV, which differs from our DFT result by 8%. We did not find values for the other terminations, but it has to be taken into account that the electrochemical environment might difficult the measurement of the work function.

Slab size(bilayers)	E_{vacuum} (eV)	E_{Fermi} (eV)	W (eV)
Pristine			
5	5.63	0.49	5.15
7	6.86	1.68	5.18
11	8.56	3.36	5.20
Adsorbed OH group			
5	6.54	-0.39	6.93
7	7.89	0.96	6.93
11	9.73	2.80	6.93
Charged OH			
5	3.95	2.04	1.91
7	4.91	3.10	1.81
11	6.30	4.71	1.59

Table 4.3: Work function calculated at different slab sizes for the undoped systems. The Work function W was calculated as the difference between the energy in the middle of the vacuum E_{vacuum} and the E_{Fermi} energy. Both quantities were obtained from the DFT calculations. The energy E_{vacuum} was extracted from the macroscopic average of the potential distribution in the middle of the vacuum e.g., in the case of the 11-bilayered slabs the E_{vacuum} values were extracted from figure 4.13

We will show the influence of doping in the band bending and the electronic structure on the (0001) slab in the next chapter.

Chapter 5

DFT calculations in doped hematite slabs

As we discussed before, high doping leads to ultrathin space charge layers. However in the context of water splitting using hematite photoanodes, this regime is rarely explored in experiments and in theoretical calculations. In this chapter, we used density functional theory to show the effect of high doping on the behavior of the band bending and the electronic structure in the atomistic models we proposed for the (0001) hematite stoichiometric surface. We also show that the DFT calculations obtained in this work agree quantitatively and qualitatively with the band bending picture offered by the classical analysis.

We doped the systems described in the previous chapter with titanium atoms, which provide electrons to the slabs. We substituted on each slab, two Fe atoms located in the third position in the direction from the top of the surface to the bulk. The structure of the slabs we used in our DFT simulations are depicted in Figure 4.1. The donor density varies with slab size, since the number of doping atoms is constant and the volume of the slab increases as we added more bilayers of hematite. Despite of that, we still managed to obtain slabs with considerably high donor densities. The addition of the two Ti atoms represents donor densities of 2.5×10^{21} cm^{-3}, 1.8×10^{21} cm^{-3}, 1.4×10^{21} cm^{-3} and 1.15×10^{21} cm^{-3} for the slabs with 5, 7, 9 and 11 bilayers respectively.

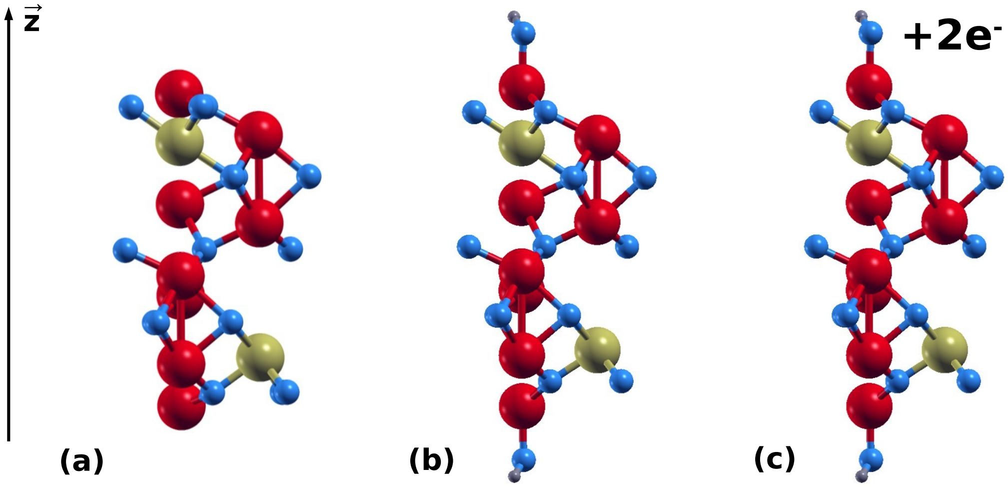

Figure 5.1: Atomistic models used to study the space charge layer in doped systems. The slab in (a) corresponds to the stoichiometric termination of the (0001) α-hematite surface doped with Ti, (b) corresponds to the latter slab with one additional hydroxyl group on each side (keeping the neutrality of the surface) and (c) illustrates the addition of two extra electrons to the slab in (b). In this case, the slabs consist of 5-bilayers of Fe_2O_3

5.1 Band bending

We determined the top of the valence band for the different slabs as we did in the previous chapter, using the projected density of states of the O-2p orbitals and setting the same thresholds. Figures 5.2, 5.3 and 5.4 show the local top of the valence band as a function of the positions of the oxygen atoms for the doped pristine slab, the slab with the adsorbed OH groups and the slab with the OH groups and two additional electrons, respectively. In the three figures we mentioned before, we show how the local top of the valence band behaves as we added additional bilayers of hematite to each system. The vertical dashed lines on each case show the position of the doping Ti atoms in the slabs. In general, we observed that in the doped case the structures developed by the valence band along the slabs did not follow a unitary trend in shape. Due to this irregularity, we decided to set the band bending as the difference between the maximum and minimum points in Figures 5.2, 5.3 and 5.4. This definition of the band bending can be problematic, since in some cases the

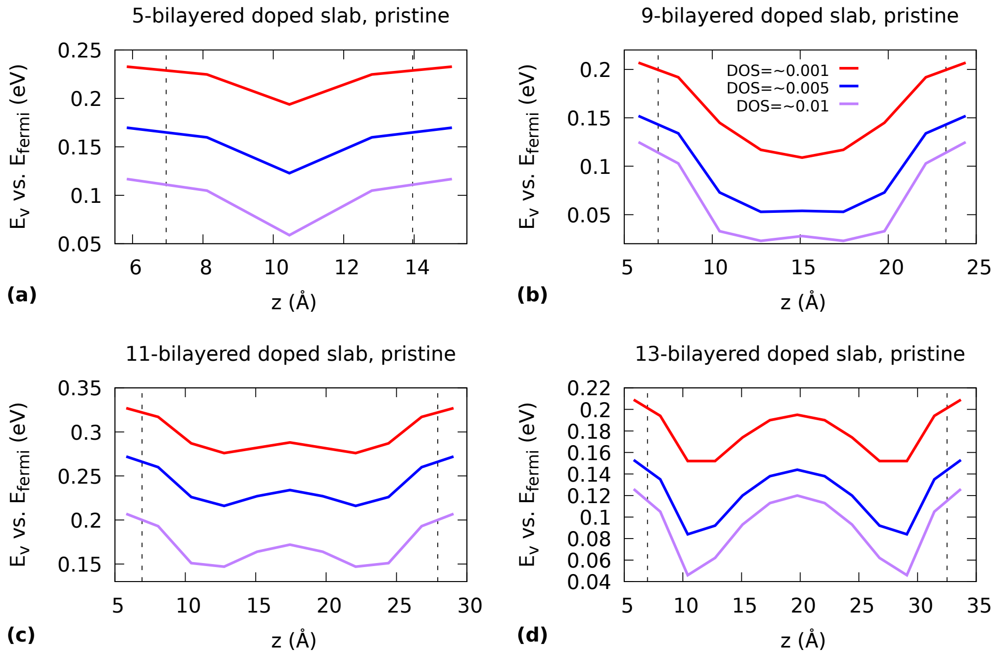

Figure 5.2: Top of the valence band with respect to the Fermi level vs. the positions of the oxygen atoms for doped stoichiometric slabs composed by a) 5-bilayers, b) 9-bilayers, c) 11-bilayers and d) 13-bilayers. As in the undoped case, the top of the valence band was measured using the O-2p orbitals. The dashed lines represent the positions of the Ti atoms used to doped the slabs.

minimum value of the energy is located at the surface. However, the actual quantity might be quite different. As commented in the last chapter, the band bending is ill-defined. It depends on many factors, including the position of the dopants, as it was shown by Yang et al.[80] in their study of Shottky barrier formation. A detail description of the band bending is out of the scope of this thesis, since it is a different research direction. However, we will keep the definition previously proposed to give the first steps towards the understanding of the band bending.

We plotted the trends developed by the band bending as the number of bilayers increased, in Figure 5.5. Despite the variety of shapes developed by the structures in Figures 5.2, 5.3 and 5.4, the trends in Figure 5.5 (b) suggest that the band bending in the neutral Ti-doped hydroxylated and the Ti-doped pristine systems converged. On the other hand,

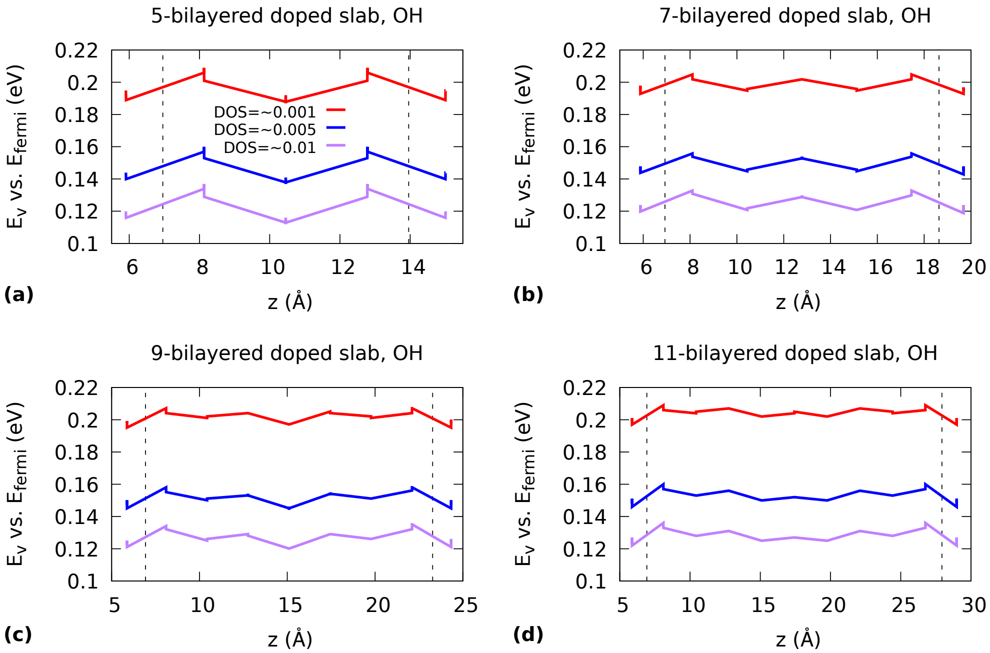

Figure 5.3: Top of the valence band with respect to the Fermi level vs. the positions of the oxygen atoms for doped stoichiometric slabs with additional OH groups composed by a) 5-bilayers, b) 7-bilayers, c) 9-bilayers and d) 11-bilayers. As in the undoped case, the top of the valence band was measured using the O-2p orbitals.

the charged slab with the adsorbed OH showed to be more problematic. In the latter case, convergence has not been reached using 11-bilayers, which might arise due to the complication of calculations in the presence of macroscopic electric fields.

The 11-bilayered slabs in the pristine case and in the case with adsorbed OH groups showed convergence in the band bending. The converged band bendings are ~ 0.07 eV and ~ 0.01 eV, respectively. These band bendings are one order of magnitude smaller than ones developed by the undoped slabs. Qualitatively, this makes sense in the band bending picture, since the additional electrons provided by the Ti atoms screen better the potential. We decided to connect the DFT results to the equation for the width of the space charge layer L_{sc} (Eq. 2.11), using the results from the converged slabs. In order to compute L_{sc}, we set the converged band bendings as the drop in the space charge layer ϕ_{sc}, and used the donor density we estimated for the 11-bilayered slabs. We found space

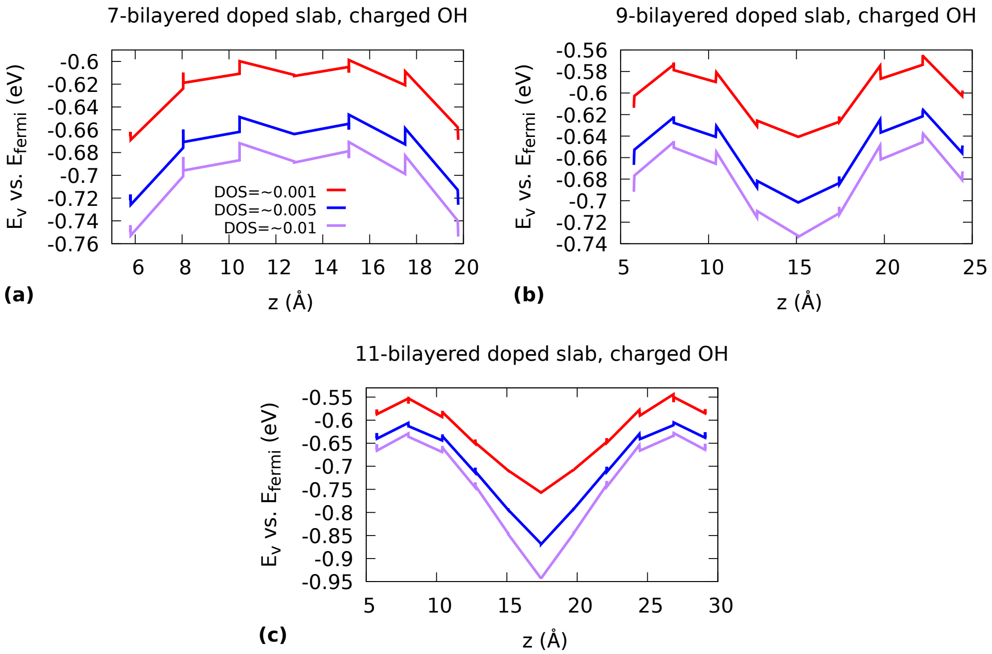

Figure 5.4: Top of the valence band with respect to the Fermi level vs. the positions of the oxygen atoms for doped stoichiometric slabs with additional OH groups and two additional electrons composed by a) 5-bilayers, b) 7-bilayers, c) 9-bilayers and d) 11-bilayers. As in the undoped case, the top of the valence band was measured using the O-2p orbitals.

charge layer widths of $\sim$ 6 Å and $\sim$ 3 Å for the doped pristine slab and for the doped slab with adsorbed OH groups, respectively. The $\sim$ 6 Å we found for the pristine slab is visible in the space charge structure developed in Figure 5.2 (c) and (d), which displayed L_{sc} between 5 Å and 6 Å. We could not observe the same in the case of the slab with the OH group, because in this case the calculated L_{sc} is too small and it is probably lost in the noise observed in Figure 5.3 (d). As we mentioned in the previous chapter, we were able to find a quantitative and qualitative correspondence between the results from our DFT calculations and the continuous model we used in this work. It is important to keep in mind that this connection was possible because these slabs are doped and because we are using the band bending from the valence band as the potential drop in the space charge layer.

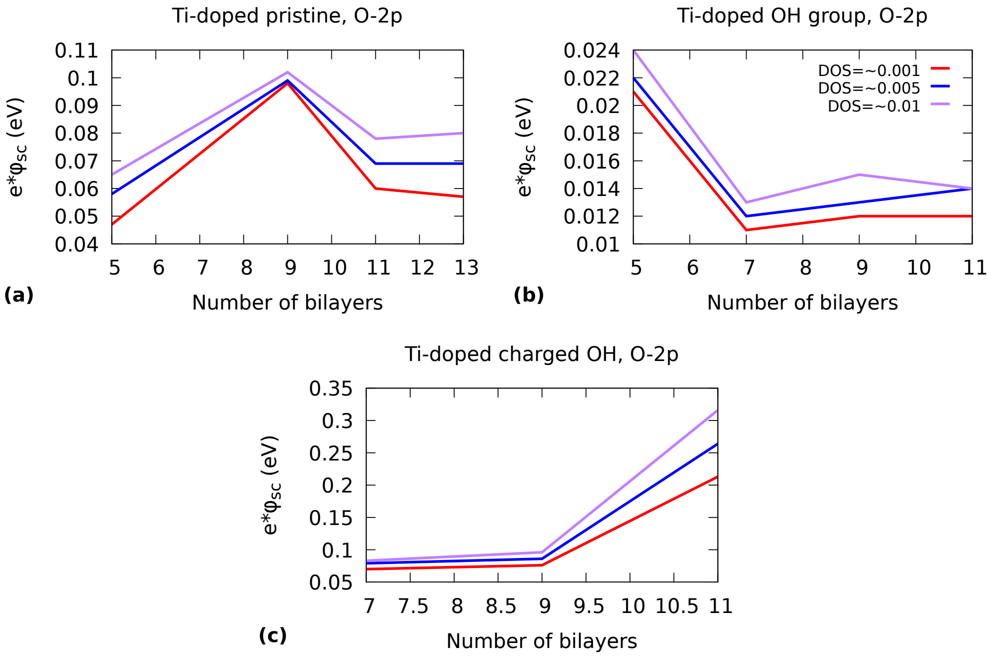

Figure 5.5: The bending of the top of the valence band as a function of the slab size for the doped (a) pristine, (b) OH-adsorbed hematite slabs and (c) OH-adsorbed with two additional electrons hematite slabs. The band bending on each case was computed as the difference between the highest and lowest points in Figures 5.2, 5.3 and 5.3. At some points in the graph, small jumps are visible. They are due to atoms with the same z coordinate having slightly different values of the displayed quantities.

We also checked the effect of high doping on the core Fe-3s orbitals. We selected the energies corresponding to the localized Fe-3s orbitals, and as in the previous chapter, we found two states for every Fe atom. Figure 5.6 shows these energies as a function of the positions of the iron atoms: (a) (b) pristine, (c) (d) adsorbed OH groups and (e) (f) charged slab with OH groups. We defined the band bending as the difference between the maximum and minimum of the Fe-3s energies for each slab. Figure 5.7 shows the band bending as a function of the slab size for the (a) doped pristine slab, (b) the slab with the adsorbed OH-groups and the one with the (c) adsorbed OH and two additional electrons. The latter result suggest that the band bending converged for the Ti-doped pristine slab and for the Ti-doped slab with adsorbed OH groups, see (a) and (b), respectively.

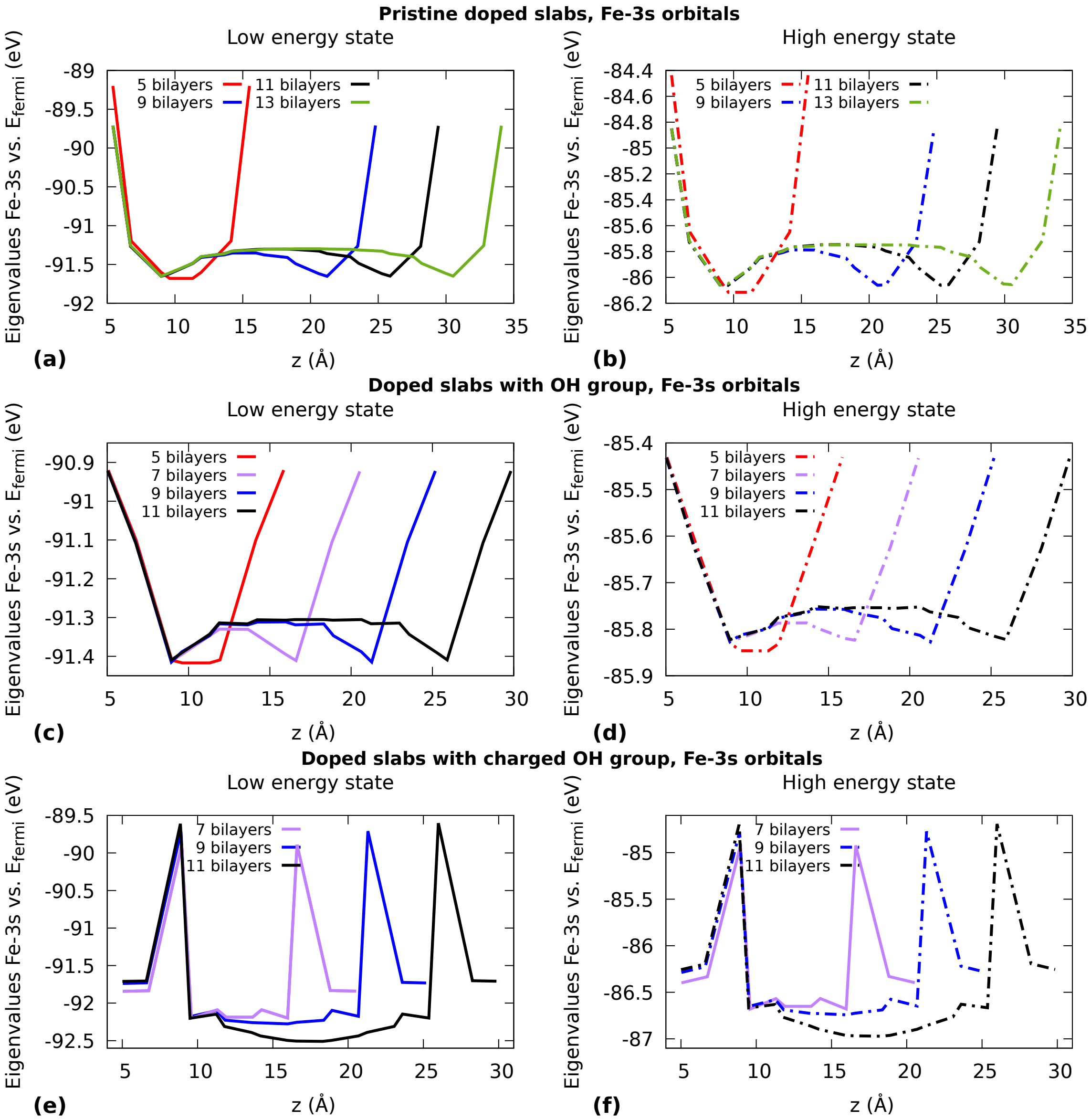

Figure 5.6: Bending of the energy bands of the localized Fe-3s orbitals along the doped slabs with different sizes. Two states with different energy levels were found on each Fe atom for the (a) pristine-doped slab and (b) the slabs with one OH group attached to each side. The low energy state (solid lines) and high energy state (dashed lines) corresponded to two different eigenvalues. The flatness developed on the center of the slabs as the size of the slabs increase, might be a signal of saturation.

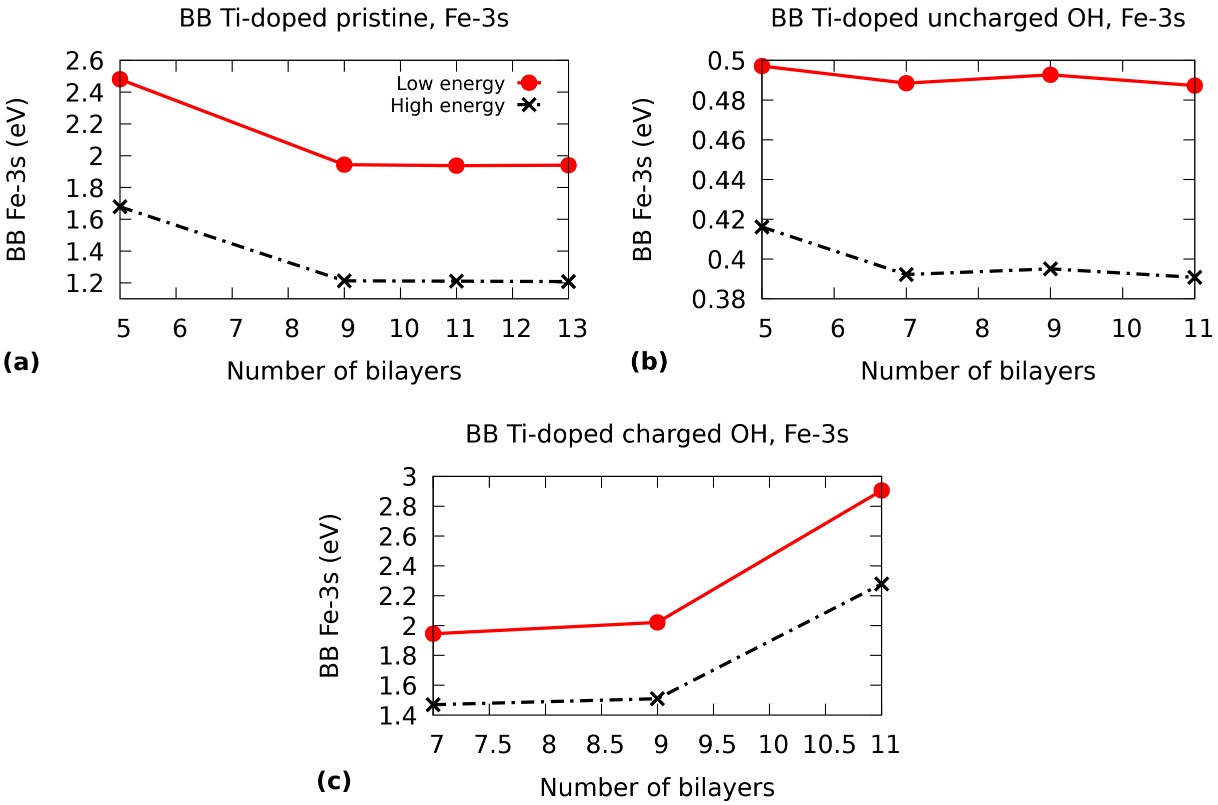

Figure 5.7: Trends in the bending of the Fe-3s orbitals energy bands along the doped slabs. The band bending on each case was computed as the difference between the highest and lowest points in the plots Fig. 5.6.

The flatness developed by the Fe-3s energy bands in the middle of the slabs might be a signature of the convergence of the slabs, see 5.6 (a), (b), (c) and (d). In these cases, it is possible to see space charge layer-like structures in the Ti-doped pristine slab and in the Ti-doped slab with adsorbed OH groups. If we assume that L_{sc} can be measured from the surface to the minima in Figure 5.6, it takes values of ~ 5 Å in the pristine case and ~ 4 Å in the neutral OH case. Which agree qualitatively with the picture obtained using the O-2p orbitals and the continuous equations, where L_{sc} took values of ~ 6 Å and ~ 3 Å respectively. We want to clarify that in this case, it is not possible to make a quantitative connection with Eq. 2.11, since in this analysis we are dealing with core states and not with states from the valence band. We did not do the same analysis in the charged OH

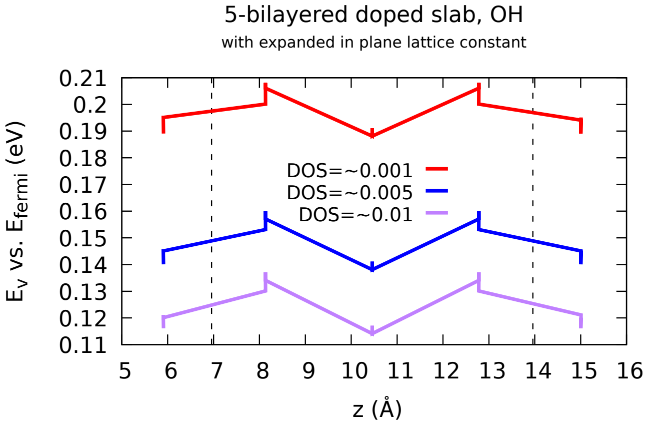

Figure 5.8: Top of the valence band with respect to the Fermi level vs. the positions of the oxygen atoms for the 5-bilayered doped stoichiometric slab with additional OH groups and expanded in-plane lattice constant. The lattice constant was expanded 0.4205% with respect to the one of pure hematite according to the experimental values reported for hematite and ilmenite. As in the previous cases, the top of the valence band was measured using the O-2p orbitals. The band bending takes values of 0.02 eV, 0.022 eV and 0.023 eV for the 0.001 a.u., 0.005 a.u and 0.01 a.u. thresholds respectively. These values are practically the same as the one reported for the fully relaxed structure previously reported.

slab, since this calculation is not converged and the space-charge structure is not clear here, see Figure 5.6(e) and (f). In the three systems the Fe-3s bands bent in a greater extent than the valence band (calculated from the PDOS of the O-2p orbital states). We did not find any kind of quantitative correlation between both quantities. Qualitatively, the larger the BB of the valence band, the larger the BB of the Fe-3s energy band.

We used the in-plane lattice constant from bulk hematite to model the slabs in the Ti-doped systems. Experimentally, it has been observed that high levels of doping with Ti lead to the expansion of the lattice constant. For example, the lattice constant expands 1% in isostructural ilmenite (which contains 50% Ti) with respect to hematite. We tested the effect of the expansion of the lattice constant in the band bending to show the robustness of our calculations. In this case, we performed the test in the 5-bilayered doped slab with adsorbed OH groups. The 5-bilayered slabs have the largest doping density in our calculations, which corresponds to 20% Ti. We made a slab with an expanded in-plane lattice constant, while keeping the z-directions positions obtained in the relaxation of the original 5-bilayered cell. We expanded the lattice constant 0.4205% with respect to the one of pure hematite according to the experimental values reported for hematite and ilmenite. Figure 5.8 shows the local top of the valence band as a function of the oxygen atoms positions in the slab. As we did before, we computed the band bending. In this case, we obtained practically the same results as in the system without the expansion of the cell, see Figure 5.8. The latter confirms the little effect of the expansion of the lattice constant in our conclusions.

5.2 Electronic structure of the space charge layer

Figure 5.9 shows the projected density of states (PDOS) for the (a) pristine slab, (b) the slab with the adsorbed OH groups and (c) the slab with the OH groups and two additional charges. In this figure the PDOS is multiplied by a factor of 2.5 to compare better the contributions from the atoms close to the surface. We still observe the presence of empty states at the top of the valence band in the case of the two charge-neutral slabs, see Fig. 5.9 (a) and (b). In the doped-pristine slab, we found that the contribution from the O-2p orbitals states is not longer dominant at the top of the valence band. By doping, the contribution from the 3-d orbitals from the Fe atoms becomes substantial in this region, as shown by the blue line in Figure 5.9 (a). These states were empty in the undoped case (Fig. 4.9 (a)) and were filled with the electrons donated by the titanium atoms.

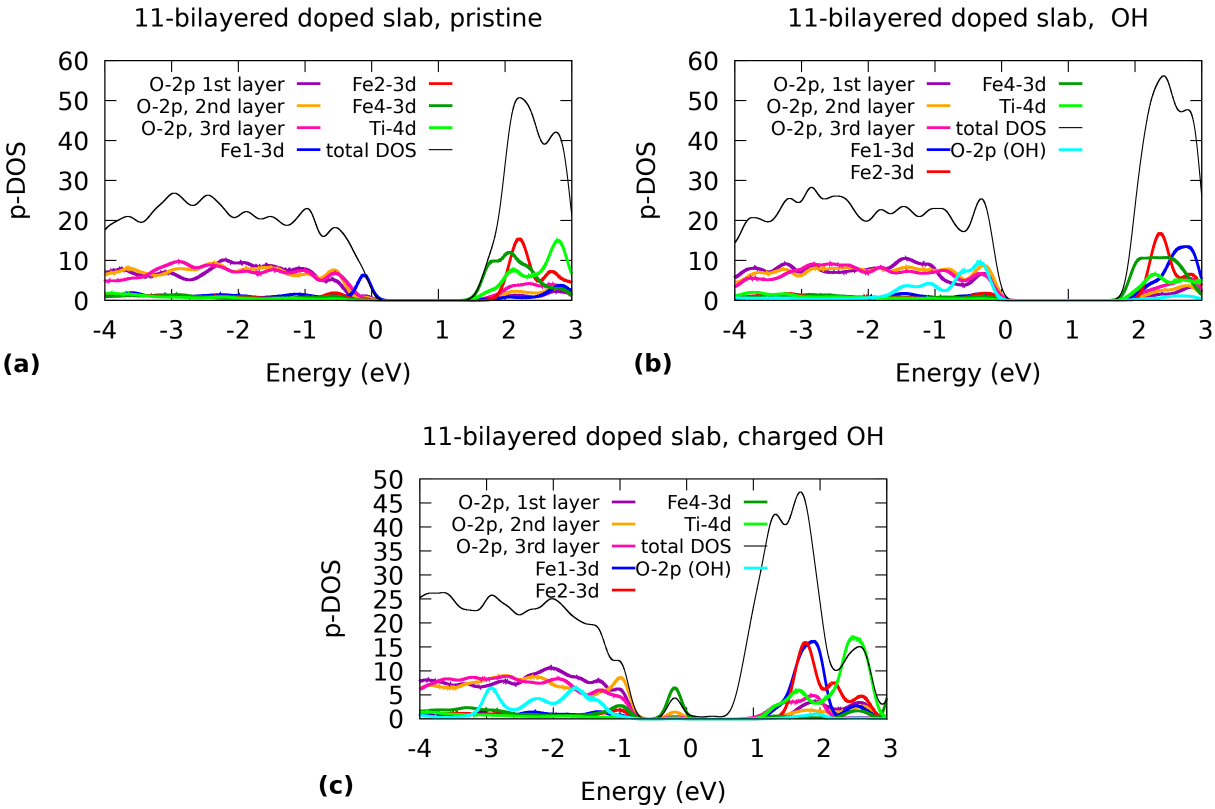

Figure 5.9: Projected density of states of the (a) pristine, (b) OH-adsorbed and (c) OH-adsorbed with two additional electrons doped hematite slabs with 11-bilayers. The pdos plotted for the different orbitals were multiplied by a factor of 2.5 to make them more visible. The density of states is adjusted to correspond to half of the atoms from the same side of the slab.

In the case of the neutral slab with the OH groups, the O-2p orbitals continue to be dominant at the top of the valence band as shown by the purple, orange and pink lines in Figure 5.9 (b) and (c). In this case we observed that the amount of empty states at the top of the valence band decreased considerably in comparison with the undoped case, see Figures 4.9 (b) and 5.9 (b). This situation is reflected in the reduction of the band bending from 0.14 eV in the undoped case, to 0.01 eV in the doped case. In this case, the empty states in the undoped case were filled with the electrons provided by the Ti atom.

The main changes we observed in the PDOS of the slabs with adsorbed OH groups by

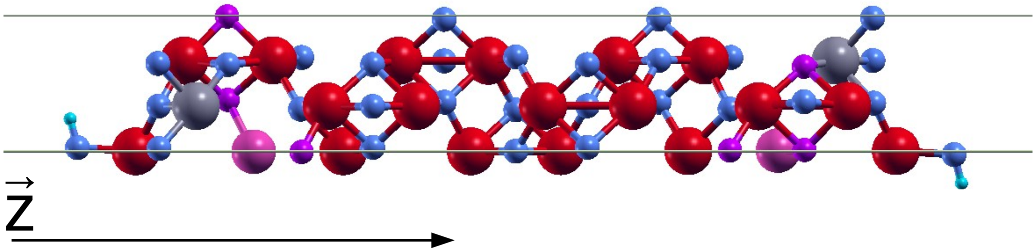

Figure 5.10: Nature of the states from the gap in the doped slab with and adsorbed OH group and two additional charges. This figure corresponds to the 11-bilayered slab plotted in the $\vec{z}$ direction. The spheres in red represent the iron atoms, the blue represent the oxygen atoms, the gray represent the titanium atoms and the cyan represents the hydrogen atoms. The spheres in pink and purple show the iron and oxygen atoms, respectively, which contribute the most to the state in the gap.

adding two extra electrons are: the complete filling of the valence band and the emergence of filled states in the middle of the gap. The O-2p states continue to be the dominant states at the top of the valence band. The states in the gap are mainly constituted by 3d-orbitals from the Iron atoms represented with pink spheres in Figure 5.10 and from the O-2p states from the oxygen atoms represented by the purple spheres in the same Figure. Seriani et al. reported similar states appearing in the gap of systems composed by TiO_2 surfaces and small copper clusters,[81] where they reported these gap states correspond to polaronic states.

A polaron forms when a charge carrier moves slowly enough to displace the surrounding atoms due to their mutual interaction. The latter leads to the formation of a potential well that lowers the energy of the carrier and fosters its confinement.[82] They can be characterized by the magnetic moment of the atom where they form, the charge of the atom and the geometric distortion around that atom.[81] Since the determination of the effective charges might be arbitrary, this would complicate the identification of polarons. As a better indicator of the presence of polarons, Seriani et al.[81] and other authors[83–86] suggest to check the spin localization, which can be identified by the increase of the magnetic moments. We observed that the greatest change in magnetic moment, occur in the iron atoms which contribute to the gap states in Figure 5.9(c) and which we previously identified in Figure

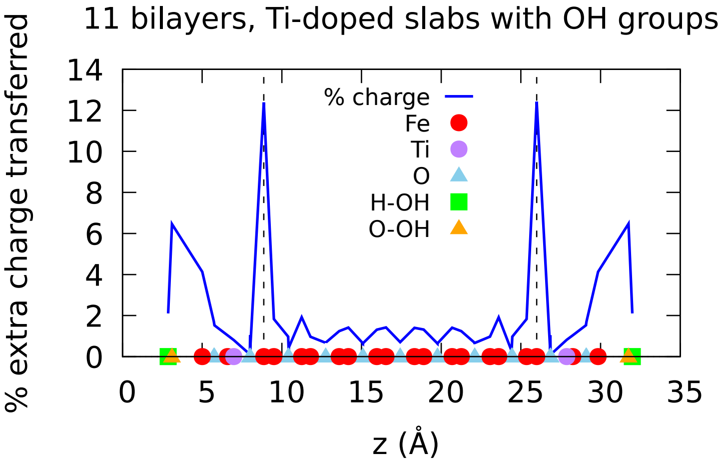

Figure 5.11: Percentage of Löwdin charges transferred to every atom by the addition of two extra electrons in the doped slab with OH groups. This calculation corresponds to the 11-bilayered slabs. The position of the atoms in the slabs are represented by geometrical figures. The red circles correspond to the Fe atoms, the purple circles to the doping Ti atoms, the blue triangles to the oxygen atoms in hematite, the green squares to the H atoms from the OH groups and the yellow triangles to the O atoms from the OH groups. It can be seen that the greatest percentage of charge is received by the Fe atoms represented by the pink spheres in Figure 5.10. The dashed lines show the position of these Fe atoms.

5.10. These Fe atoms also received a substantial part of the charge added to the OH slabs, as it can be seen in Figure 5.11. According to the Löwdin charges analysis, the Fe atoms gained +|0.21|e from the two additional electrons added to this slab; while each oxygen atom from the hydroxyl groups gained +|0.11|e and the rest of the charge is the delocalized along the slab. We also observed geometric distortions of the atomic configuration around these Fe atoms, in comparison to the neutral slab with the OH groups. The latter facts suggest that the state we found in the gap corresponds to a polaron.

It is well known that excess charge carriers form polarons in hematite[6,82,87] and in many other transition-metal oxides.[82] In the case of hematite, excess electrons tend to localize in iron atoms, leading to the formation of small polarons. The latter implies the reduction of Fe^{3+} to Fe^{2+}.[6] DFT+U simulations and quantum mechanical calculations have shown that doping hematite leads to the formation of electron polarons on a nearby Fe atom to the doping atoms, when Fe atoms are substituted by Si, Ge, Zr and Sn.[6,88,89] In the case of Ti-doping, some experiments reported that the presence of Ti^{4+} did not lead to the formation of Fe^{2+}, which mean that polarons do not form just by Ti-doping.[6,90] The latter agrees with the calculations from Ref. 89 and our DFT+U calculations for the neutral Ti-doped slabs, where we did not observed polarons. The addition of the electrons in our calculations triggered the appearance of polarons. The latter suggest that the addition of electrons from sources different to Ti-doping might lead to the experimental observation of polarons in this system.

Despite the calculations of the charged slabs are not converged with slab size, the latter discussion on polarons is valid since this is a local effect: We observed the same polaron, located in the same position and the same magnetic and electronic structure, regardless of the slab size. As we mentioned before, the fact that the calculations are not converged with slab size does not mean that the DFT calculations are not converged. The same is true for the smaller slabs of the uncharged systems. As we did in the last chapter, we also analyzed the nature of the states in the valence band and the conduction band. We were not able to identify surface states at the top of the valence band in any system, our DFT calculations did not provide enough resolution to do it. However, we still manage to find bulk states at the bottom of the conduction band. And also found surface states in the conduction band in the slabs with the OH groups, in both uncharged and charged cases. In the neutral slab with the OH group, we found surface states 0.8 eV, 1eV and 1.15 eV deep into the conduction band. In the case of the charged slab we found surface states located at depths of 1.1 eV and 1.5 eV in the conduction band.

5.3 Potential distribution and work function

Figure 4.13 shows the planar and macroscopic averages of the potential across the doped slabs with 11 bilayers in the case of the (a) pristine slab, (b) the slab with the adsorbed OH groups and the (c) the slab with the OH group and the additional charges. The position of

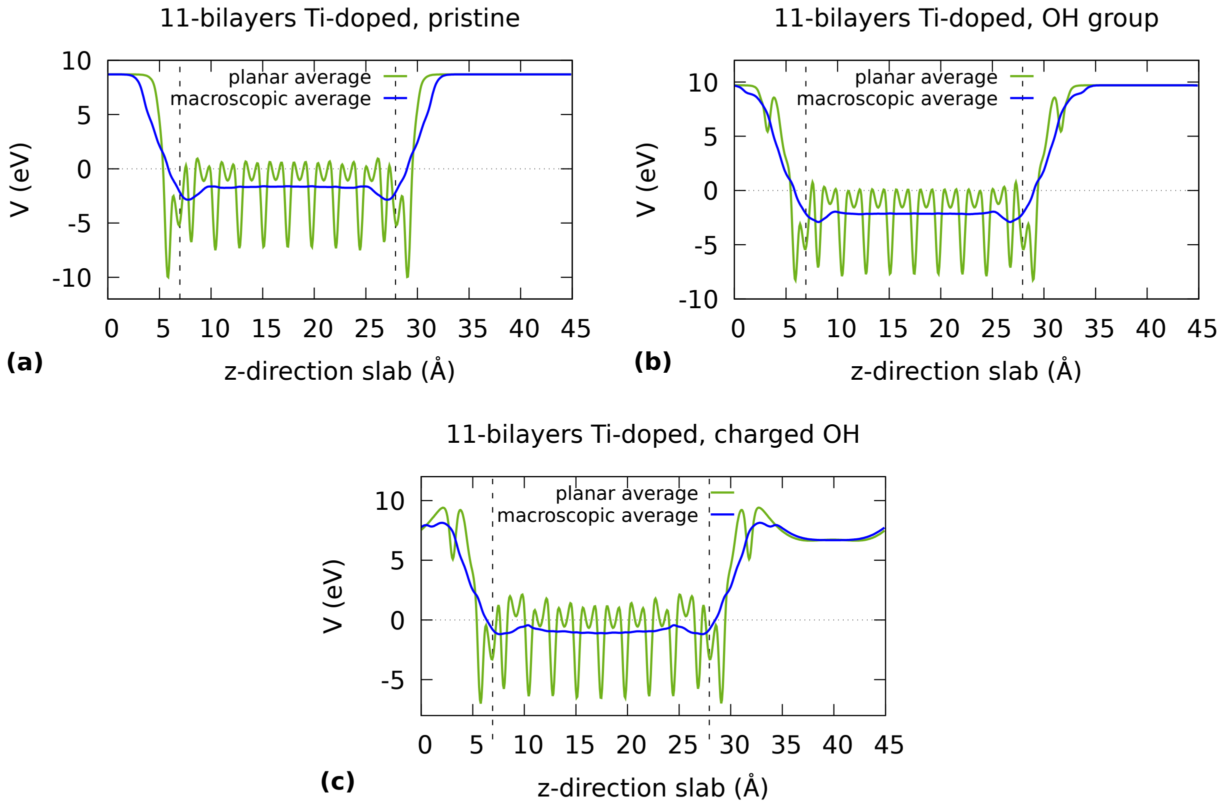

Figure 5.12: Planar and macroscopic averages of the potential across the 11-bilayered doped hematite slabs. The resulting potential across the doped slabs: pristine slab, slab with an adsorbed OH molecule (OH group), and the slab with the OH molecule plus two additional charges (charged OH), can be seen in figure (a), (b) and (c) respectively.

the doping atoms is represented by the dashed-vertical lines. The position of the plateau both in the vacuum and in the center of the slab did not change substantially. The latter is reflected in the calculated work functions, see 5.1. We computed the work functions for the three systems at different slab sizes. The values converged in the largest slabs for the pristine slab and the neutral slab with the attached OH. The calculated work functions in both systems showed a difference of 0.1 eV in comparison with their undoped analogues. These calculations suggest that doping does not have a major impact on the work functions. However, it can be seen that in the doped case, the neutral slabs with the attached OH still show work functions higher than the pristine case (as in the undoped case). The lack of convergence of the charged slabs is evident in the work functions calculated for different slab sizes in table 5.1.

Slab size	E_{vacuum} (eV)	E_{Fermi} (eV)	W (eV)
Pristine-doped			
5	5.80	0.38	5.42
11	8.71	3.38	5.32
13	9.29	3.99	5.30
OH group-doped			
5	6.56	-0.31	6.87
7	7.88	1.02	6.85
9	8.90	2.04	6.86
11	9.70	2.85	6.86
Charged OH-doped			
7	5.44	3.59	1.86
9	6.12	4.34	1.78
11	6.67	5.03	1.64

Table 5.1: Work function calculated at different slab sizes for the doped systems. As in the previous chapter, the work function W was calculated as the difference between the energy in the middle of the vacuum E_{vacuum} and the E_{Fermi} energy. The energy E_{vacuum}values from the 11-bilayered slabs were extracted from the macroscopic average of the potential in the middle of the vacuum, see figure 5.12.

Conclusions

In this work, we studied the space charge layer in hematite photoanodes by means of the Poisson-Boltzmann equations, the Stern model and density functional theory, due to its relevance in the photoelectrocatalytic water oxidation. Recently, the presence of ultrathin space charge layers has been experimentally observed under water splitting conditions, which occurs at high doping conditions. However this regime is rarely explored. We used a continuous model based on the Stern model and the Poisson-Boltzmann equations to explore a series of water-splitting experimental data and to examine the consequences of the high doping regime on the interface. Finally, we used density functional theory to get an atomistic insight into the space charge layer in the stoichiometric (0001) hematite surface. These are the main conclusions we draw from our study:

1. Using the continuous equations, we detected ultrathin space charge layers with thicknesses of ~ 10 Å in experiments employing highly-doped nanostructured hematite films. These experiments also displayed a regime of high photoelectrocatalytic efficiency, which is unexpected given the small size of the space charge layers in the samples. The substantial volume-fraction of the electrode, occupied by the space charge layer, plays a role in the efficiency observed in these films. Such thin space charge layers are in principle accessible to quantum mechanical ab-initio calculations.
2. At high doping densities a substantial fraction of the potential drop is located in the Helmholtz layer, which according to our calculations can take values between 0.1 V and 0.6 V. This contrasts with the conventional behavior of the interface, where the

potential drop in the space charge layer dominates. And which is considered necessary for the separation and transport of charge carriers under water splitting conditions. The substantial drop in the Helmholtz layer happens at the same high doping conditions where ultrathin space charge layers develop. This regime might probably give place to considerable molecular and ionic rearrangements in the Helmholtz layer. It also leads to modifications to the usual Mott-Schottky relation between the inverse of the square capacitance and the applied voltage, which holds in the depletion approximation. At high doping densities, we showed that the Mott-Schottky relation becomes quadratic in the applied bias close to the flatband potential. Far from flatband conditions, the Mott-Schottky relation shows a sub-linear behaviour which follows from a quadratic correction.

3. This kind of analysis should always be done whenever experiments are performed in semiconductor-electrolyte interfaces. We did this analysis on the hematite-electrolyte interface under water splitting conditions, but this study can be extended to other systems e.g., other oxides. Experimentalists should perform this kind of analysis to get an estimate on the space charge layer width and the potential drops whenever they characterize their samples with the Mott-Shottky analysis. This should become a standard way to analyze the experimental data, which could provide insight into why experiments lead to different outcomes, compare experiments and provide more insight into the electrostatics.

4. We showed Density Functional Theory describes space charge layers at an atomistic level. We studied the evolution of the space charge layer in models that range from the pristine stoichiometric surface to the doped hydroxylated surface with additional electrons. Using DFT, we calculated the band bendings displayed in every surface and we got an atomistic insight into the electronic structure of the space charge layer in every case. The band bending showed to be independent of the particular choice of threshold used to calculate it, once it reaches saturation with the slab thickness. Band bending convergence was achieved for the pristine slab and for the neutral slab with two additional OH groups, in both undoped and doped conditions. The band

bending did not reach saturation for the surface with adsorbed OH groups and two additional electrons, in any case. We calculated band bendings of ∼0.14 eV for the undoped pristine surface and ∼0.49 eV for the neutral surface with adsorbed OH. The larger band bending in the OH-terminated surface agrees qualitatively with chemical intuition, given that the OH group attracts negative charge to the surface. In the doped case, we found band bendings of ∼ 0.07 eV and ∼ 0.01 eV for the pristine and OH-terminated slabs, respectively. The decrease of the band bending with Ti-doping can be explained by the better screening of the potential provided by the Ti-donated electrons. The latter band bendings correspond to space charge layer widths of ∼6 Å and ∼3 Å, where the first is visible in the larger pristine slab. The DFT results for the doped slabs showed a qualitative and quantitative correspondence with the continuous model. The quantitative correspondence just occurs in the doped case because the band bendings observed in the undoped slabs have an intrinsic origin, and therefore there is no connection with the continuous model. Despite the limitations imposed by the minimalistic description of our systems, we managed to gain an insight of the electronic structure of space charge layers in hematite surfaces. Here we disregarded the effect of the electrolyte to focus on the development of the space charge layer in the solid. The simulation of the electrolyte would have implied a large amount of computational resources. Considering the electrolyte means charging the surface, therefore one must consider the ions and the water molecules. The non-static nature of the liquid is another important factor to take into account, given that many configurations of the system are required in the calculations. The latter can in principle be achieved using ab initio molecular dynamics calculations. Although the latter research area is really active, one has to sacrifice either the solid part or the liquid. The simulation of the full interface is still a challenge.

Bibliography

[1] K. Sivula, F. Le Formal, and M. Grätzel. Solar water splitting: Progress using hematite photoelectrodes. *ChemSusChem*, 4:432, 2011.

[2] F. E. Osterloh and B. A. Parkinson. Recent developments in solar water-splitting photocatalysis. *MRS Bulletin*, 36(1):17, 2011.

[3] H. Dau, C. Limberg, T. Reier, M. Risch, S. Roggan, and P. Strasser. The mechanism of water oxidation: From electrolysis via homogeneous to biological catalysis. *ChemCatChem*, 2:724, 2010.

[4] M. G. Walter, E. L. Warren, J. R. McKone, S. W. Boettcher, Q. Mi, E. A. Santori, and N. S. Lewis. Solar water splitting cells. *Chem. Rev.*, 110:6446, 2010.

[5] M. D. Bhatt and J. S. Lee. Recent theoretical progress in the development of photoanode materials for solar water splitting photoelectrochemical cells. *J. Mater. Chem. A.*, 3:10632, 2015.

[6] N. Seriani. Ab initio simulations of water splitting on hematite. *J. Phys.: Condens. Matter*, 29:463002, 2017.

[7] K. Sivula, R. Zboril, F. Le Formal, R. Robert, A. Weidenkaff, J. Tucek, J. Frydrych, and M. Gratzel. Photoelectrochemical water splitting with mesoporous hematite prepared by a solution-based colloidal approach. *J. Am. Chem. Soc.*, 132:7436, 2010.

[8] R. E. Blankenship et al. Comparing photosynthetic and photovoltaic efficiencies and recognizing the potential for improvement. *Science*, 332:805, 2011.

[9] A. Fujishima and K. Honda. Electrochemical photolysis of water at a semiconductor electrode. *Nature*, 238:37, 1972.

[10] A. Hellman and R. G. S. Pala. First-principles study of photoinduced water-splitting on fe2o3. *J. Phys. Chem. C*, 115:12901, 2011.

[11] X. Wang, A. Kafizas, X. Xiaoe Li, S. J. A. Moniz, P. J. T. Reardon, J. Tang, I. P. Parkin, and J. R. Durrant. Transient absorption spectroscopy of anatase and rutile: The impact of morphology and phase on photocatalytic activity. *J. Phys. Chem. C*, 119(19):10439, 2015.

[12] J. Bisquert. *Nanostructured energy devices, Equilibrium Concepts and Kinetics.* CRC Press, Universitat Jaume I, Castelló, Spain, 1 edition, 2015.

[13] Yu. V. Pleskov and Yu. Ya. Gurevich. *Semiconductor Photoelectrochemistry.* Consultants Bureau, New York, 1 edition, 1986.

[14] H. Helmholtz. Studien über electrische grenzschichten. *Ann. Phys.*, 243:337, 1879.

[15] M. Gouy. Sur la constitution de la charge électrique à la surface d'un électrolyte. *J. Phys. Theor. Appl.*, 9:457, 1910.

[16] D. L. Chapman. A contribution to the theory of electrocapillarity. *Philos. Mag. J. Sci.*, 25:475, 1913.

[17] O. Stern. Zur theorie der elektrolytichen doppelschicht. *Z. Elecktrochem. Angew. Phys. Chem.*, 30:508, 1924.

[18] K. Shimizu, A. Lasia, and J.-F. Boily. Electrochemical impedance study of the hematite/water interface. *Langmuir*, 28:7914, 2012.

[19] K. Shimizu and J. F. Boily. Electrochemical properties and relaxation times of the hematite/ water interface. *Langmuir*, 30:9591, 2014.

[20] K. Shimizu, J. Nystrom, P. Geladi, B. Lindholm-Sethson, and J.-F. Boily. Electrolyte ion adsorption and charge blocking effect at the hematite/aqueous solution interface: an

electrochemical impedance study using multivariate data analysis. *Phys. Chem. Chem. Phys.*, 17:11560, 2015.

[21] K. Shimizu and J.-F. Boily. Electrochemical signatures of crystallographic orientation and counterion binding at the hematite/water interface. *J. Phys. Chem. C*, 119:5988, 2015.

[22] M. Lucas and J.-F. Boily. Mapping electrochemical heterogeneity at iron oxide surfaces: A local electrochemical impedance study. *Langmuir*, 31:13618, 2015.

[23] M. Lucas and J. F. Boily. Electrochemical response of bound electrolyte ions at oriented hematite surfaces: A local electrochemical impedance spectroscopy study. *J. Phys. Chem. C*, 121:27976, 2017.

[24] B. Iandolo, H. Zhang, B. Wickman, I. Zorić, G. Conibeer, and A. Hellman. Correlating flat band and onset potentials for solar water splitting on model hematite photoanodes. *RSC Adv.*, 5:61021, 2015.

[25] B. Klahr, S. Gimenez, F. Fabregat-Santiago, T. Hamann, and J. Bisquert. Water oxidation at hematite photoelectrodes: The role of surface states. *J. Am. Chem. Soc.*, 134(9):4294, 2012.

[26] O. Zandi and T. W. Hamann. Enhanced water splitting efficiency through selective surface state removal. *J. Phys. Chem. Lett.*, 5:1522, 2014.

[27] F. Le Formal, N. Tétreault, M. Cornuz, T. Moehl, M. Grätzel, and K. Sivula. Passivating surface states on water splitting hematite photoanodes with alumina overlayers. *Chem. Sci.*, 2:737, 2011.

[28] Z. Zhang, H. Nagashima, and T. Tachikawa. Ultra-narrow depletion layers in a hematite mesocrystal-based photoanode for boosting multihole water oxidation. *Angew. Chem. Int. Edit.*, 59:9047, 2020.

[29] K. Ulman, M.-T. Nguyen, N. Seriani, S. Piccinin, and R. Gebauer. A unified picture of water oxidation on bare and gallium oxide-covered hematite from density functional theory. *ACS Catal.*, 7:1793, 2017.

[30] M. H. Dahan and M. C. Toroker. Water oxidation catalysis with fe2o3 constrained at the nanoscale. *J. Phys. Chem. C*, 121:6120, 2017.

[31] O. Neufeld and M. C. Toroker. Platinum-doped -fe2o3 for enhanced water splitting efficiency: A dft+u study. *J. Phys. Chem. C*, 119:5836, 2015.

[32] K. Ulman, E. Poli, N. Seriani, S. Piccinin, and R. Gebauer. Understanding the electrochemical double layer at the hematite/water interface: A first principles molecular dynamics study. *J. Chem. Phys.*, 150:041707, 2019.

[33] N. J. English, M. Rahman, N. Wadnerkar, and J. M. D. MacElroy. Photo-active and dynamical properties of hematite (fe2o3)–water interfaces: an experimental and theoretical study. *Phys. Chem. Chem. Phys.*, 2016:14445, 2014.

[34] S. Zhang, X. Gu, Y. Zhao, and Y. Qiang. Enhanced photoelectrochemical performance of tio2 nanorod arrays by a 500°c annealing in air: Insights into the mechanism. *J. Electron. Mater.*, 45:648, 2016.

[35] O. M. Magnussen and A. Groß. Toward an atomic-scale understanding of electrochemical interface structure and dynamics. *J. Am. Chem. Soc.*, 141:4777, 2019.

[36] R. E. Bangle, J. Schneider, D. T. Conroy, B. M. Aramburu-Trošelj, and G. J. Meyer. Kinetic evidence that the solvent barrier for electron transfer is absent in the electric double layer. *J. Am. Chem. Soc.*, 142(35):14940, 2020.

[37] C. G. Malmberg and A. A. Maryott. Dielectric constant of water from 0° to 100°c. *J. Res. Natl. Inst. Stand. Technol.*, 56(1):1, 1956.

[38] R. Buchner, G. Hefter, P. M. May, and P. Sipos. Dielectric relaxation of dilute aqueous naoh, naal(oh) 4 , and nab(oh) 4. *J. Phys. Chem. B*, 103:11186, 1999.

[39] T. Chen, G. Hefter, and R. Buchner. Dielectric spectroscopy of aqueous solutions of kcl and cscl. *J. Phys. Chem. A*, 107:4025, 2003.

[40] A. Levy, D. Andelman, and H. Orland. Dielectric constant of ionic solutions: A field-theory approach. *Phys. Rev. Lett.*, 108:227801, 2012.

[41] B. E. Conway, J. O'M. Bockris, and I. A. Ammar. The dielectric constant of the solution in the diffuse and helmholtz double layers at a charged interface in aqueous solution. *Trans. Faraday Soc.*, 47:756, 1951.

[42] S. Chatman, P. Zarzycki, and K. M. Rosso. Surface potentials of (001), (012), (113) hematite (a-fe2o3) crystal faces in aqueous solution. *Phys. Chem. Chem. Phys.*, 15:13911, 2013.

[43] J. A. Glasscock, P. R. F. Barnes, I. C. Plumb, A. Bendavid, and P. J. Martin. Structural, optical and electrical properties of undoped polycrystalline hematite thin films produced using filtered arc deposition. *Thin Solid Films*, 516(8):1716, 2008.

[44] R. K. Quinn, R. D. Nasby, and R. J. Baughman. Photoassisted electrolysis of water using single crystal -fe2o3 anodes. *Mat. Res. Bull.*, 11:1011, 1976.

[45] John H. Kennedy. Flatband potentials and donor densities of polycrystalline alpha-fe203 determined from mott-schottky plots. *J. Electrochem. Soc.*, 125(5):723, 1978.

[46] J. C. Papaioannou, G. S. Patermarakis, and H. S. Karayianni. Electron hopping mechanism in hematite (alpha-fe2o3). *J. Phys. Chem. Solids*, 66:839, 2005.

[47] X. Yang, A. Wolcott, G. Wang, A. Sobo, R. C. Fitzmorris, F. Qian, J. Z. Zhang, and Y. Li. Ultra-narrow depletion layers in a hematite mesocrystal-based photoanode for boosting multihole water oxidation. *Nano Lett.*, 9:2331, 2009.

[48] A. Rokade, S. Rodniya, V. Sharma, M. Prasad, H. Pathan, and S. Jadkar. Electrochemical synthesis of 1d zno nanoarchitectures and their role in efficient photoelectrochemical splitting of water. *J. Solid State Electrochem.*, 21:2639, 2017.

[49] J. P. Perdew, K. Burke, and M. Ernzerhof. Generalized gradient approximation made simple. *Phys. Rev. Lett.*, 77:3865, 1996.

[50] P. Giannozzi, S. Baroni, N. Bonini, M. Calandra, R. Car, C. Cavazzoni, D. Ceresoli, G. L Chiarotti, M. Cococcioni, I. Dabo, A. Dal Corso, S. de Gironcoli, S. Fabris, G. Fratesi, R. Gebauer, U. Gerstmann, C. Gougoussis, A. Kokalj, M. Lazzeri, L. Martin-Samos, N. Marzari, F. Mauri, R. Mazzarello, S. Paolini, A. Pasquarello, L. Paulatto, C. Sbraccia, S. Scandolo, G. Sclauzero, A. P. Seitsonen, A. Smogunov, P. Umari, and R. M. Wentzcovitch. Quantum espresso: a modular and open-source software project for quantum simulations of materials. *J. Phys.: Condens. Matter*, 21(39):395502, 2009.

[51] V. I. Anisimov, J. Zaanen, and O. K. Andersen. Band theory and mott insulators: Hubbard u instead of stoner. *Phys. Rev. B*, 44:943, 1991.

[52] M. Cococcioni and S. de Gironcoli. Linear response approach to the calculation of the effective interaction parameters in the lda+u method. *Phys. Rev. B*, 71:035105, 2005.

[53] M.-T. Nguyen, N. Seriani, and R. Gebauer. Water adsorption and dissociation on alpha-fe2o3 (0001): Pbe+u calculations. *J. Chem. Phys.*, 138:194709, 2013.

[54] J. M. D. Coey and G. A. Sawatzky. A study of hyperfine interactions in the system (fe1-xrhx)2o3 using the mossbauer effect (bonding parameters). *J. Phys. C*, 4:2386, 1971.

[55] E. Krén, P. Szabó, and G. Konczos. Neutron diffraction studies on the (1x) fe2o3xrh2o3 system. *Phys. Lett.*, 19:103, 1965.

[56] K. Reuter and M. Scheffler. Composition, structure, and stability of ruo2(110) as a function of oxygen pressure. *Phys. Rev. B*, 65:035406, 2001.

[57] N. Seriani, W. Pompe, and L. Colombi Ciacchi. Catalytic oxidation activity of pt3o4 surfaces and thin films. *J. Phys. Chem. B*, 110:14860, 2006.

[58] N. Seriani. Ab initio thermodynamics of lithium oxides: from bulk phases to nanoparticles. *Nanotechnology*, 20:445703, 2009.

[59] J.-F. Boily, S. Chatman, and K. M. Rosso. Inner-helmholtz potential development at the hematite (a-fe2o3) (001) surface. *Geochim. Cosmochim. Acta*, 75:4113, 2011.

[60] T. Lopes, L. Andrade, F. Le Formal, M. Gratzel, K. Sivula, and A. Mendes. Hematite photoelectrodes for water splitting: evaluation of the role of film thickness by impedance spectroscopy. *Phys. Chem. Chem. Phys.*, 16(31):16515, 2014.

[61] A. Gorji and N. Bowler. Static permittivity of environmentally relevant low-concentration aqueous solutions of nacl, nano3, and na2so4. *J. Chem. Phys.*, 153(1):014503, 2020.

[62] W. Wachter, W. Kunz ad R. Buchner, and H. Hefter. Is there an anionic hofmeister effect on water dynamics? dielectric spectroscopy of aqueous solutions of nabr, nai, nano 3 , naclo 4 , and nascn. *J. Phys. Chem.*, 109(1):8675, 2005.

[63] T. P. Trainor, A. M. Chaka, P. J. Eng, M. Newville, G. A. Waychunas, J. G. Catalano, , and G. E. Brown. Structure and reactivity of the hydrated hematite (0001) surface. *Surf. Sci.*, 573:204, 2004.

[64] Y. S. Hwang and J. J. Lenhart. The dependence of hematite site-occupancy standard state triple-layer model parameters on inner-layer capacitance. *J. Colloid Interface Sci.*, 319(1):206, 2008.

[65] M. Liu, J. L. Lyons, D. Yan, and M. S. Hybertsen. Semiconductor-based photoelectrochemical water splitting at the limit of very wide depletion region. *Adv. Funct. Mater.*, 26:219, 2016.

[66] K. D. Malviya, D. Klotz, H. Dotan, D. Shlenkevich, A. Tsyganok, H. Mor, and A. Rothschild. Influence of ti doping levels on the photoelectrochemical properties of thin-film hematite (alpha-fe 2o3) photoanodes. *J. Phys. Chem. C*, 121(8):4206, 2017.

[67] H. Dotan, K. Sivula, M. Grätzel, A. Rothschild, and S.C. Warren. Probing the photoelectrochemical properties of hematite (-fe2o3) electrodes using hydrogen peroxide as a hole scavenger. *Energy Environ. Sci.*, 4:958, 2011.

[68] L. Steier, I. Herraiz-Cardona, S. Gimenez, F. Fabregat-Santiago, J. Bisquert, S. D. Tilley, and M. Grätzel. Onset potential behavior in a-fe2o3 photoanodes: the influence of surface and diffusion sn doping on the surface states. *Adv. Funct. Mater.*, 24(48):7681, 2014.

[69] M. Forster, R. J. Potter, Y. Ling, Y. Yang, D. R. Klug, Y. Li Yat, and A. J. Cowan. Oxygen deficient a-fe2o3 photoelectrodes: a balance between enhanced electrical properties and trap-mediated losses. *Chem. Sci.*, 6:4009, 2015.

[70] P. S. Shinde, S. H. Choi, Y. Kim, J. Ryu, and J. S. Jang. Onset potential behavior in -fe2o3 photoanodes: the influence of surface and diffusion sn doping on the surface states. *Phys. Chem. Chem. Phys.*, 18:2495, 2016.

[71] K. Itoh and J. O. M. Bockris. Stacked thin-film photoelectrode using iron oxide. *J. Appl. Phys.*, 56:874, 1984.

[72] K. Sivula. Mott–schottky analysis of photoelectrodes: Sanity checks are needed. *ACS Energy Lett.*, 6:2549, 2021.

[73] A. Natarjan, G. Oskam, and P. C. Searson. The potential distribution at the semiconductor/solution interface. *J. Phys. Chem. B*, 102:7793, 1998.

[74] S. P. Harrington and T. M. Devine. Analysis of electrodes displaying frequency dispersion in mott-schottky tests. *J. Electrochem. Soc.*, 155:C381, 2008.

[75] C. Fabrega, D. Monllor-Satoca, S. Ampudia, A. Parra, T. Andreu, and J. R. Morante. Tuning the fermi level and the kinetics of surface states of tio2 nanorods by means of ammonia treatments. *J. Phys. Chem. C*, 117:20517, 2013.

[76] Y. Ling, G. Wang, D. A. Wheeler, J. Z. Zhang, and Y. Li. Sn-doped hematite nanostructures for photoelectrochemical water splitting. *Nano Lett.*, 11:2119, 2011.

[77] B. Klahr, S. Gimenez, F. Fabregat-Santiago, J. Bisquert, and T. W. Hamann. Photoelectrochemical and impedance spectroscopic investigation of water oxidation with "copi"-coated hematite electrodes. *J. Am. Chem. Soc.*, 134:16693, 2012.

[78] K. Ulman, M.-T. Nguyen, N. Seriani, and R. Gebauer. Passivation of surface states of -fe2o3(0001) surface by deposition of ga2o3 overlayers: A density functional theory study. *J. Chem. Phys.*, 144:094701, 2016.

[79] F. Kraushofer, Z. Jakub, M. Bichler, J. Hulva, P. Drmota, M. Weinold, M. Schmid, M. Setvin, U Diebold, P. Blaha, and G. S. Parkinson. Atomic-scale structure of the hematite -fe2o3(1102) "r-cut" surface. *J. Phys. Chem. C*, 122(3):1657, 2018.

[80] J. Yang, A. Hellman, Y. Fang, S. Gao, and M. Käll. Schottky barrier formation and band bending revealed by first-principles calculations. *Sci. Rep.*, 5:11374, 2015.

[81] N. Seriani, C. Pinilla, and Y. Crespo. Presence of gap states at cu/tio 2 anatase surfaces: Consequences for the photocatalytic activity. *J. Phys. Chem. C*, 119:6696, 2015.

[82] A. J. E. Rettie, W. D. Chemelewski, D. Emin, and C. B. Mullins. Unravelling small-polaron transport in metal oxide photoelectrodes. *J. Phys. Chem. Lett.*, 7:421, 2016.

[83] L. Giordano, G. Pacchioni, T. Bredow, and J. F. Sanz. Cu, ag, and au atoms adsorbed on tio2(1 1 0): cluster and periodic calculations. *Surf. Sci.*, 471:21, 2001.

[84] T. Bredow, E. Aprá, M. Catti, and G. Pacchioni. Cluster and periodic ab-initio calculations on k/tio2(110). *Surf. Sci.*, 418:150, 1998.

[85] T. A. Mellan, K. P. Maenetja, P. E. Ngoepe, S. M. Woodly, C. R. A. Catlow, and R. J. Grau-Crespo. Lithium and oxygen adsorption at the -mno2 (110) surface. *J. Mater. Chem. A*, 1:14879, 2013.

[86] Y. Crespo and N. Seriani. A lithium peroxide precursor on the -mno2 (100) surface. *J. Mater. Chem. A*, 2:16538, 2014.

[87] K. M. Rosso and M. Dupuis. Electron transfer in environmental systems: a frontier for theoretical chemistry. *Theor. Chem. Acc.*, 116:124, 2006.

[88] Z. Zhou, P. Huo an L. Guo, and O. V. Prezhdo. Understanding hematite doping with group iv elements: A dft+u study. *J. Phys. Chem. C*, 119:26303, 2015.

[89] P. Liao, M. C. Toroker, and E. A. Carter. Electron transport in pure and doped hematite. *Nano Lett.*, 11:1775, 2011.

[90] C. X. Kronawitter, I. Zegkinoglou, S.-H. Shen, P. Liao, I. S. Cho, O. Zandi, Y.-S. Liu, K. Lashgari, G. Westin, J.-H. Guo, F. J. Himpsel, E. A. Carter, X. L. Zheng, T. W. Hamann, B. E. Koel, S. S. Mao, and L. Vayssieres. Titanium incorporation into hematite photoelectrodes: theoretical considerations and experimental observations. *Energy Environ. Sci.*, 7:3100, 2014.

APPENDICES

Appendix A

Implementation of continuous equations

Here we show the robustness of the analysis with the continuous equations. We performed the same analysis using different dielectric constants for hematite and for the different Helmholtz parameters.

Analysis with $\epsilon = 57$ with the OH termination

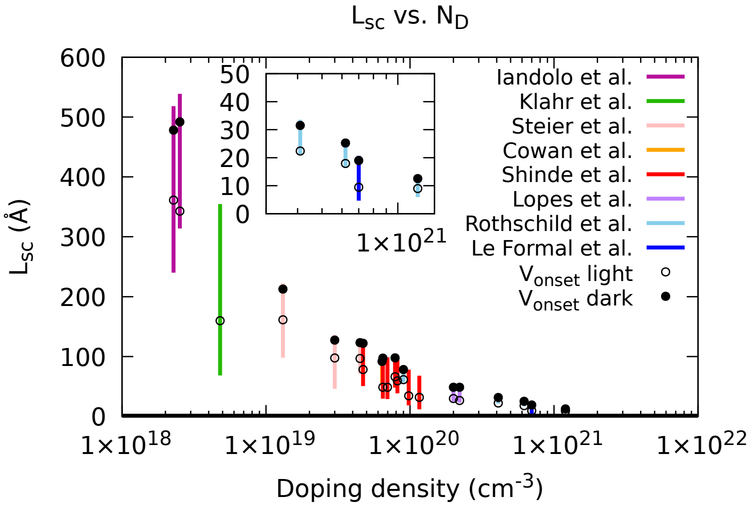

Figure A.1: Calculated drop of the space charge layer L_{sc} versus the doping density. The inset shows a zoom in on the data at high doping densities $\sim 10^{21}\text{cm}^{-3}$. The white and black dots represent the data of the onset of the OER under illuminated (1 sun) and dark conditions. Here we used $\epsilon = 80$ and together with the Helmholtz parameters extracted from the simulations of the OH termination.

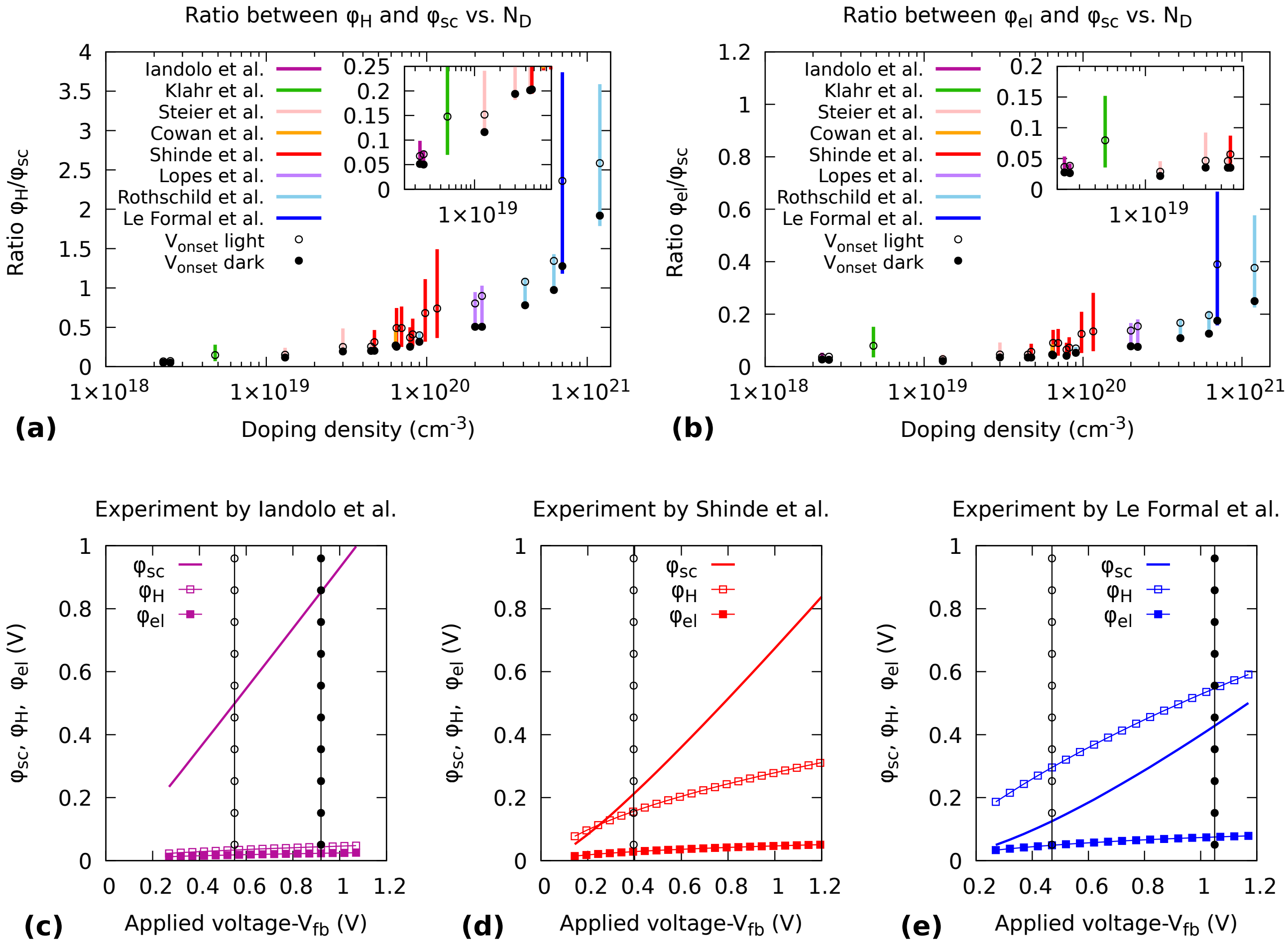

Figure A.2: Behaviour of the potential drops across the interface of hematite-OH. Figures (a) and (b) show plots of the ratios ϕ_H/ϕ_{sc} and ϕ_{el}/ϕ_{sc} versus the doping density. Figures (c), (d) and (e) show ϕ_{sc}, ϕ_H and ϕ_{el} versus the applied voltage with respect to the flatband potential for three different samples located in different regions of (a). The doping densities of the samples in these experiments were $2.28 \times 10^{18}\text{cm}^{-3}$, $1.1594 \times 10^{20}\text{cm}^{-3}$ and $7 \times 10^{20}\text{cm}^{-3}$ respectively. The vertical lines in (c), (d) and (e) represent the potential values for the onset of the oxygen evolution reaction on both dark and illuminated conditions. The zero of the applied voltage is referenced to the flat band potential V_{fb}. Voltages higher than zero mean applied voltages more positive than V_{fb}. Here, $\epsilon = 57$ has been used for bulk hematite, together with the Helmholtz parameters extracted from the simulations of the OH termination.

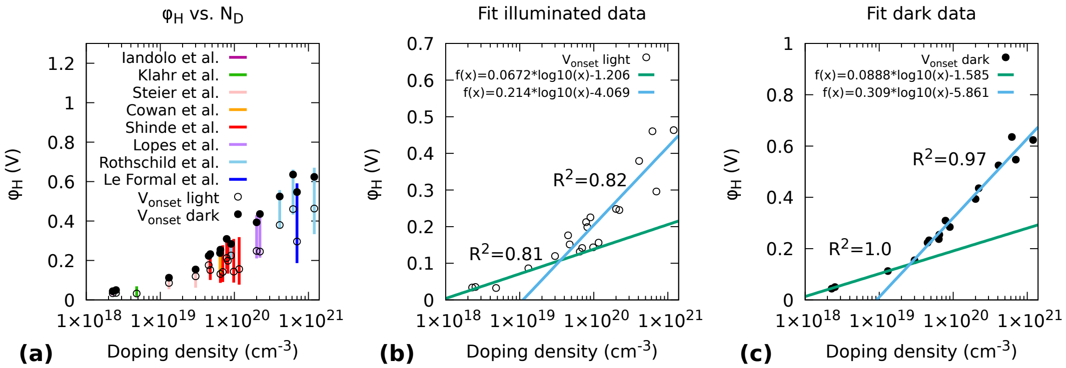

Figure A.3: Potential drop in the Helmholtz layer versus the doping density, (a). Figures (b) and (c) show linear fits performed for the data of onset potential under illuminated and dark conditions respectively. Here, $\epsilon = 57$ has been used for bulk hematite, together with the Helmholtz parameters extracted from the simulations of the OH termination.

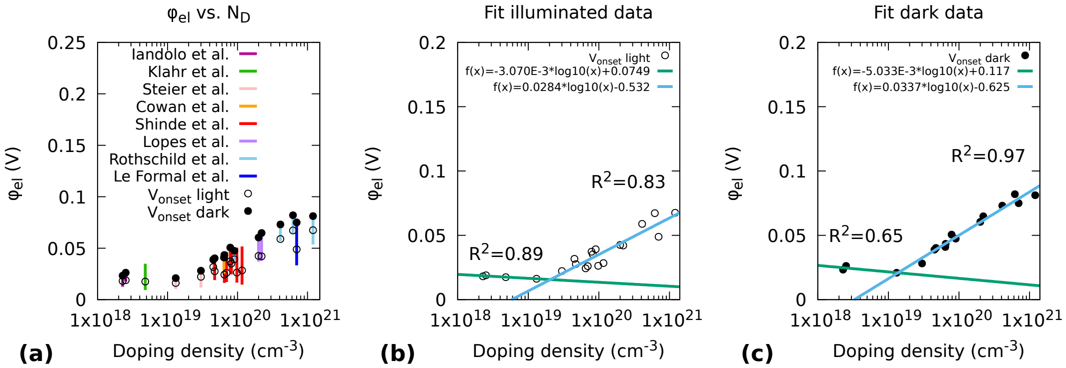

Figure A.4: Potential drop in the Gouy-Chapman layer versus the doping density, (a). Figures (b) and (c) show linear fits performed for the data of onset potential under illuminated and dark conditions respectively. Here, $\epsilon = 57$ has been used for bulk hematite, together with the Helmholtz parameters from the simulations of the OH termination.

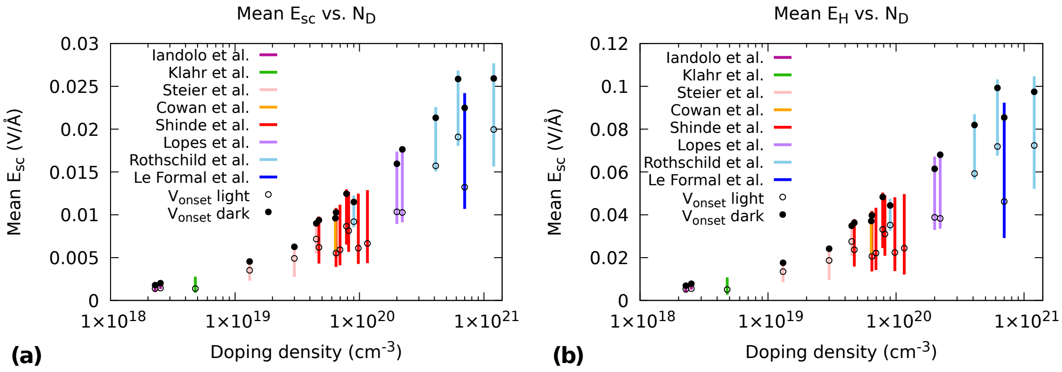

Figure A.5: Average electric field versus the doping density across the the space charge layer and the Helmholtz layer, figures (a) and (b) respectively. It can be seen that both average fields increase while increasing the doping density due to the decrease of the spatial extension of both layers. Here, $\epsilon = 57$ has been used for bulk hematite, together with the Helmholtz parameters extracted from the simulations of the OH termination.

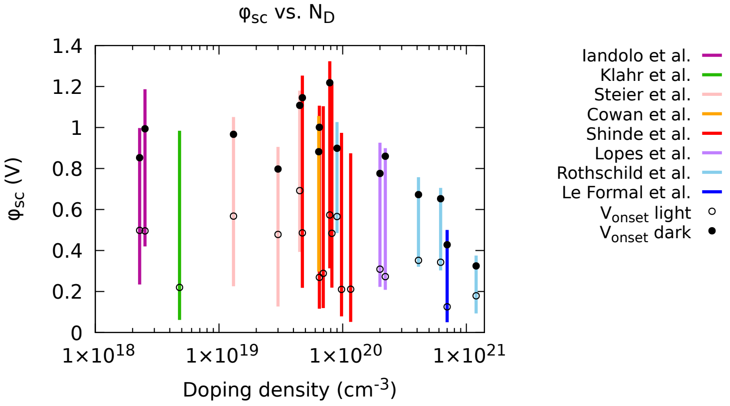

Figure A.6: Potential drop in the space charge layer versus doping density. Here, $\epsilon = 57$ has been used for bulk hematite, together with the Helmholtz parameters extracted from the simulations of the OH termination.

Analysis with $\epsilon = 80$ with the stoichiometric termination

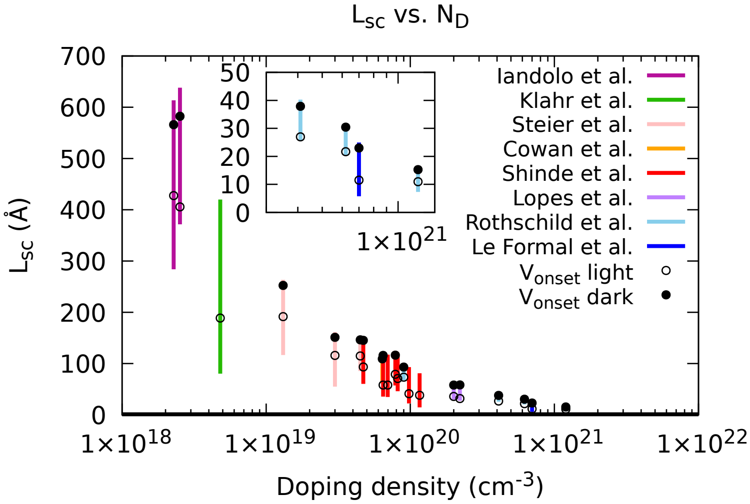

Figure A.7: Calculated drop of the space charge layer L_{sc} versus the doping density. The inset shows a zoom in on the data at high doping densities $\sim 10^{21}\text{cm}^{-3}$. The white and black dots represent the data of the onset of the OER under illuminated (1 sun) and dark conditions. Here we used $\epsilon = 80$ and the Helmholtz parameters extracted from simulations of the stoichiometric simulation.

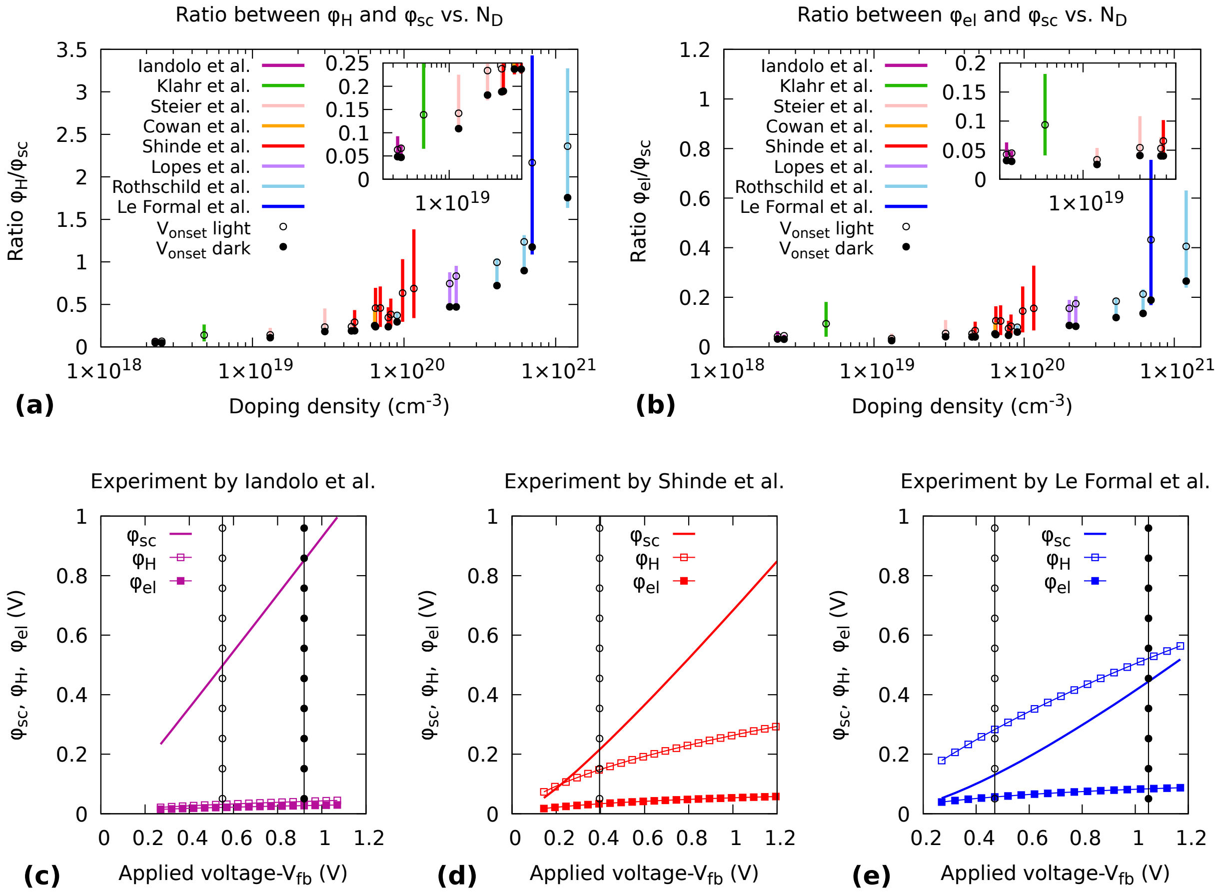

Figure A.8: Behaviour of the potential drops across the interface of hematite-NaOH. Figures (a) and (b) show plots of the ratios ϕ_H/ϕ_{sc} and ϕ_{el}/ϕ_{sc} versus the doping density. Figures (c), (d) and (e) show ϕ_{sc}, ϕ_H and ϕ_{el} versus the applied voltage with respect to the flatband potential for three different samples located in different regions of (a). The doping densities of the samples in these experiments were $2.28 \times 10^{18}\text{cm}^{-3}$, $1.1594 \times 10^{20}\text{cm}^{-3}$ and $7 \times 10^{20}\text{cm}^{-3}$ respectively. The vertical lines in (c), (d) and (e) represent the potential values for the onset of the Oxygen evolution reaction on both dark and illuminated conditions. The zero of the applied voltage is referenced to the flat band potential V_{fb}. Voltages higher than zero, mean applied voltages more positive than V_{fb}. Here, $\epsilon = 80$ has been used for bulk hematite, together with the Helmholtz parameters extracted from the simulations of the stoichiometric termination.

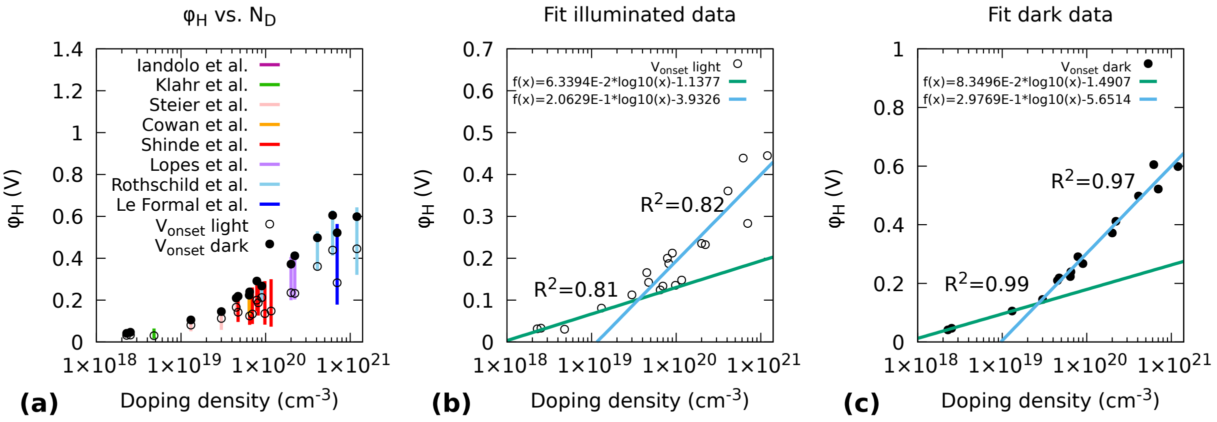

Figure A.9: Potential drop in the Helmholtz layer versus the doping density, (a). Figures (b) and (c) show linear fits performed for the data of onset potential under illuminated and dark conditions respectively. Here, $\epsilon = 80$ has been used for bulk hematite, together with the Helmholtz parameters extracted from the simulations of the stoichiometric termination.

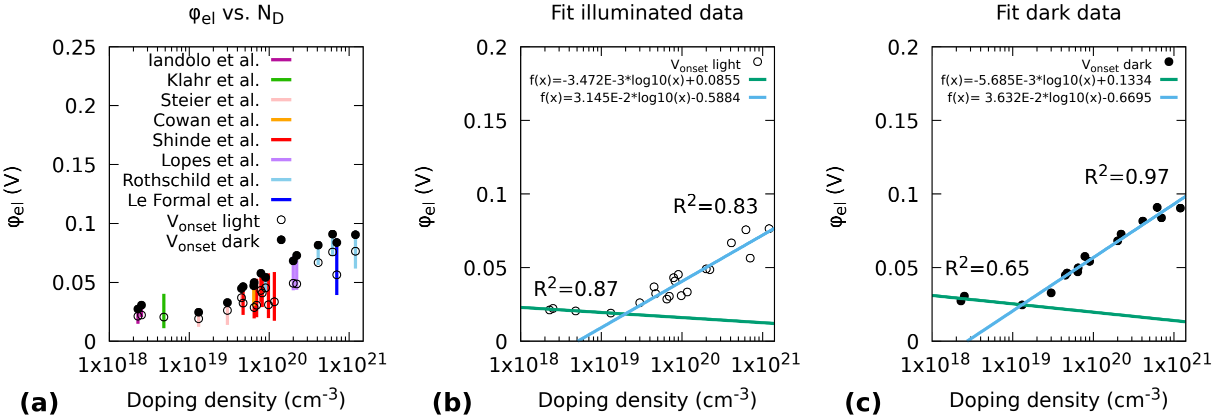

Figure A.10: Potential drop in the Gouy-Chapman layer versus the doping density, (a). Figures (b) and (c) show linear fits performed for the data of onset potential under illuminated and dark conditions respectively. Here, $\epsilon = 80$ has been used for bulk hematite, together with the Helmholtz parameters extracted from the simulations of the stoichiometric termination.

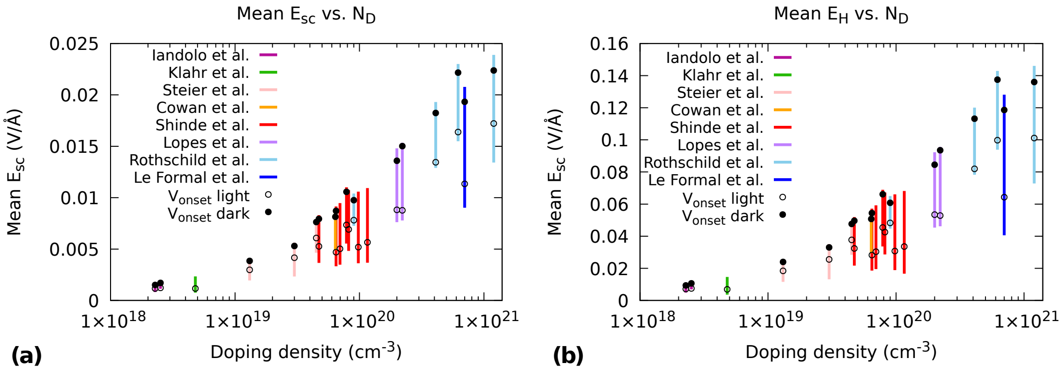

Figure A.11: Average electric field versus the doping density across the the space charge layer and the Helmholtz layer, figures (a) and (b) respectively. It can be seen that both average fields increase while increasing the doping density due to the decrease of the spatial extension of both layers. Here, $\epsilon = 80$ has been used for bulk hematite, together with the Helmholtz parameters extracted from the simulations of the stoichiometric termination.

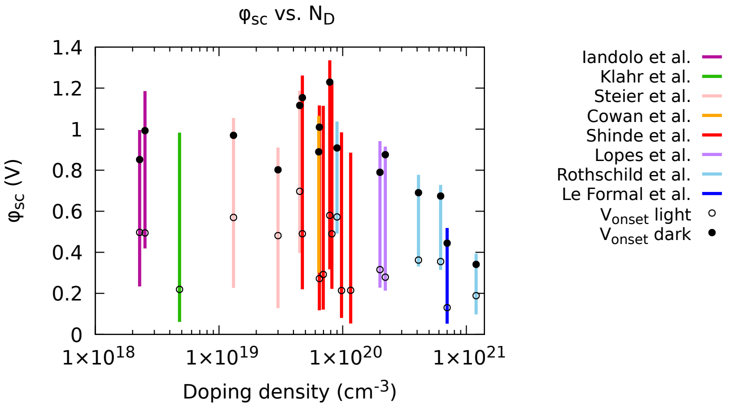

Figure A.12: Potential drop in the space charge layer versus doping density. Here, $\epsilon = 80$ has been used for bulk hematite, together with the Helmholtz parameters extracted from the simulations of the stoichiometric termination.

Appendix B

Code continuos equations

The code we used to analyze the experimental data is written in Python. The equations for the interface were solved numerically using the library scipy. This code should be compiled with versions of Python 3.

```
import numpy as np
import math
from scipy.optimize  import fsolve



#fundamental constants
e=1.60217662E-19
k=1.3806488E-23
eps0=8.8541878128E-12
T=298.15 #temperature at 25C

#Dielectric constant hematite
eps=57  #dielectric constant hematite

#Helmholtz layer parameters
```

```
eps_H=25.3
LH=4.4E-10

#parameters reported in paper
#Doping density in cm^-3
n=7E20
#range of aplied voltage (V)
vo=0.8
vf=1.7 + 0.05 ## + 0.05 is just to take into account 1.7 in the interval
#flatband potential
vfb=0.53
#Vonset potential
vonset_l=1.0  #light
vonset_d=1.58 #dark
#concentration of the solution(M)
c=1.0330
epsel=64.42

#the conversion of the parameters to SI units are performed within the
#calculations




FileName='results_LeFormal2011.dat'
f=open(FileName,'w')
f.write("# c0(M)\t  ND(cm-3) \t   L_sc(A) \t L_H(A) \t  Vapp-Vfb \t
phi_sc \t phi_H \t phi_el \t phi_el+phiH \t phi_tot\n")

#i is the voltage across the interface Vapp-Vfb
for i in np.arange(vo-vfb,vf-vfb,0.05):
```

```
     #Solving  phi_H + phi_el + phi_sc - (Vapp-Vfb)==0 numerically
     #i=(vapp-Vfb)
     #Defining function
     func = lambda x : (2*k*T/e)*np.arcsinh(math.sqrt((e*eps*abs(x)*(n*1.0E6))/
     (4*(c*6.022140857E26)*epsel*T*k))) +  ((LH*math.sqrt(2))/(eps_H*eps0))
     *math.sqrt(e*eps*eps0*(n*1.0E6*abs(x))) +abs(x)-i
     #Getting the solution
     phi_sc= fsolve(func,i)

     #Using output phi_sc as input to calculate the other quantities
     phi_el=(2*k*T/e)*np.arcsinh(math.sqrt((e*eps*abs(phi_sc)*(n*1.0E6))/
     (4*(c*6.022140857E26)*epsel*T*k)))
     phi_H = ((LH*math.sqrt(2))/(eps_H*eps0))*math.sqrt(e*eps*eps0*
     (n*1.0E6*abs(phi_sc)))
     L_G = math.sqrt((epsel*eps0*k*T)/(2*e*e*c*6.022140857E26))
     L_sc=math.sqrt((2*eps*eps0)/(e*(n*1.0E6)))*math.sqrt(abs(phi_sc)
     -(k*T/e))
     phi_total=abs(phi_sc)+phi_H+phi_el


      #-----------writing in  file
      #Lsc and LH are written in angstrom, note *1E10 in the printing
     f.write(" %.4f \t %.2E   \t %.4f \t %.4f  \t %.4f \t %.4f \t %.4f
     \t %.4f \t %.4f \t %.4f\n " %(c, n, L_sc*1.0E10, LH*1.0E10, i,
     phi_sc, phi_H, phi_el, phi_H + phi_el, phi_total ))
f.close()
```